Lehrstuhl für Hochfrequenztechnik
Technische Universität München

# Low Phase Noise SiGe Push-Push Oscillators for Millimeter Wave Frequencies

Robert Wanner

Vollständiger Abdruck der von der Fakultät für Elektrotechnik und Informationstechnik der Technischen Universität München zur Erlangung des akademischen Grades eines

*– Doktor-Ingenieurs –*

genehmigten Dissertation.

| | |
|---|---|
| Vorsitzender: | Univ.-Prof. Dr. sc. techn. (ETH) A. Herkersdorf |
| Prüfer der Dissertation: | 1. Univ.-Prof. Dr. techn. P. Russer |
| | 2. Univ.-Prof. Dr.-Ing., Dr.-Ing. habil. R. Weigel, Friedrich-Alexander-Universität Erlangen-Nürnberg |

Die Dissertation wurde am 23.11.2006 bei der Technischen Universität München eingereicht und durch die Fakultät für Elektrotechnik und Informationstechnik am 09.05.2007 angenommen.

# Zusammenfassung

In dieser Arbeit werden phasenrauscharme, monolithisch integrierte SiGe HBT Push-Push-Oszillatoren für Frequenzen im Millimeterwellenbereich untersucht. Nichtlineare Simulationsmethoden zur Signal- und Rauschanalyse von Oszillatoren und Transistoreigenschaften bei hohen Strömen und Spannungen werden diskutiert. Push-Push-Oszillatoren mit Ausgangsfrequenzen von 63 GHz bis 280 GHz wurden entworfen, und nachdem sie in einer externen Technologie realisiert wurden auch experimentell untersucht. Für die Anwendung in Kraftfahrzeug-Radar wurde ein VCO mit einer Mittenfrequenz von 78.5 GHz und einem Abstimmbereich von 6.4 % realisiert. In diesem Frequenzbereich erzielt die Schaltung eine Ausgangsleistung von 4.0 ± 0.4 dBm bei sehr niedrigem Phasenrauschen, das bei einer Ablagefrequenz von 1 MHz unter −105 dBc/Hz liegt. Ein Oszillator mit einer Ausgangsfrequenz um 278 GHz erzielte eine Ausgangsleistung von −20 dBm.

# Abstract

In this thesis low phase noise SiGe HBT monolithically integrated push-push oscillators for millimeter wave frequency generation are investigated. Nonlinear simulation methods for oscillator signal and noise analysis and device physics at high currents and high voltages are discussed. Push-push oscillators with output frequencies from 63 GHz up to 280 GHz were designed and after fabrication in an external foundry investigated experimentally. For automotive radar applications a VCO with a center frequency of 78.5 GHz and a tuning bandwidth of 6.4 % has been realized. Within this range the output power is 4.0 ± 0.4 dBm and a very low single sideband phase noise level below −105 dBc/Hz at 1 MHz offset is achieved. An oscillator with an output frequency around 278 GHz achieved an output power of −20 dBm.

# Danksagung

Diese Arbeit entstand während meiner Tätigkeit als wissenschaftlicher Assistent am Lehrstuhl für Hochfrequenztechnik der Technischen Universität München. Ich danke Herrn Professor Dr. Peter Russer, der mir die Durchführung der Untersuchungen und die Anfertigung dieser Arbeit ermöglichte. Mein Dank gilt auch Herrn Dr. Gerhard Olbrich, der mir stets mit fachlichem und praktischem Rat zur Seite stand.

Die Fertigung der integrierten Oszillatoren übernahm Infineon Technologies A. G. als Projektpartner. Ich danke für die Überlassung der Schaltungen und im Besonderen den Herren Dr. Martin Pfost, Dr. Klaus Aufinger, Dr. Herbert Knapp und Dr. Rudolf Lachner für die fachlichen Diskussionen und die Unterstützung und Geduld bei der Erstellung der Schaltungslayouts.

Ich danke Herrn Dr. Werner Anzill für die hilfreiche Erläuterung seiner Methode zur Berechnung des Phasenrauschens. Herr Professor Dr. Steve Maas unterstützte mich durch wertvolle Diskussionen bezüglich der Harmonic Balance Methode.

Für das sehr freundschaftliches Arbeitsklima und die Hilfsbereitschaft danke ich allen Kolleginnen und Kollegen am Lehrstuhl. Besonderen Dank schulde ich meinem Freund und Kollegen Michael Zedler, der diese Arbeit Korrektur las und mir fachlich, sowie darüber hinaus eine große Hilfe war. Zudem danke ich Tobias Hermann für die Unterstützung bei praktischen Arbeiten und der Messtechnik und Stephan Braun für die allseitige Diskussionsbereitschaft.

Nicht vergessen möchte ich schließlich meine Frau, die mich abseits der fachlichen Themen emotional unterstützt hat.

Vergelt's Gott.

Contact: wanner@mytum.de

# Contents

# Chapter 1

# Introduction

## 1.1 Millimeter Wave Oscillators

In future millimeter-wave[1] and submillimeter-wave applications as high-resolution radars, biological and chemical sensors and wide bandwidth communication systems the key components are compact, reliable low noise sources [1]. Monolithic microwave integrated circuits (MMIC) can obtain the required performance for most of these systems combined with small sizes, low weight and high reliability. Traditionally at these frequencies microwave tubes and microwave diodes have been used. However, nowadays the advances in transistor technologies allow realizing transistor based millimeter wave oscillators. While at first mainly III/V semiconductor transistors have reached the millimeter wave frequency range, the latest developments in SiGe heterojunction bipolar transistors (HBTs) [2–5] allow the SiGe technology to compete now with III/V based technologies at these frequencies. Tube and diode based oscillators have been pushed back to high power applications and to extremely high frequencies.

The low noise level at low frequencies (LF) and the resulting low oscillator phase noise are areas in which SiGe HBTs generally outperform III/V HBTs or high electron mobility transistors (HEMTs) [6]. The significant lower costs of SiGe chip area can reduce the prices of millimeter-wave systems and thus it has the potential to open mass markets for consumer systems at millimeter-wave frequencies.

The integration of complete oscillator circuits on a chip reduces costs in mass production and enables to integrate other functionalities on the same chip. This way

[1] Millimeter-wave denotes the frequency range, where the free space wavelength is between 1 mm and 10 mm, i. e. from 30 GHz to 300 GHz

expensive interconnects are avoided, the reliability is increased and the total system size shrinks. The realization of complete systems on chip (SoC) for millimeter applications is therefore advantageous.

Integrated realizations, however, require more than discrete assemblies a precise circuit modeling, since a tuning of the dimensions of circuit elements after production is very limited. Due to the nonlinear behavior of oscillator circuits, a nonlinear circuit simulation is indispensable. In section 2.1 therefore simulation methods for determining the oscillators steady state are considered.

Besides the deterministic characteristics as output frequency and output power in oscillator circuits, the stochastic parameters are of interest. The oscillator phase noise e. g. is one of the key requirements in high-resolution radar systems. Therefore, in the design of oscillators not only the deterministic quantities, but also the noise behavior needs to be considered. Hence, in section 2.2 methods for the analysis of oscillator phase noise are investigated.

## 1.2 State of the Art of Integrated Millimeter Wave Oscillators

In the last decade several MMICs for signal generation at millimeter wave frequencies have been realized. Many of these oscillators are produced in III/V semiconductor based technologies, but recent years have proven that advanced Si based devices are capable of producing signals in the millimeter wave frequency range.

Figure 1.1 shows the state-of-the-art output power and measured single side band phase noise level of integrated oscillators for signals from 40 GHz to 100 GHz. The circuits [14, 19, 25–29] are push-push oscillators and [7–13, 15–18, 20–24] are fundamental frequency oscillators. In the designs of [7, 13, 16, 18, 20–22, 24] output buffers are used. The oscillator in [14] is hybrid integrated, while all other circuits are MMICs.

It can be seen that the lowest phase noise levels are obtained by using HBTs. The use of the push-push oscillator topology and investigations on the noise behavior have allowed to achieve superior phase noise levels with the oscillators realized in this work [25–30].

At frequencies above 100 GHz the number of published MMIC oscillators is limited. To the authors knowledge the comparison in Figure 1.2 of output power and

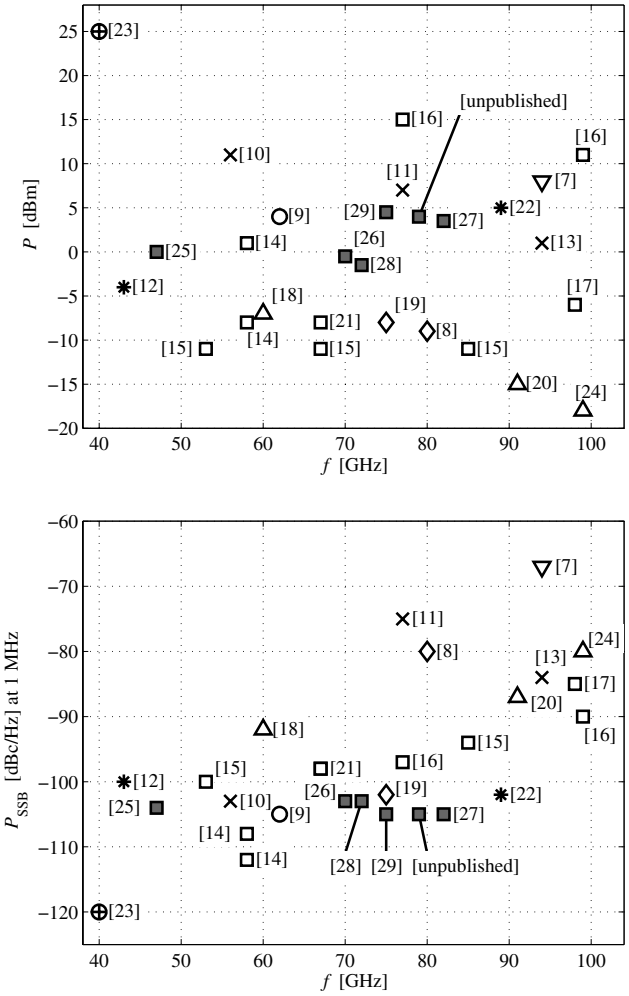


Figure 1.1: State-of-the-art output power $P$ and single side band phase noise level $P_{\mathrm{SSB}}$ at 1 MHz offset frequency for integrated transistor based oscillators in the frequency range from 40 GHz to 100 GHz (◇ GaAs HBT, ✱ InP HBT, × GaAs HEMT, ▽ GaAs HFET, △ CMOS, ⊕ GaN HEMT, □ SiGe HBT and ■ SiGe HBT that are presented in this work).

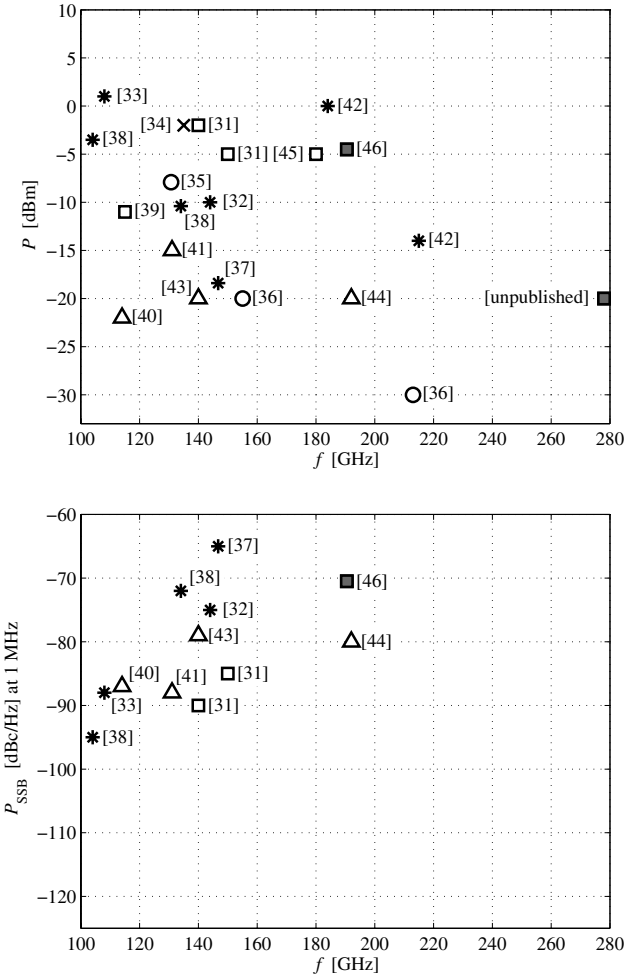


Figure 1.2: State-of-the-art output power $P$ and single side band phase noise level $P_{SSB}$ at 1 MHz offset frequency for integrated transistor based oscillators above 100 GHz (✱ InP HBT, × GaAs HEMT, ○ InP HEMT, △ CMOS, □ SiGe HBT and ■ SiGe HBT that are presented in this work).

measured single side band phase noise levels of transistor based oscillators for these frequencies is complete. The circuits in [31–34, 40–42, 44–46] are push-push oscillators and the circuits in [35–39, 43] are fundamental frequency oscillators. In [34–36, 39, 42, 45] and for the unpublished oscillator of this work (see section 5.2.2) no reliable phase noise measurement data are given. For oscillators where the phase noise is measured at another offset frequency (e. g. at 10 MHz) the measured data is scaled by 20 dB per decade to allow a comparison in the Figure.

The oscillator in [46] that has been developed within this work has been the first HBT based oscillator giving an output frequency above 150 GHz. The output power of the 190 GHz signal is with −4.5 dBm in the same range as previously published oscillators operating below 150 GHz. In addition, the measured phase noise level coincides with the performance of previously published oscillator data operating at lower frequencies.

To the authors knowledge the InP D-HBT based push-push oscillator described in [42] shows with 215 GHz the highest output frequency of any transistor based and of any MMIC oscillator published up to now. With the unpublished oscillator at 278 GHz that also originates from this work, the first transistor based oscillator with an output frequency beyond 215 GHz has been realized.

For the generation of higher frequencies diodes and microwave tubes are used. In [47] Eisele et al show InP Gunn diode based oscillators, operating in a second harmonic mode that give an output power of −1.5 dBm at 333 GHz. In [48] GaAs TUNNETT diodes oscillating at frequencies up to 655 GHz in fundamental mode and giving an output power of −61 dBm are reported. The main drawbacks of these diode based signal generators compared to MMIC transistor based solutions are, however, the low tunability of the output frequency and the expensive mounting techniques required for the connection to waveguide resonators. When high output high powers are required tubes are used. Usually they cannot compete in size, weight and costs with solid-state circuits.

## 1.3 Contents of this work

In this work monolithic integrated SiGe push-push oscillators for automotive radar applications in the frequency range around 77 GHz and for signal generation at much higher frequencies, i. e. at 190 GHz and 278 GHz, are presented. In the design of the oscillators, the main attention is paid on a low phase noise level of the output

signals. By using SiGe HBT technology in combination with the push-push oscillator principle, low phase noise levels are achieved.

In chapter 2 methods for calculating the oscillators steady state signals and its noise behavior are investigated. Focus is put on the oscillator phase noise at harmonic frequencies since in a push-push oscillator the second harmonic signal content is coupled to the output. The conversion matrix approach by Anzill [49, 50] for the analysis of oscillator phase noise in frequency domain by perturbation method is therefore generalized for arbitrary harmonics.

Chapter 3 describes the push-push oscillator principle, gives an expression to estimate the gain in phase noise that is achieved by push-push oscillators compared to fundamental frequency oscillators and gives a procedure for the design of such oscillators.

The succeeding chapter outlines the boundary conditions in the circuit design within this work. The fabrication technology and the active and passive components that can be realized with this process and that are used for the oscillator design are described. For achieving high amplitude swings possible driving conditions for the SiGe HBTs are analyzed with respect to the device physics at high currents and high voltages. Passive circuit elements as spiral inductors and transmission lines are considered by means of full-wave analysis. In chapter 5 finally the design and the experimental results are exemplarily presented for some of the realized circuits.

# Chapter 2

# Oscillator Signal Analysis

The signal analysis of an oscillator is generally divided into two parts: The calculation of the limit cycle for the unperturbed oscillator and based on that, the determination of the noise properties of the perturbed oscillator. From these two steps follows the structure of this chapter: First methods for the determination of the steady state are investigated. Thereafter different methods for the oscillator noise analysis are considered, while the focus is put on the conversion analysis approach in frequency domain.

## 2.1 Determination of the steady state

### 2.1.1 Linear Analysis of Oscillators

In an electronic oscillator a DC input power is transformed to a periodic output signal with a specific fundamental frequency and a constant amplitude. This basic behavior cannot be realized or modeled by linear circuit models [51]. The linear consideration, however, allows to analyze the stability of a circuit and thus to prove the condition for the startup of an oscillation.

A linear system is stable when the transfer function of the form

$$H(s) = \frac{\prod_m (s + z_m)}{\prod_n (s + p_n)} \tag{2.1}$$

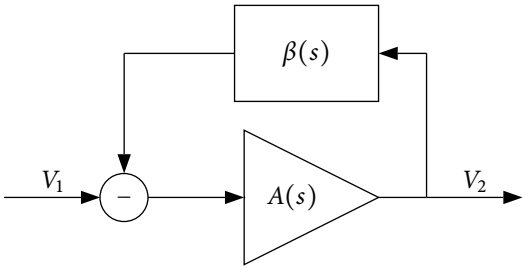


Figure 2.1: Feedback oscillator model

has no poles in the right half of the complex frequency plane $s$. When poles with positive real parts exist, the response to a small transient excitation is an exponentially growing signal. The linear circuit theory cannot predict the amplitude growth of this signal, as it is limited by nonlinear effects. For an oscillation with a constant amplitude a pole on the complex frequency axis $\Re\{s\} = 0$ is required. This, however, cannot be realized exactly in a linear system due to uncertainties in device dimensions [51].

For the linear analysis of an oscillator circuit two methods are commonly used: The positive feedback model and the negative resistance model. Figure 2.1 shows the feedback oscillator model consisting of an amplifier with the transfer function $A(s)$ and a feedback path with the transfer function $\beta(s)$. The combination of the two elements results in the transfer function

$$H(s) = \frac{V_2(s)}{V_1(s)} = \frac{A(s)}{1 + A(s)\beta(s)}. \tag{2.2}$$

A steady state oscillation can occur when for technical frequencies $s = \mathrm{j}\omega$ the open loop gain $A(\mathrm{j}\omega)\beta(\mathrm{j}\omega) = -1$. In this case the transfer function $H(s)$ of the feedback oscillator shows poles on the imaginary axis. This requirement for steady state oscillation is known as the Barkhausen criterion.

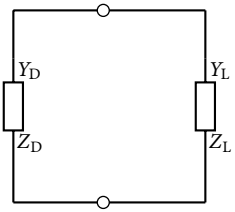


Figure 2.2: Negative impedance oscillator model

For the startup of an oscillation from the noise inherent in any circuit, the NYQUIST stability criterion is to be considered [52]: The number of right-hand plane poles of a system is equal to the number of the right-hand plane poles of $A(s)\beta(s)$ plus the number of the clockwise encirclements of the point $s = -1$ by $A(\mathrm{j}\omega)\beta(\mathrm{j}\omega)$. Counterclockwise encirclements are to be subtracted from the clockwise encirclements. When $A(s)\beta(s)$ has no right half plane poles, the number of clockwise encirclements of $s = -1$ directly determines the stability of the feedback system.

The second model, the negative resistance model, has been shown already in 1917 by Vallauri [53]. This method is equivalent to the positive feedback model from a network theoretical point of view [51]. For this model we consider the circuit in Figure 2.2. $Z_D(s)$ and $Z_L(s)$ represent the impedance of the active device and the impedance of the load circuit, respectively. $Y_D(s)$ and $Y_L(s)$ are the corresponding admittances. In the case of series resonance a steady state oscillation at the frequency $s_0$ can be achieved when

$$Z_D(s_0) + Z_L(s_0) = 0 \tag{2.3}$$

is fulfilled for its real an its imaginary parts. For parallel resonance the admittances are to be considered and the corresponding condition for a steady state oscillation is given by

$$Y_D(s_0) + Y_L(s_0) = 0. \tag{2.4}$$

For the startup of an oscillation the poles of the circuit in Figure 2.2 need to be investigated in. This can be achieved either determining the poles of the equation

$Z_D(s) + Z_L(s) = 0$ directly or by using the NYQUIST stability criterion. For the latter the transfer function $T_Z(s) = Z_D(s)/Z_L(s)$ needs to be considered [52] with respect to its right hand side poles and the encirclements of the point $s = -1$ for $s = j\omega$ as described above. For the ease of simplicity the circuit is separated in a way so that poles in the transfer function are omitted. When admittances are considered the transfer function is given by $T_Y(s) = Y_L(s)/Y_D(s)$, which is equal to $T_Z(s)$.

In most of the technical relevant cases, i. e. high $Q$-resonator oscillators, the following assumptions are met: The frequency dependency of the load circuitry can be neglected. Furthermore, the transfer function does not show right hand side poles and encircles the point $s = -1$ only once for $s = j\omega$. When these conditions are fulfilled, the NYQUIST criterion can be proven by the analysis of the crossing point of the transfer function and the real axis. An oscillation can rise from the noise, when this crossing point is located at $s < -1$ and the direction of the curve at the intersection is in clockwise direction. For impedances this can be formulated by

$$\Re\{Z_D(s_0) + Z_L(s_0)\} < 0 \quad \text{and} \quad \Im\{Z_D(s_0) + Z_L(s_0)\} = 0 \tag{2.5}$$

$$\text{and} \quad \frac{\partial \Im\{Z_D(s_0)\}}{\partial \omega} > 0. \tag{2.6}$$

When admittances are considered, these conditions are given by

$$-\Re\{Y_L(s_0)\} < \Re\{Y_D(s_0)\} < 0 \quad \text{and} \quad \Im\{Y_D(s_0) + Y_L(s_0)\} = 0 \tag{2.7}$$

$$\text{and} \quad \frac{\partial \Im\{Y_D(s_0)\}}{\partial \omega} < 0. \tag{2.8}$$

This dependency has been formulated already by Kurokawa in 1969 within the derivation of the onset of an oscillation by an nonlinear network analysis [54]. The conditions in (2.5) are often found in literature as general conditions required for the startup of an oscillation, while (2.6) is most times omitted. This simplification is justified for most technical oscillators, as the phase of impedances usually grow with frequency. For a correct analysis of the oscillation conditions, however, the complete set of equations and the conditions above must be considered.

The negative impedance model is originated by works on oscillators that use two terminal devices as e. g. diodes as active elements, to obtain the negative resistance. In the case of three terminal devices, as e. g. transistors, the device is usually embedded into a passive network and the impedance at the output terminal is considered.

A more elegant linear method to consider an oscillatory circuit is the straightforward linear network analysis. In the small signal case the system of network equations

$$\mathbf{M}(s)\mathbf{x} = \mathbf{0} \tag{2.9}$$

in the frequency domain with the oscillation frequency $\omega$ as parameter is set up. The matrix $\mathbf{M}$ denotes the matrix describing the linear circuit and the vector $\mathbf{x}$ denotes the state variables. This homogeneous system of linear equations is the network theoretical formulation of the oscillation condition. It is equivalent to the other two criteria described above [51]. The positive feedback method and the negative impedance method, however, give the circuit designer a better understanding of the circuit properties, especially, when it comes to the startup conditions for an oscillation.

### 2.1.2 Nonlinear Analysis of Oscillators

The linear circuit analysis is an approximation of the nonlinear behavior at a specific operating point for small signals. With increasing signal amplitudes nonlinearities must be considered for a rigorous circuit analysis. While for a small signal amplifier in general a linear analysis is appropriate, it gives only a rough approximation for e. g. a power amplifier or an oscillator. In the linear analysis only one frequency is considered, while the generation of harmonics and the mixing between frequencies are neglected.

In an oscillator circuit, the nonlinearities cause the amplitude saturation that determines the steady state amplitude of the oscillating signal and its harmonic content. Therefore, in a linear analysis the output power of an oscillator cannot be calculated.

The nonlinear behavior of oscillators has been studied already in 1934 by van der Pol [55] by means of nonlinear differential equations. The so-called van der Pol oscillator consists of a resistive nonlinearity that is modeled by a cubic function. By solving the differential equations, van der Pol is able to determine the signal power of the oscillator.

Numerical methods for solving the nonlinear network equations for arbitrary circuits have been established in recent decades. The state of the art are time domain [56,57], frequency domain [58] and combined frequency-time domain [59–62] methods, which are implemented in most commercial simulators.

For oscillators to be designed for low phase noise, straightforward transient time domain methods are in general not suitable. The high resonator $Q$ implies very long turn-on transients and thus a large number of time steps needs to be analyzed [59, 60]. Additionally distributed circuit elements are generally described in frequency domain by **Y**- or **S**-parameters that cannot directly be transformed into the time domain [63].

Thus, for the analysis of oscillators the most appropriate methods are frequency domain and combined frequency-time domain methods. These methods can be summarized by the term *harmonic balance methods* and methods derived hereof.

In harmonic balance the solution is represented by a linear combination of sinusoids. Thus, it is a frequency domain method. The nonlinear equations, however, are mostly solved in the time domain and Fourier transformed into the frequency domain, but can also be solved directly in the frequency domain [64]. This, however, is not a fundamental property of the algorithm [61]. The characteristic property of the method is that the currents of the linear and nonlinear subcircuits are equal (balanced) at all ports.

For the circuit analysis by harmonic balance the circuit is usually separated in a linear and a nonlinear subcircuit as shown in Figure 2.3. The linear part is then solved in the frequency domain, while the nonlinear part is analyzed in the time domain. The solution is found when the currents of the two subcircuits balance out, or in other words, they fulfill Kirchhoff's current law.

The separation into subcircuits is not compulsory. The circuit partitioning is mainly advantageous when the linear subcircuit is much larger than the nonlinear subcircuit [61].

In harmonic balance the port variables are described by the state vector

$$\mathbf{X} = \begin{bmatrix} \mathbf{X}_1 \\ \vdots \\ \mathbf{X}_N \end{bmatrix} \tag{2.10}$$

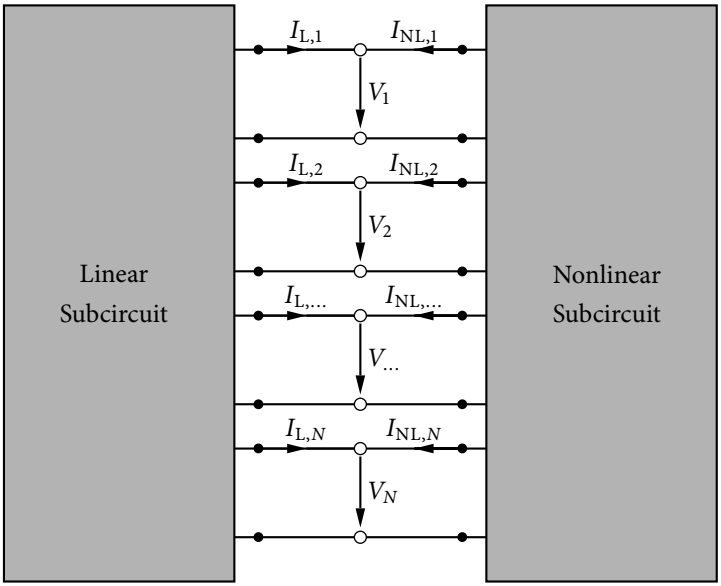


Figure 2.3: Linear and nonlinear subcircuits for harmonic balance analysis

containing $N$ subvectors $\mathbf{X}_n$ that represent the state variables at each of port. For node oriented harmonic balance methods the state variables are the currents and the voltages at the common nodes, whereas for port oriented harmonic balance methods normalized powers are considered [63]. In this work, focus is put to node oriented harmonic balance methods.

Each state variable $\mathbf{X}_n$ represents the Fourier coefficients of the time domain voltage or current at node $n$ that is assumed to be periodic. The coefficients are assorted in the subvector

$$\mathbf{X}_n = \begin{bmatrix} X_{n,-K} \\ \vdots \\ X_{n,+K} \end{bmatrix}. \tag{2.11}$$

In this thesis the harmonic balance formulation with positive and negative frequencies is used. By using a notation with only positive frequencies, the computational effort for solving the system of equations could be reduced [61, 63]. The considered frequency range is limited to $K$ harmonics resulting in a dimension of $N(2K+1)$ for the state vector $\mathbf{X}$. The Fourier coefficients for the negative frequency components in the state vectors are the complex conjugates of the positive frequency components

$$X_{n,-k} = X^*_{n,+k}. \tag{2.12}$$

Hence, the number of unknowns in the state vector is reduced to $NK$. In node oriented harmonic balance the function $\mathbf{F}(\mathbf{V}, \omega)$ that describes the circuit relates the voltage stage vector to the current stage vector as

$$\mathbf{F}(\mathbf{V}, \omega) = \mathbf{I}. \tag{2.13}$$

The steady state solution denoted by $\mathbf{V^0}$ is found when for a given set of port voltages Kirchhoff's current law for the currents into the linear and into the nonlinear subnetwork is fulfilled

$$\mathbf{F}(\mathbf{V^0}, \omega) \equiv \mathbf{0}. \tag{2.14}$$

The function $\mathbf{F}(\mathbf{V}, \omega)$ is called the cost function or the error function and is to be minimized when the problem is solved. (2.14) shows an infinite number of possible solutions due to the unassigned phase of a free running oscillator. Therefore, the phase of the first harmonic at one node is usually set to zero (see e. g. [49, 50]).

**The Linear Subcircuit**

The linear subcircuit is described by the linear system of equations as

$$\mathbf{I}_\mathrm{L} = \mathbf{Y}\mathbf{V} \tag{2.15}$$

were $\mathbf{I}_{\mathrm{L}}$ and $\mathbf{V}$ are state vectors for current and voltage, respectively, in the form defined in (2.10). The admittance matrix $\mathbf{Y}$ is given by harmonic Y-parameters. It has the dimension $N(2K+1)$ and consists of $N \times N$ submatrices $\mathbf{Y}_{m,n}$ with the dimension $2K+1$

$$\mathbf{Y}_{m,n} = \mathrm{diag}[\,Y_{m,n}(k\omega)\,] \quad \text{for} \quad k = -K, \ldots, K. \tag{2.16}$$

These submatrices are diagonal matrices describing the Y-parameters at the harmonics of the fundamental frequency $\omega$.

**The Nonlinear Subcircuit**

The most common nonlinear elements in RF circuits are nonlinear capacitors, resistors and controlled sources. The nonlinear elements are assumed to be all voltage controlled. This is not a limitation as current controlled nonlinearities can be transformed to voltage controlled elements [63]. For determining the nonlinear current vector $\mathbf{I}_{\mathrm{NL}}$ in (2.14) first the excitation voltage vectors for each port $\mathbf{V}_{\mathrm{n}}$ are inverse Fourier transformed into the time-domain

$$\mathbf{V}_n \bullet\!\!-\!\!\circ\, v_n(t). \tag{2.17}$$

The current into a nonlinear conductance or a controlled current source is given by

$$i_{\mathrm{G,n}}(t) = f_{\mathrm{G,n}}(v_1(t), v_2(t), \ldots, v_N(t)) \tag{2.18}$$

as a function of all port voltages $v_m$ in the time domain. By the Fourier transform $i_{\mathrm{G,n}}(t) \circ\!\!-\!\!\bullet\, \mathbf{I}_{\mathrm{G,n}}$ the current vector in the frequency domain at port $n$ is determined. The current vectors for all nodes are written in the form as (2.10) by

$$\mathbf{I}_G = \begin{bmatrix} \mathbf{I}_{G,1} \\ \vdots \\ \mathbf{I}_{G,N} \end{bmatrix}. \tag{2.19}$$

In a nonlinear capacitor the charge is considered in the time domain a function of the port voltages. It is given by

$$q_n(t) = f(v_1(t), v_2(t), \ldots, v_N(t)). \tag{2.20}$$

The Fourier transform of the charge waveform $q_n(t)$ results in the frequency domain charge vector $\mathbf{Q}_n$. The charge vectors of all ports are summarized in the charge vector $\mathbf{Q}$.

The displacement current through a nonlinear capacitor is defined as the time derivative of the charge

$$i_{\mathrm{c,n}}(t) = \frac{d}{dt} q_n(t), \tag{2.21}$$

which complies in the frequency domain with a multiplication by $\mathrm{j}\,k\omega$

$$\frac{d}{dt} q_n(t) \circ\!\!-\!\!\bullet\, \mathrm{j}\,k\omega Q_{n,k}. \tag{2.22}$$

For this multiplication in the frequency domain the diagonal matrix

$$\mathbf{\Omega} = \mathrm{diag}[\mathbf{\Omega}_1, \mathbf{\Omega}_2 \ldots \mathbf{\Omega}_N] \tag{2.23}$$

consisting of the diagonal submatrices with the harmonic frequency contributions for each port $n$

$$\mathbf{\Omega}_n = \mathrm{diag}[-K, \ldots, K] \tag{2.24}$$

is introduced. Thus, the state vector for the current can be written in the frequency domain by

$$\mathbf{I}_c = \mathrm{j}\,\omega\mathbf{\Omega}\mathbf{Q}. \tag{2.25}$$

The total current into the nonlinear subcircuit is the sum of the current into the nonlinear conductances and into the nonlinear capacitances

$$\mathbf{F}_{\mathrm{NL}}(\mathbf{V}) = \mathbf{I}_{\mathrm{NL}} = \mathbf{I}_{\mathrm{G}} + \mathrm{j}\,\omega\mathbf{\Omega}\mathbf{Q}. \tag{2.26}$$

**Numerical Algorithm for Harmonic Balance**

With (2.15) and (2.26) Kirchhoff's current law in (2.14) can be rewritten as

$$\mathbf{F}(\mathbf{V}) = \mathbf{Y}\mathbf{V} + \mathbf{I}_{\mathrm{G}} + \mathrm{j}\,\omega\mathbf{\Omega}\mathbf{Q} \equiv \mathbf{0}. \tag{2.27}$$

In most circuits the solution of this equation can be found only numerically due to its high complexity. The most common algorithm for solving (2.27) is Newton's method or modifications of this method [61, 63]. For this purpose the nonlinear function $\mathbf{F}(\mathbf{V})$ is linearized at one set of trial voltages $\mathbf{V}_0$ as

$$\mathbf{F}(\mathbf{V}_0+\delta\mathbf{V}) \approx \mathbf{F}(\mathbf{V}_0) + \mathbf{J}_{\mathrm{F}}(\mathbf{V}_0)\delta\mathbf{V} \tag{2.28}$$

with

$$\mathbf{J}_{\mathrm{F}}(\mathbf{V}_0) = \left.\frac{\partial\mathbf{F}(\mathbf{V})}{\partial\mathbf{V}}\right|_{\mathbf{V}=\mathbf{V}_0}. \tag{2.29}$$

The matrix $\mathbf{J}_{\mathrm{F}}(\mathbf{V}_0)$ is known as the Jacobian matrix. From

$$\mathbf{F}(\mathbf{V}_0) - \left.\frac{\partial\mathbf{F}(\mathbf{V})}{\partial\mathbf{V}}\right|_{\mathbf{V}_0} \Delta\mathbf{V} \equiv \mathbf{0} \tag{2.30}$$

the estimate voltage correction vector $\Delta\mathbf{V}$ can be calculated. Starting from an arbitrary set of trial voltages the steady state is calculated iteratively. The elements of the Jacobian are given by

$$\mathbf{J}_{\mathrm{F}}(\mathbf{V}_0)[i,j] = \left.\frac{\partial F_i(\mathbf{V})}{\partial V_j}\right|_{\mathbf{V}=\mathbf{V}_0}. \tag{2.31}$$

For calculating the Jacobian matrix we recall (2.27) and derive each addend with respect to the components of $\mathbf{V}$ as

$$\mathbf{J}_{\mathrm{F}} = \mathbf{Y} + \frac{\partial \mathbf{I}_{\mathrm{G}}}{\partial \mathbf{V}} + \mathrm{j}\,\omega\mathbf{\Omega}\frac{\partial \mathbf{Q}}{\partial \mathbf{V}}. \tag{2.32}$$

The linear subcircuit contributes with the matrix $\mathbf{Y}$ directly to the Jacobian matrix whereas the nonlinear subcircuit needs to be investigated in the time domain and then Fourier transformed into the frequency domain [63]. The frequency domain current coefficients at node $n$ are determined by the Fourier transform

$$I_{n,k} = \frac{1}{T}\int_0^T i_n(t)\mathrm{e}^{-\mathrm{j}\,k\omega_0 t}\mathrm{d}t \tag{2.33}$$

from the time domain waveform. Its derivatives with respect to the voltage $V_{m,l}$ at node $m$ at the frequency $l\omega_0$ are

$$\frac{\partial I_{n,k}}{\partial V_{m,l}} = \frac{1}{T}\int_0^T \frac{\partial i_n}{\partial v_m}\frac{\partial v_m}{\partial V_{m,l}}\mathrm{e}^{-\mathrm{j}\,k\omega_0 t}\mathrm{d}t. \tag{2.34}$$

With the inverse Fourier transform of the voltage $\mathbf{V}_{\mathrm{m}}$ at port $m$

$$v_m(t) = \sum_{l=-K}^{K} V_{m,l}\mathrm{e}^{\mathrm{j}\,l\omega_0 t} \tag{2.35}$$

we determine the derivative

$$\frac{\partial v_m}{\partial V_{m,l}} = \mathrm{e}^{\mathrm{j}\, l \omega_0 t} \tag{2.36}$$

and obtain from (2.34) the derivative of the coefficient for the $k$th harmonic of the current into port $n$ by the coefficient for the $l$th harmonic of the voltage at port $m$

$$\frac{\partial I_{n,k}}{\partial V_{m,l}} = \frac{1}{T} \int_0^T \frac{\partial i_n}{\partial v_m} \mathrm{e}^{-\mathrm{j}\,(k-l)\omega_0 t} \mathrm{d}t. \tag{2.37}$$

For nonlinear capacitors the derivative of the charge with respect to voltage is determined by

$$\frac{\partial Q_{n,k}}{\partial V_{m,l}} = \frac{1}{T} \int_0^T \frac{\partial q_n}{\partial v_m} \mathrm{e}^{-\mathrm{j}\,(k-l)\omega_0 t} \mathrm{d}t. \tag{2.38}$$

The Jacobian matrix is composed of $N \times N$ submatrices. Each submatrix has the dimension $2K+1$ and represents a harmonic matrix for one node. The diagonal elements of these submatrices give the admittance values for all considered harmonics, while the off-diagonal elements describe harmonic mixing transadmittances.

For the analysis of a circuit by harmonic balance the Jacobian matrix needs to be recalculated for each iteration step. By using (2.30) the estimate voltage correction vector $\Delta\mathbf{V}$ is determined. The solution is found, when the error $\mathbf{F}(\mathbf{V})$ vanishes.

### 2.1.3 Example: Jacobian Matrix of the Van der Pol Oscillator

In the following we determine the Jacobian matrix for the steady state solution of the van der Pol oscillator in Figure 2.4. The phase noise of this oscillator will be analyzed in an example in the the phase noise chapter (2.2.3).

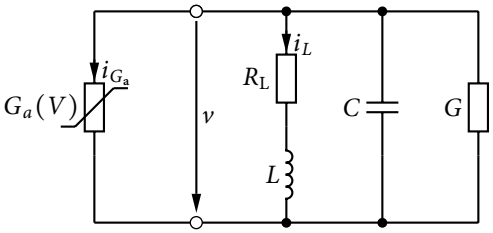


Figure 2.4: Van der Pol oscillator

A van der Pol oscillator consists of a nonlinear conductance $G_a(u)$ and a frequency determining network modeled by a lossy inductor and a capacitor and the load conductance $G$. The nonlinear conductance is described by

$$i_{Ga}(t) = G_a v(t) = -G_0(1 - bv^2(t))v(t) \quad \text{with} \quad G_0 > G \tag{2.39}$$

The resistance $R_L$ in series to the inductor $L$ is introduced in order to avoid an infinite conductivity in the inductor path. The resistance is assumed to be very small and therefore it can be neglected later.

In order to keep this example simple only the fundamental frequency is considered ($K = 1$). For the oscillator in Figure 2.4 the number of ports and the number of state variables is $N = 1$. Thus, the voltage vector $\mathbf{V}$ has 3 elements.

The admittance matrix for the linear subcircuit is a diagonal matrix with the elements

$$\mathbf{Y} = \begin{bmatrix} -\frac{1}{\mathrm{j}\,\omega L} - \mathrm{j}\,\omega C + G & 0 & 0 \\ 0 & \frac{1}{R_L} + G & 0 \\ 0 & 0 & \frac{1}{\mathrm{j}\,\omega L} + \mathrm{j}\,\omega C + G \end{bmatrix}. \tag{2.40}$$

The nonlinear contribution to the Jacobian matrix is determined by (2.37). The port indices $n$, $m$ are equal to one. Thus only the derivative

$$\frac{\partial}{\partial v} i_{\mathrm{Ga}}(v) = -G_0(1 - 3bv^2(t)) \tag{2.41}$$

needs to be considered in the Fourier transform. The differential conductance is voltage dependent and thus in a numerical solver it would be calculated for each iteration step. Here, we directly use the analytical solution of the van der Pol oscillator:

$$v^0(t) = V_1\left(\mathrm{e}^{-\mathrm{j}\,\omega_0 t} + \mathrm{e}^{\mathrm{j}\,\omega_0 t}\right) \tag{2.42}$$

with

$$V_1 = \sqrt{\frac{G_0 - G}{3bG_0}} \quad \text{and} \quad \omega_0 = \frac{1}{\sqrt{LC}}. \tag{2.43}$$

The higher harmonics are neglected in this example. The voltage state vector of the steady state solution is given by

$$\mathbf{V}^0 = \begin{bmatrix} V_1 \\ 0 \\ V_1 \end{bmatrix} \tag{2.44}$$

With the steady state solution the derivative in (2.41) results in

$$\frac{\partial}{\partial v} i_{\mathrm{Ga}}(v) = -G_0\left(1 - \tfrac{G_0 - G}{G_0}\left(\mathrm{e}^{-\mathrm{j}\,\omega_0 t} + \mathrm{e}^{\mathrm{j}\,\omega_0 t}\right)^2\right) \tag{2.45}$$

$$= -G_0 + (G_0 - G)\left(\mathrm{e}^{-\mathrm{j}\,2\omega_0 t} + 2 + \mathrm{e}^{\mathrm{j}\,2\omega_0 t}\right) \tag{2.46}$$

$$= G_0 - 2G + (G_0 - G)\left(\mathrm{e}^{-\mathrm{j}\,2\omega_0 t} + \mathrm{e}^{\mathrm{j}\,2\omega_0 t}\right) \tag{2.47}$$

and with (2.37) we determine the Fourier transform

$$\frac{\partial I_k}{\partial V_l} = \frac{1}{T}\int_0^T \left(G_0 - 2G + (G_0 - G)\left(\mathrm{e}^{-\mathrm{j}\,2\omega_0 t} + \mathrm{e}^{\mathrm{j}\,2\omega_0 t}\right)\mathrm{e}^{-\mathrm{j}\,(k-l)\omega_0 t}\right)\mathrm{d}t \tag{2.48}$$

and obtain the elements of the Jacobian matrix as

$$l = k: \quad \frac{\partial I_k}{\partial V_k} = G_0 - 2G \tag{2.49}$$

$$l = k+1: \quad \frac{\partial I_k}{\partial V_{k+1}} = \frac{1}{T}\int_0^T \left((G_0 - 2G)\mathrm{e}^{-\mathrm{j}\,\omega_0 t} + (G_0 - G)\left(\mathrm{e}^{-\mathrm{j}\,3\omega_0 t} + \mathrm{e}^{\mathrm{j}\,\omega_0 t}\right)\right)\mathrm{d}t = 0 \tag{2.50}$$

$$l = k-1: \quad \frac{\partial I_k}{\partial V_{k-1}} = 0 \tag{2.51}$$

$$l = k+2: \quad \frac{\partial I_k}{\partial V_{k+2}} = \frac{1}{T}\int_0^T \left((G_0 - 2G)\mathrm{e}^{-\mathrm{j}\,2\omega_0 t} + (G_0 - G)(\mathrm{e}^{-\mathrm{j}\,4\omega_0 t} + 1)\right)\mathrm{d}t = G_0 - G \tag{2.52}$$

$$l = k-2: \quad \frac{\partial I_k}{\partial V_{k-2}} = G_0 - G. \tag{2.53}$$

With these results the Jacobian for the van der Pole oscillator is

$$\mathbf{J}_\mathrm{F}(\mathbf{V}^0, \omega) = \begin{bmatrix} \mathrm{j}\left[-\frac{1}{-\omega L} - \omega C\right] + G_0 - G & 0 & G_0 - G \\ 0 & \frac{1}{R_\mathrm{L}} + G_0 - G & 0 \\ G_0 - G & 0 & \mathrm{j}\left[-\frac{1}{\omega L} + \omega C\right] + G_0 - G \end{bmatrix}. \tag{2.54}$$

## 2.2 Analysis of the Oscillator Phase Noise

### 2.2.1 Methods for Phase Noise Analysis

For the analysis of the phase noise in oscillator signals approaches based on linear and nonlinear oscillator models have been developed in the last decades. An encyclopedic overview of these methods is given in [49, 50].

The most common model based on linear oscillator theory is the empirical model of Leeson [65] in which a feedback oscillator consisting of an amplifier as active element that is described by its noise figure and a resonator with the quality factor $Q$ is used. Due to neglecting the nonlinear behavior of the oscillator circuit, however, modulation of the noise sources and noise mixing between harmonic frequencies can not be taken into account by these linear models.

For an accurate noise modeling of an oscillator a nonlinear treatment of the circuit is indispensable. The statistical properties of the noise processes of the circuit elements are the basis for the analysis. These noise processes can be described by a set of nonlinear Langevin equations that give the deterministic and the stochastic behavior of the oscillator [49, 50].

There are three groups of methods used for solving the Langevin equations: First, the direct solution of the Fokker-Planck equation, which can be established by the Langevin equations [66, 67]. This method allows to find an exact solution for the oscillator noise spectrum but entails a large numerical effort for oscillator circuits [59, 60].

In the second group of methods the Langevin equations are integrated numerically in the time domain [68]. The noise sources are implemented as random number generators. The spectrum of the oscillator signal is determined by averaging and Fourier transform. As with the first method, here an exact solution can be found. However, this method requires long integration times and thus it is unsuitable for complex circuits.

The third approach to solve the Langevin equations is limited to small signal perturbations of the steady state signal. This, however, is in most cases not a limitation as in the relevant type of operation the noise is small compared to the oscillating signal. This allows to use perturbation theory and the linearization of the differential equations around the steady state.

This approach is used by several authors [69–72] for the calculation of the oscillator signal amplitude and noise in simplified oscillators. Kärtner generalized this method for arbitrary complex oscillators in [73] by deriving a general expression for the correlation spectrum of an oscillator in the time domain. In [74, 75] Kärtner extends this method for $f^{-\alpha}$ noise sources. With the theory presented by Demir in [76] any desired colored noise source can be included in the analysis. In [49, 50] and [77] the conversion analysis approach is formulated in the frequency domain, which makes it compatible with harmonic balance methods.

The correlation matrix approach is currently the most common one for simulating noise in oscillators. Beside that, the method of time domain impulse sensitivity functions [78] is developed in 1998 by Hajimiri and Lee. In this theory the calculation of the Jacobian matrix is not required. The time-derivatives of the oscillator steady state solution are used for determining the tangential small signal perturbations of the limit cycle [78].

An analytical comparison of the two approaches is given by Suárez [79]. The approximate analytic calculation of the impulse sensitivity functions shows a good qualitative agreement with the conversion analysis approach, but is less accurate. This statement is validated in [80] in a comparative study by means of three different practical oscillators. Vanassche investigates in [81] into phase noise simulation of injection looked oscillators. He concludes that the method by impulse sensitivity functions in [78] is not accurate enough to analyze injection looked oscillators or generally any oscillator where the input sources are not stationary.

### 2.2.2 Phase Noise Analysis by Conversion Analysis

In the following the conversion analysis approach in frequency domain is considered. We focus on the work of Anzill [49,50] and extend this method by considering the oscillator phase noise at harmonic frequencies.

In this method, the noise sources are taken into account in the nonlinear system of equations as in (2.14) by the additional parameter $\mathbf{N}_\mathrm{T}$ representing the noise source vector.

$$\mathbf{F}(\mathbf{V}^0, \omega, \mathbf{N}_\mathrm{T}) \equiv \mathbf{0}. \tag{2.55}$$

The noise vector $\mathbf{N}_\mathrm{T}$ has the form of (2.10). The index T indicates that time windowed signals are considered for amplitude spectra of the random noise signals. As long as the oscillator is not operating close to its bifurcation point the noise sources can all be regarded as small signals compared to the oscillator signals [82]. Therefore they are considered in a linearized manner as

$$\mathbf{F}(\mathbf{V}^0, \omega) + \mathbf{G}(\mathbf{V}^0, \omega)\mathbf{N}_\mathrm{T} \equiv \mathbf{0} \tag{2.56}$$

with

$$\mathbf{G}(\mathbf{V}^0, \omega) = \left.\frac{\partial \mathbf{F}(\mathbf{V}, \omega)}{\partial \mathbf{N}_\mathrm{T}}\right|_{\mathbf{V}=\mathbf{V}^0, \mathbf{N}_\mathrm{T}=\mathbf{0}}. \tag{2.57}$$

The matrix $\mathbf{G}(\mathbf{V}^0, \omega)$ is the linear noise conversion matrix for the noise sources in the steady state regime of the oscillator.

As the noise signals can be regarded as small signals, the state variables and the oscillation frequency of the perturbed oscillator differ only by a small amount from the unperturbed case

$$\mathbf{V} = \mathbf{V}^0 + \delta\mathbf{V} \quad \text{with} \quad \|\delta\mathbf{V}\| \ll \|\mathbf{V}^0\| \tag{2.58}$$

$$\omega = \omega_0 + \omega_\mathrm{m} \quad \text{with} \quad \omega_\mathrm{m} \ll \omega_0. \tag{2.59}$$

The small amplitude deviation $\delta\mathbf{V}$ is taken into account in a linear manner by the Jacobian matrix defined in (2.29). As $\mathbf{F}(\mathbf{V}^0, \omega_0) \equiv \mathbf{0}$ is fulfilled in the steady state, Kirchhoff's current law (2.14) is now given by

$$\mathbf{J}_\mathrm{F}(\mathbf{V}^0, \omega)\delta\mathbf{V} + \mathbf{G}(\mathbf{V}^0, \omega)\mathbf{N}_\mathrm{T} = \mathbf{0}. \tag{2.60}$$

The Jacobian matrix contains the conversion parameters of the noise signals mixed with the spectral components of the state variables. At the steady state the Jacobian

matrix is singular [56] and thus it has one eigenvalue equal to zero, denoted by $\lambda_1 = 0$. This means that a distortion vector $\delta\mathbf{V}$ exists, so that $\mathbf{J}_\mathrm{F}(\mathbf{V}^0, \omega_0)\delta\mathbf{V} = \mathbf{0}$ and thus Kirchhoff's current law (2.14) is also fulfilled for $\mathbf{V}^0 + \delta\mathbf{V}$. This implies that the new solution $\mathbf{V}^0 + \delta\mathbf{V}$ differs from the steady state solution $\mathbf{V}^0$ only by a phase shift while the amplitudes in the state vector remain constant. The corresponding eigenvector points in the direction of the phase deviations. These stochastic phase fluctuations represent the oscillator phase noise [49, 50].

Deviations in the direction of the other eigenvectors with $\lambda_\mathrm{n} \neq 0$ with $n > 1$ describe amplitude noise. In this case $\mathbf{J}_\mathrm{F}(\mathbf{V}^0, \omega_0)\delta\mathbf{V} \neq \mathbf{0}$ and the steady state amplitudes vary. In contrast to phase deviations, here restoring forces towards the steady state take effect. Due to the decomposition in deviations tangential and normal to the limit cycle a definite separation of amplitude and phase noise is achieved.

As mentioned already above the Jacobian matrix is singular in the steady state. Thus, it cannot be inverted directly. To circumvent difficulties in inverting the Jacobian matrix, it is linearized with respect to frequency at the steady state oscillation frequency by

$$\mathbf{J}_\mathrm{F}(\mathbf{V}^0, \omega_0 + \omega_\mathrm{m}) = \mathbf{J}_\mathrm{F}(\mathbf{V}^0, \omega_0) + \omega_\mathrm{m}\mathbf{J}_\omega(\mathbf{V}^0, \omega_0) \tag{2.61}$$

with

$$\mathbf{J}_\omega(\mathbf{V}^0, \omega_0) = \left.\frac{\partial \mathbf{J}_\mathrm{F}(\mathbf{V}^0, \omega)}{\partial \omega}\right|_{\omega=\omega_0}. \tag{2.62}$$

For small offset frequencies $\omega_\mathrm{m}$, which are usually considered in a phase noise analysis this linearization is justified.

In the following an eigenvalue decomposition of the Jacobian $\mathbf{J}_F$ with left-sided eigenvectors $\mathbf{U}_\mathrm{j}$ and right-sided eigenvectors $\mathbf{W}_\mathrm{i}$ is performed in order to decompose the oscillator noise.

$$\mathbf{U}_j^+ \mathbf{J}_\mathrm{F}(\mathbf{V}^0, \omega_0) = \lambda_j^{\mathbf{U}} \mathbf{U}_j^+ \tag{2.63}$$

$$\mathbf{J}_\mathrm{F}(\mathbf{V}^0, \omega_0)\mathbf{W}_i^+ = \lambda_i^{\mathbf{W}} \mathbf{W}_i^+ \tag{2.64}$$

For a set of left- and right-sided eigenvectors the eigenvalues are equal $\lambda_j^{\mathbf{V}} = \lambda_i^{\mathbf{W}} = \lambda_i$ for $i = j$ and the orthogonality relation is valid

$$\mathbf{U}_j^+ \mathbf{W}_i = \delta_{ij} \quad \text{with} \quad \delta_{ij} = \begin{cases} 1 & i = j \\ 0 & i \neq j \end{cases} . \tag{2.65}$$

The right sided eigenvector $\mathbf{W}_1$ is the tangential vector on the steady state regime. It is given by

$$\mathbf{W}_1 = \mathrm{j}\,\omega_0 \boldsymbol{\Omega} \mathbf{V}^0 \tag{2.66}$$

with $\boldsymbol{\Omega}$ defined in (2.23).

The left sided eigenvector $\mathbf{U}_1$ is determined by the eigenvalue equation where $\lambda_1 = 0$, thus

$$\mathbf{J}^+(\mathbf{V}^0, \omega_0)\mathbf{U}_1 = \mathbf{0}. \tag{2.67}$$

$\mathbf{U}_1$ can be determined by LU-decomposition numerically [49, 50]. The length of the vector is chosen to fulfill the orthogonality relationship in (2.65). By applying the projector operator $\mathbf{W}_1\mathbf{U}_1$ to the noise sources in the steady state space the phase noise deviations are separated from the amplitude noise.

The physical representation of the eigenvectors $\mathbf{U}_\mathrm{i}$ and $\mathbf{W}_\mathrm{j}$ is illustrated in Figure 2.5. The time domain signal of two state variables $\mathbf{X}_1$ and $\mathbf{X}_2$ are drawn into a 2-dimensional diagram. The eigenvector $\mathbf{U}_1$ is tangential to the steady state.

The eigenvalues and eigenvectors for the perturbed Jacobian matrix $\mathbf{J}_\mathrm{F}(\mathbf{V}^0, \omega_0 + \omega_\mathrm{m})$ are given by

$$\lambda_i' = \lambda_i + \delta\lambda_i \quad \text{with} \quad |\delta\lambda_i| \ll |\lambda_i|, \tag{2.68}$$

$$\mathbf{U}_j'^+ = \mathbf{U}_j^+ + \delta\mathbf{U}_j^+ \quad \text{with} \quad \|\delta\mathbf{U}_j\| \ll \|\mathbf{U}_j\|, \tag{2.69}$$

$$\mathbf{W}_i'^+ = \mathbf{W}_i^+ + \delta\mathbf{W}_i^+ \quad \text{with} \quad \|\delta\mathbf{W}_i\| \ll \|\mathbf{W}_i\|. \tag{2.70}$$

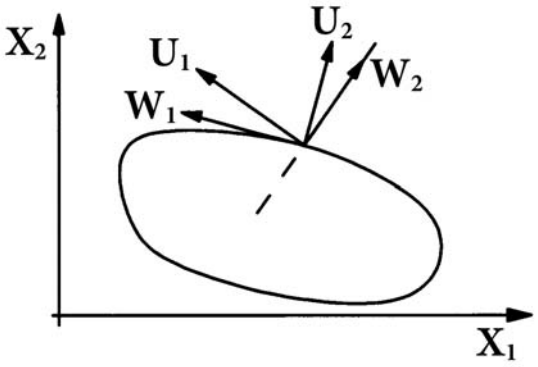


Figure 2.5: Physical representation of the eigenvectors $\mathbf{U}_\mathrm{i}$ and $\mathbf{W}_\mathrm{j}$ [49,50]

The deviation of the eigenvalue $\lambda_1$ is calculated in [49,50] under the assumption of the Jacobian matrix linearized with respect to frequency by

$$\delta\lambda_i = \omega_\mathrm{m}\mathbf{U}_i^+\mathbf{J}_\omega(\mathbf{V}^0,\omega_0)\mathbf{W}_i \tag{2.71}$$

and with $\lambda_1 = 0$ and (2.66) we get

$$\lambda_1' = \delta\lambda_1 = \omega_\mathrm{m}\mathbf{U}_1^+\mathbf{J}_\omega(\mathbf{V}^0,\omega_0)\mathrm{j}\,\omega_0\mathbf{\Omega}\mathbf{V}^0. \tag{2.72}$$

With these eigenvectors the Jacobian matrix and its inverse can now be expressed by

$$\mathbf{J}(\mathbf{V}^0,\omega) = \sum_{i=1}^{n(2k+1)} \lambda_i'\mathbf{W}_i'\mathbf{U}_i'^{+} \quad \text{and} \tag{2.73}$$

$$\mathbf{J}^{-1}(\mathbf{V}^0,\omega) = \sum_{i=1}^{n(2k+1)} \frac{1}{\lambda_i'}\mathbf{W}_i'\mathbf{U}_i'^{+}. \tag{2.74}$$

Instead of calculating the inverse of the bad conditioned Jacobian matrix numerically, (2.73) is used to rewrite (2.60)

$$\delta \mathbf{V}_{\mathrm{T}} = \sum_{i=1}^{n(2k+1)} \frac{1}{\lambda_i'} \mathbf{W}_i' \mathbf{U}_i'^{+} \left( -\mathbf{G}(\mathbf{V}^0, \omega) \mathbf{N}_{\mathrm{T}} \right). \tag{2.75}$$

The correlation spectra of the noise sources $\mathbf{C}^{\mathrm{N}}(\omega)$ and the deviations of the state vector $\mathbf{C}^{\delta V}(\omega)$ are defined by

$$\mathbf{C}^{\mathrm{N}}(\omega) = \lim_{T \to \infty} \frac{1}{2T} \left\langle \mathbf{N}_{\mathrm{T}}(\omega) \mathbf{N}_{\mathrm{T}}^{+}(\omega) \right\rangle \tag{2.76}$$

$$\mathbf{C}^{\delta V}(\omega) = \lim_{T \to \infty} \frac{1}{2T} \left\langle \delta \mathbf{V}(\omega) \delta \mathbf{V}^{+}(\omega) \right\rangle. \tag{2.77}$$

where the brackets denote ensemble averages. With (2.75) and

$$\left\langle \mathbf{W}_i \mathbf{U}_i^{+} \mathbf{G} \mathbf{N}_{\mathrm{T}} \mathbf{N}_{\mathrm{T}}^{+} \mathbf{G}^{+} \mathbf{U}_j \mathbf{W}_j^{+} \right\rangle = \mathbf{U}_i^{+} \mathbf{G} \left\langle \mathbf{N}_{\mathrm{T}} \mathbf{N}_{\mathrm{T}}^{+} \right\rangle \mathbf{G}^{+} \mathbf{U}_j \mathbf{W}_i \mathbf{W}_j^{+} \tag{2.78}$$

and

$$\mathbf{C}^{\mathrm{GN}}(\omega) = \mathbf{G}(\mathbf{V}^0, \omega) \mathbf{C}^{\mathrm{N}}(\omega) \mathbf{G}^{+}(\mathbf{V}^0, \omega) \tag{2.79}$$

we obtain the noise correlation matrix of the oscillator circuit

$$\mathbf{C}^{\delta V}(\omega) = \sum_{i=1}^{n(2k+1)} \sum_{i=1}^{n(2k+1)} \frac{1}{\lambda_i' \lambda_j'^{*}} \mathbf{U}_i'^{+} \mathbf{C}^{\mathrm{GN}}(\omega) \mathbf{U}_j' \mathbf{W}_i' \mathbf{W}_j'^{+}. \tag{2.80}$$

In $\mathbf{C}^{\delta V}(\omega)$ all noise processes are enclosed. The correlation spectrum for the phase deviations $\mathbf{C}^{\varphi}(\omega)$ is determined by applying the projection operator $\mathbf{W}_1' \mathbf{U}_1'^{+}$

in (2.80). The deviations $\delta\mathbf{V}_1$ and $\delta\mathbf{W}_1$ of the eigenvectors are by a factor of about $\omega_\mathrm{m}/\omega_0$ smaller than the eigenvectors. Therefore, these deviations can be neglected and we approximate $\mathbf{U}_1' \approx \mathbf{U}_1$ and $\mathbf{W}_1' \approx \mathbf{W}_1$ and achieve

$$\mathbf{C}^{\varphi}(\omega) = \frac{1}{|\lambda_1'|^2}\mathbf{U}_1^{+}\mathbf{C}^{\mathrm{GN}}(\omega)\mathbf{U}_1\mathbf{W}_1\mathbf{W}_1^{+} = \frac{\mathbf{U}_1^{+}\mathbf{C}^{\mathrm{GN}}(\omega)\mathbf{U}_1\mathbf{\Omega}\mathbf{V}^0\mathbf{V}^{0+}\mathbf{\Omega}}{\omega_\mathrm{m}^2|\mathbf{U}_1^{+}\mathbf{J}_\omega(\mathbf{V}^0,\omega_0)\mathbf{\Omega}\mathbf{V}^0|^2}. \tag{2.81}$$

The coefficients in the matrix $\mathbf{\Omega}\mathbf{V}^0\mathbf{V}^{0+}\mathbf{\Omega}$ in (2.81) scale the noise correlation factor $\mathbf{C}^{\varphi}(\omega)_{n,m,k,l}$ between the nodes $n$ and $m$ and the frequencies $k\omega_0$ and $l\omega_0$. For $n = m$ and $k = l$ the scaling factor for the noise autocorrelation factors are

$$\mathbf{\Omega}\mathbf{V}^0\mathbf{V}^{0+}\mathbf{\Omega}_{n,n,k,k} = k^2|V_{n,k}^0|^2. \tag{2.82}$$

The phase noise of oscillators is characterized by the single-sideband phase noise $\mathcal{L}(\omega_\mathrm{m})$ at an offset frequency $\omega_\mathrm{m}$ from the carrier. It is the ratio of the noise power $P_{\mathrm{N},n}(\omega)$ in a single sideband in a bandwidth of 1 Hz at an offset frequency $\omega_\mathrm{m}$ from the carrier frequency and the total signal power $P_{\mathrm{S},n}$ at node $n$.

$$\mathcal{L}_{n,k}(\omega_\mathrm{m}) = \frac{P_{\mathrm{N},n,k}(\omega_\mathrm{m})}{P_{\mathrm{S},n,k}}. \tag{2.83}$$

The phase noise power that would be delivered to a normalization resistance $R_\mathrm{N}$ at the $k$th harmonic frequency at node $n$ is

$$P_{\mathrm{N},n,k}(\omega_\mathrm{m}) = 2R_\mathrm{N}\mathbf{C}_{n,k}^{\delta V}(f_0 + f_\mathrm{m}) \tag{2.84}$$

$$= 2R_\mathrm{N}\frac{\mathbf{U}_1^{+}\mathbf{C}^{\mathrm{GN}}(\omega_0+\omega_\mathrm{m})\mathbf{U}_1 k^2|V_{n,k}^0|^2}{\omega_\mathrm{m}^2|\mathbf{U}_1^{+}\mathbf{J}_\omega(\mathbf{V}^0,\omega_0)\mathbf{\Omega}\mathbf{V}^0|^2}. \tag{2.85}$$

The noise power in the considered 1 Hz bandwidth is assumed to be constant. For offset frequencies $f_\mathrm{m} >> 1\,\mathrm{Hz}$ this assumption is justified, as the phase noise decays

with $f_m^{-\alpha}$ in general. With the oscillator signal power at the $k$th harmonic frequency at node $n$

$$P_{\mathrm{S},n,k} = 2R_{\mathrm{N}}|V_{n,k}^0|^2 \tag{2.86}$$

we obtain the single side band phase noise at the $k$th harmonic frequency

$$\mathcal{L}_{n,k}(\omega_{\mathrm{m}}) = \frac{\mathbf{U}_1^+\mathbf{C}^{\mathrm{GN}}(\omega_0+\omega_{\mathrm{m}})\mathbf{U}_1 k^2}{\omega_{\mathrm{m}}^2|\mathbf{U}_1^+\mathbf{J}_\omega(\mathbf{V}^0,\omega_0)\mathbf{\Omega}\mathbf{V}^0|^2} \tag{2.87}$$

$$= \frac{\omega_0^2}{|\lambda_1'|^2}\mathbf{U}_1^+\mathbf{C}^{\mathrm{GN}}(\omega_0+\omega_{\mathrm{m}})\mathbf{U}_1 k^2. \tag{2.88}$$

From (2.87) it can be seen that the phase noise power scales with the square of the harmonic index $k$. Thus e. g. at the second harmonic frequency $2\omega_0$ the phase noise level is 6 dB higher than at the fundamental frequency $\omega_0$. The following model can describe this fixed ratio: a phase disturbance $\Delta\varphi$ of the fundamental frequency occurs at the $k$th harmonic by a phase change by $k\Delta\varphi$.

When only white noise sources are considered $\mathcal{L}(\omega_{\mathrm{m}})$ decrements by 20 dB per frequency decade. For $f^{-\alpha}$ noise sources the correlation spectrum $\mathbf{C}^{\mathrm{GN}}$ scales proportional by $f^{-\alpha}$ and thus the single side band phase noise reduces with $(20+10\alpha)$ dB per decade. Different kind of noise sources in one circuit result in an overlapping of the various kinds of frequency decays, which can be recognized in the phase noise spectrum of the output signal.

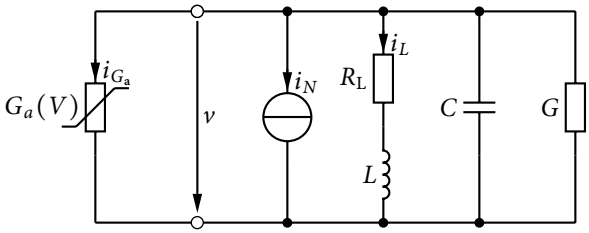


Figure 2.6: Van der Pol oscillator with current noise source

### 2.2.3 Example: Phase Noise of the Van der Pol Oscillator

The method described above is used now to analyze the phase noise characteristic of the van der Pol oscillator described in section 2.1.3. The noise source is described by a zero-mean gaussian white noise current source denoted in Figure 2.6 by $i_N$. This noise source could also include $f^{-\alpha}$ noise. The noise correlation matrix $\mathbf{C}^{\mathrm{I_r}}$ of the noise current source is

$$\mathbf{C}^{\mathrm{I_r}} = \sigma \begin{bmatrix} 1 & 0 & 0 \\ 0 & 1 & 0 \\ 0 & 0 & 1 \end{bmatrix} \tag{2.89}$$

and the noise conversion matrix defined in (2.57) is

$$\mathbf{G} = \begin{bmatrix} 1 & 0 & 0 \\ 0 & 1 & 0 \\ 0 & 0 & 1 \end{bmatrix}. \tag{2.90}$$

Thus $\mathbf{C}^{\mathrm{GI_r}} = \mathbf{C}^{\mathrm{I_r}}$. The Jacobian matrix that describes the linearization around the steady state of the oscillator in (2.54) is now considered at the shifted frequency $\omega = \omega_0 + \omega_{\mathrm{m}}$

$$\mathbf{J}_{\mathrm{F}}(\mathbf{V}^0,\omega)=\begin{bmatrix} \mathrm{j}\left[-\frac{1}{(-\omega_0+\omega_{\mathrm{m}})L}(-\omega_0+\omega_{\mathrm{m}})C\right]+ & 0 & G_0-G \\ +G_0-G & & \\ 0 & \frac{1}{R_{\mathrm{L}}+\mathrm{j}\,\omega_{\mathrm{m}}L}+\mathrm{j}\,\omega_{\mathrm{m}}C+ & 0 \\ & +G_0-G & \\ G_0-G & 0 & \mathrm{j}\left[-\frac{1}{(\omega_0+\omega_{\mathrm{m}})L}+(\omega_0+\omega_{\mathrm{m}})C\right]+ \\ & & +G_0-G \end{bmatrix}. \tag{2.91}$$

Based on that, the Jacobian matrix linearized with respect to frequency is calculated after (2.62). With the oscillation frequency in (2.43), small offset frequencies compared to the carrier frequency ($\omega_{\mathrm{m}} \ll \omega_0$) and a negligible series resistance ($R_{\mathrm{L}} \ll \omega_0 L$) we obtain

$$\mathbf{J}_{\omega}(\mathbf{V}^0,\omega_0)=\left.\frac{\partial \mathbf{J}_{\mathrm{F}}(\mathbf{V}^0,\omega)}{\partial\omega}\right|_{\omega=\omega_0}=\begin{bmatrix} \mathrm{j}2C & 0 & 0 \\ 0 & \mathrm{j}C-\frac{\mathrm{j}L}{R_{\mathrm{L}}} & 0 \\ 0 & 0 & \mathrm{j}2C \end{bmatrix}. \tag{2.92}$$

The first eigenvalue of the Jacobian matrix at the oscillation frequency $\omega_0$ is $\lambda_1 = 0$. At the offset frequency $\omega_{\mathrm{m}}$ the first eigenvalue for the perturbed Jacobian matrix is determined by (2.72)

$$\lambda_1' = \mathrm{j}2\omega_{\mathrm{m}}C. \tag{2.93}$$

The unperturbed left-sided and the right-sided eigenvectors are determined with

(2.66) and (2.67) as

$$\mathbf{W}_1 = \mathrm{j}\,\omega_0 V_1 \begin{bmatrix} -1 \\ 0 \\ 1 \end{bmatrix} \tag{2.94}$$

$$\mathbf{U}_1 = -\frac{\mathrm{j}}{2\omega_0 V_1} \begin{bmatrix} 1 \\ 0 \\ -1 \end{bmatrix}. \tag{2.95}$$

Thus, the single sideband phase noise is given by (2.87)

$$\mathcal{L}_{n,k}(\omega_\mathrm{m}) = \frac{\omega_0^2}{|\lambda_1'|^2}\mathbf{U}_1^+ \mathbf{C}^{\mathrm{GI_r}} \mathbf{U}_1 \tag{2.96}$$

$$= \frac{\omega_0^2}{4\omega_\mathrm{m}^2 C^2} \frac{2\sigma}{4\omega_0^2 |V_1|^2} \tag{2.97}$$

$$= \frac{\sigma}{8\omega_\mathrm{m}^2 C^2 |V_1|^2}. \tag{2.98}$$

With the quality factor $Q = \omega_0 C/G$, the oscillator signal power $P_S = 2|V_1|^2 G$ and the noise correlation density $\sigma = \frac{1}{2} FkTG$ the single side band phase noise is be expressed by

$$\mathcal{L}_{n,k}(\omega_\mathrm{m}) = \frac{\omega_0^2 FkT}{8\omega_\mathrm{m}^2 Q^2 P_\mathrm{S}}. \tag{2.99}$$

This result agrees with the analytical solutions found by Leeson [65].

### 2.2.4 Oscillator Phase Noise Analysis Conclusion

We have investigated on the theory of oscillator phase noise analysis by the conversion method. The method of Anzill in [49, 50] has been extended for the oscillator phase noise analysis at harmonic frequencies. Since in a push-push oscillator the second harmonic frequency is coupled to the output, the phase noise analysis at this frequency is of great interest for this type of oscillators.

A comparison of the method by Anzill, which is described above, with the method by Rizzoli [77] shows that Anzill's method with the eigenvector decomposition is simpler to use. However, it does not use the frequency of oscillation as an unknown when the noise sources are introduced. In an autonomous system this frequency, however, can be affected by the noise perturbations. This limitation is expected to take effect especially at small offset frequencies, e. g. below 1 kHz when the oscillation frequency is in the microwave range. For most applications at these frequencies this is not a limitation, since the oscillator phase noise is mostly specified at offset frequencies at 100 kHz or 1 MHz.

Due to the higher accuracy at low offset frequencies from the carrier, Rizzoli's method has been implemented in several commercial simulators (e. g. Advanced Design System (ADS) of Agilent, Microwave Office of Advanced Wave Research (AWR), Spectre of Cadence).

The implementation of the method described above requires two steps: First the steady state solution and the Jacobian matrix need to be calculated as described in section 2.1.2. These results of the unperturbed oscillator are then used for the oscillator phase noise analysis. The steady state calculation is already standard in commercially available circuit simulators. However, the Jacobian matrix that is needed for the phase noise analysis cannot be extracted from these programs. Inquiries at the companies Agilent and AWR during this work have shown that they are not willing to give out the Jacobian matrix – not even for research purposes.

The calculation of the Jacobian matrix would have required the implementation of a complete harmonic balance circuit simulator. This, however, would have gone beyond the scope of this work and thus, also the phase noise analysis method has not been implemented. The principles of the phase noise theory, however, have been a basis for the design of the oscillators described in chapter 5.

# Chapter 3

# Push-Push Oscillators

## 3.1 The Push-Push Oscillator Principle

The maximum oscillation frequency that can be reached by a fundamental frequency oscillator is primarily limited by the active devices used. For transistor-based oscillators the maximum frequency of oscillation $f_{\max}$ is given by the frequency where the maximum available gain of the device is reduced to one.

For extending the frequency range for a given technology the harmonic frequency content of the oscillator signal can be coupled out. In order to increase the signal power at harmonic frequencies the nonlinearities in the oscillator need to be enhanced. This can be reached by a large signal drive of the nonlinear characteristics of the active devices or by adding a multiplier stage at the oscillator output. In any of these cases, however, the output signal needs to be filtered to achieve a purely sinusoidal output signal.

A push-push oscillator combines both, the harmonic frequency content generation and the cancellation of the unwanted frequency contributions at once. It consists of two equal suboscillators operating in odd mode at the fundamental frequency $f_0$ as depicted in Figure 3.1. Nonlinear distortion in the suboscillators cause harmonic frequency contributions in the output signals $s_1(t)$ and $s_2(t)$ of the suboscillators at the $n$th harmonic $f_{\mathrm{n}} = nf_0$. The output signals are given by

$$s_1(t) = \sum_{n=0}^{\infty} a_n \cdot \sin(n\omega_0 t + \varphi_n) \tag{3.1}$$

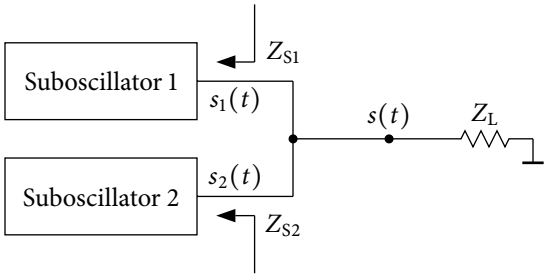


Figure 3.1: Principle of the push-push oscillator

$$s_2(t) = \sum_{n=0}^{\infty} a_n \cdot \sin(n\omega_0 t + \varphi_n + \Delta\varphi_n). \tag{3.2}$$

Due to the odd mode operation of the suboscillators the phase differences of the frequency contributions of the two output signals are given by

$$\Delta\varphi_n = n\pi. \tag{3.3}$$

At the common output port the output signals are added up to the output signal of the push-push oscillator

$$s(t) = s_1(t) + s_2(t) = \sum_{n=2,4,\ldots}^{\infty} 2 \cdot a_n \cdot \sin(\omega_0 t + \varphi_n). \tag{3.4}$$

The fundamental frequency and the odd harmonics cancel out, while the even harmonics add in phase as demonstrated in Figure 3.2. Hence, power is delivered to the load only at the even harmonics $f_2, f_4, \ldots$ [83–85]. An ideal suppression is achieved only when both oscillators operate stable at the same frequency in odd mode and show the same signal power at each frequency contribution.

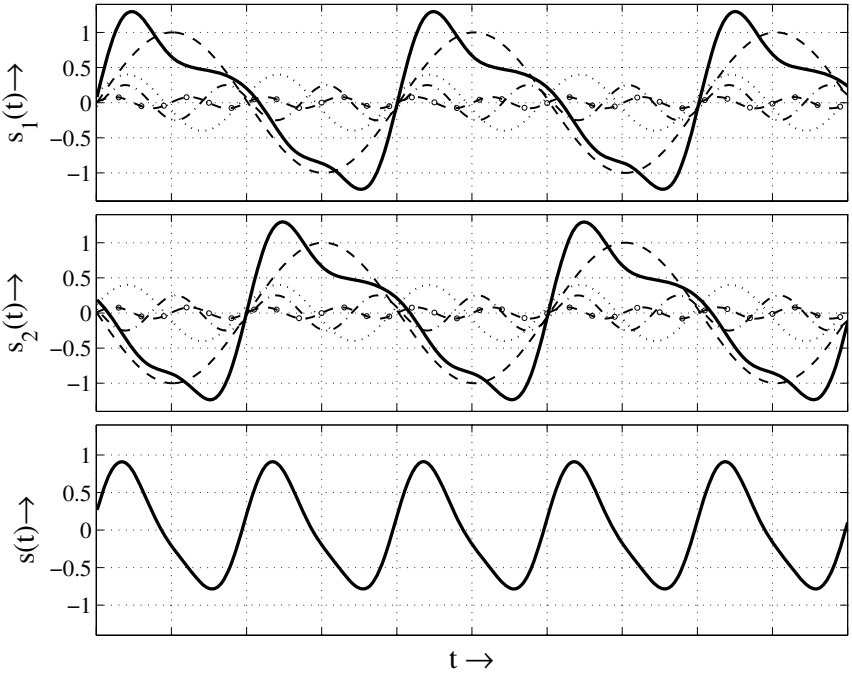


Figure 3.2: Output signals $s_1(t)$ and $s_2(t)$ of the two subcircuits (solid lines) with their harmonic frequency contributions plotted individually (dotted lines) and the sum $s(t)$ of the combined signals

The push-push principle was known already in the 1930's when push-push doublers were realized [86]. The first push-push oscillator published dates to 1983 [83]. John B. Bender and Colmon Wong predict the push-push topology for the realization of bipolar transistor oscillators at *X*-band and above. To verify the design theory a 200-MHz push-push oscillator was built and measured. The experiments showed that by distorting the current waveforms in the active devices, their second harmonic content increases and therefore the output power of the push-push oscillator rises.

## 3.2 Properties of Push-Push Oscillators

The push-push oscillator principle shows several advantages over a conventional fundamental frequency oscillator. First of all, the push-push principle allows to extend the usable frequency range of an active device as the signal power at the second harmonic frequency is used. In [87] a push-push oscillator is reported that exceeds the transient frequency $f_T$ and the maximum frequency of oscillation $f_{max}$ by a factor of 1.5.

Compared to solutions using frequency multipliers or doublers, a push-push oscillator is generally less space consuming. Hyun et al present in [88] a comparison of the two design options with hairpin resonator based oscillators. The size of the push-push oscillator is by a factor of three smaller than the realization with a frequency doubler without considering the size of the required filter.

Additionally push-push oscillators are highly resistant to load pulling effects [89–91]. The suboscillators are terminated by 'virtual grounds' for the fundamental frequency and only the second harmonic frequency component is influenced by variations of the oscillators load impedance.

As the two suboscillators operate at halve of the output frequency this frequency contribution can be coupled to an additional output port. Thus, the first frequency divider that would be needed in a PLL circuit can be saved.

The temperature sensitivity of a push-push oscillator is generally lower compared to a fundamental frequency oscillator because at the halved oscillation frequency the temperature sensitivity of the active devices is reduced. This is proved by the comparison of *W*-band push-push oscillators presented in [27, 29] and the fundamental frequency oscillator in [16], which are all build with the same technology.

The fundamental frequency inherent in the suboscillators needs to be specially considered in a push-push oscillator. For optimum suppression, attention must be paid on a symmetric circuit design, layout and fabrication. With a monolithical integrated realization the best suppression of the fundamental frequency in the output signal is reached. As high signal amplitudes at fundamental frequency in the suboscillators occur, the electromagnetic compatibility at this frequency needs to be taken care of.

## 3.3 Phase Noise of Push-Push Oscillators

Phase noise is one of the most essential criteria whether a specific oscillator can be used in an intended application. Therefore, in this section the phase noise characteristics of a push-push oscillator compared to a fundamental frequency oscillator are considered.

In (2.87) a general expression for the single side band phase noise of an oscillator is given. A general dependency of the oscillator phase noise on the frequency of oscillation, however, cannot be derived directly form this equation. It can only be applied to a specific type of oscillator and then a relation for the phase noise versus the frequency of oscillation can be given as in the example of the van der Pol oscillator in (2.99). As shown in the example and as commonly known from realized oscillators, the phase noise power scales generally with $\omega_0^2$ when all other parameters are kept constant. This relation is incorporated in various figures of merit definitions for oscillators available in literature [92–95].

When the oscillation frequency is changed, however, not all other parameters can be kept constant. The $Q$-factor that can be reached with one type of resonator decreases usually with increasing frequency. Additionally some types of resonators as for example dielectric resonators or quartz resonators cannot be used in a fundamental frequency oscillator with a too high oscillation frequency, but can be used in the suboscillators of a push-push oscillator with the same output frequency. Furthermore in a push-push oscillator the fundamental frequency is not damped by the oscillators load impedance because in odd mode operation a virtual ground exists at the common output port for the fundamental frequency. Therefore, in a push-push oscillator the loaded $Q$-factor is equal to the unloaded $Q$-factor, which results in an overall increased $Q$-factor.

For the generation of the oscillation signal in the suboscillators active devices with lower noise can be used. Field effect transistors (FET) and high electron mobility transistors (HEMT) providing high $f_T$ and $f_{max}$ values can be replaced by the slower heterojunction bipolar transistors (HBT) showing inherently lower $1/f$ noise characteristics [96]. Secondly slower transistors with a larger size exhibiting lower $1/f$ noise due to reduced current densities can be utilized. We can sum up these considerations by a factor of $(6 + \alpha)$ dB, with $\alpha > 0$, describing the phase noise reduction when the oscillation frequency is halved.

The noise sources in the two suboscillators can be regarded as uncorrelated as they are originated from different, independent devices. At the output terminal of the push-push oscillator the second harmonic carrier powers add up while the uncorrelated noise power remains constant [97, 98]. This results in a single sideband phase noise reduction by 3 dB with respect to the total signal power at the second harmonic frequency.

Therefore, the overall phase noise reduction that can be achieved by a push-push oscillator compared to a conventional oscillator cannot be expressed by a factor or a general equation. Due to the halved oscillation frequency of the suboscillators the phase noise of the fundamental frequency is $(6 + \alpha)$ dB lower and the phase noise of the second harmonic frequency is $\alpha$ dB lower than for a fundamental frequency oscillator. The summation of the suboscillator signals results in a decrease of the phase noise level with respect to the carrier by 3 dB. Thus, the complete phase noise reduction of a push-push oscillator is $(3 + \alpha)$ dB.

## 3.4 Design of Push-Push Oscillators

The main drawback of the push-push oscillator principle is the more complicated circuit design than that of a fundamental frequency oscillator. The two suboscillators need to be designed for an odd mode operation while an even mode operation must be prevented. For the analysis the circuit is cut at the symmetry line and this way the problem is reduced to a single oscillator that can be investigated depending on the mode of operation.

The resulting equivalent circuits, one for the odd and one for the even mode, are drawn in Figure 3.3. In the odd mode case the common port can be represented by a virtual ground, because the voltages cancel out. In the even mode, no voltage difference between two symmetric points occurs and thus there is no current between

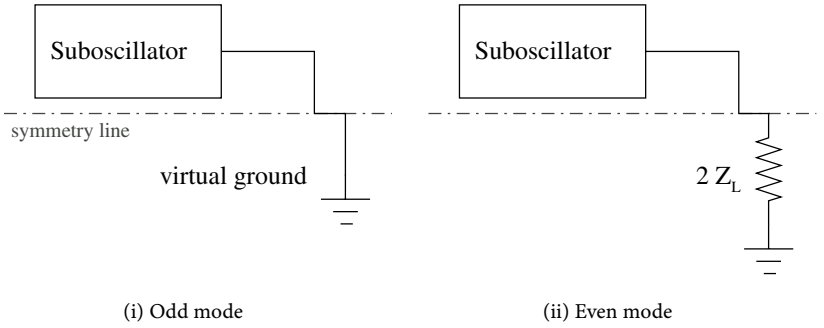


Figure 3.3: Equivalent circuits for the modes of operation of a suboscillator

them. Hence, any resistor symmetric to the symmetry line and crossing this line can be removed in this equivalent circuit. The load impedance $Z_\mathrm{L}$ is split into two parallel impedances, each with a resistance of $2 \cdot Z_\mathrm{L}$.

In the circuit design, first the small signal case is considered as described in section 2.1.1. For considering the small signal oscillation condition the suboscillator is approximated by an one-port connected to its respective termination impedance as in Figure 3.3. Thus, the small signal oscillation condition for the suboscillator in odd mode operation is given by

$$Z_\mathrm{S}(s_0) = 0. \tag{3.5}$$

The unwanted even-mode oscillation must be suppressed to ensure a stable odd-mode operation. This is unconditionally fulfilled, when the negative real part of the suboscillator impedance $-\Re\{Z_\mathrm{S}\}$ is smaller than two times the real part of the oscillator load impedance $2 \cdot \Re\{Z_\mathrm{L}\}$

$$-\Re\{Z_\mathrm{S}(s)\} < 2 \cdot \Re\{Z_\mathrm{L}(s)\}. \tag{3.6}$$

Thus, the load resistance attenuates even mode signals and prevents the startup of even mode oscillations. When the assumptions for the validity of the startup condi-

tions (2.5) and (2.6) are fulfilled, then for the startup of an odd mode oscillation the real part of the suboscillator input impedance $\Re\{Z_S\}$ needs to be negative and the derivation of the imaginary part $\Im\{Z_S\}$ with respect to frequency needs to be positive. Thus the following startup conditions for a push-push oscillator can be given:

$$0 < -\Re\{Z_S(s_0)\} < 2 \cdot \Re\{Z_L(s_0)\} \tag{3.7}$$

$$\frac{\partial \Im\{Z_S(s_0)\}}{\partial \omega} > 0. \tag{3.8}$$

This condition needs to be fulfilled in the whole tuning range of the oscillator. At any other frequency, any oscillation must be prevented. Therefore, the real part of the suboscillator impedance must be $\Re\{Z_S\} > 0$ at these frequencies.

When the small signal oscillation conditions are fulfilled, the two suboscillators can be combined. Then the resulting push-push oscillator is analyzed in a nonlinear manner as described in section 2.1.2 and section 2.2.

# Chapter 4

# Design Considerations for the Push-Push Oscillators

## 4.1 Fabrication Technology

For the realization of millimeter-wave oscillators MMIC technologies or hybrid integrated realizations can be principally used. The latter shows generally the advantage of higher available resonator $Q$-factors. However, due to the parasitics added in a realization with single transistors, the usable frequency range is limited considerably. Additionally in an integrated circuit fabrication, a maximum in symmetry of the active devices can be achieved as they are fabricated close together on the same wafer. Thus, a high fundamental frequency suppression in the output signal of the push-push oscillator can be reached.

In order to combine high-$Q$ resonators with high symmetry in [99] a push-push oscillator with an active MMIC part and an external resonator is realized. Such a partially monolithical integration, and also hybrid solutions, however, cannot compete with MMIC realizations in terms of size and weight. Moreover, when the number of circuits to be fabricated is large enough the MMIC fabrication is generally the most cost efficient.

Conventionally oscillators for millimeter-wave frequencies are built on III/V semiconductor based technologies. Recent advances in SiGe heterojunction bipolar transistors (HBTs) [2–5], however, have increased the usable frequency range of SiGe devices in the last few years. This allows the SiGe technology to compete now with III/V devices at these frequencies.

The low noise level at low frequencies (LF) and the resulting low oscillator phase noise are areas in which SiGe HBTs generally outperform III/V HBTs or high electron mobility transistors (HEMTs) [6]. The significant lower costs of SiGe chip area can reduce the prices of millimeter-wave systems and thus it has the potential to open mass markets for consumer systems at millimeter-wave and submillimeter-wave frequencies.

For the intended application of the push-push oscillator in an automotive radar system a MMIC realization based on SiGe HBTs is therefore promising. In this work we make use of the production-near SiGe:C bipolar technology of INFINEON TECHNOLOGIES [2, 100] for the realization of the designed circuits. In the following two sections the characteristics of this technology are presented and resulting design issues are considered.

## 4.2 Active Structures

### 4.2.1 Properties of the SiGe HBTs

The SiGe:C transistors make use of a double-polysilicon self-aligned emitter-base configuration. The minimum effective emitter width is 0.14 µm. The SiGe:C base is integrated by using a selective epitaxial growth [2]. The maximum transit frequency $f_T$ is 200 GHz and the maximum frequency of oscillation $f_{max}$ is 275 GHz as can be seen in Figure 4.1.

The optimum collector current density $J_{C,opt}$ is 8 mA/µm$^2$ for maximum $f_T$ and $f_{max}$. For lower current densities these maximum ratings are approximately proportional to the collector current density. When the collector current exceeds the optimum current density $J_{C,opt}$, high current effects occur. The main effect in SiGe HBTs is the *Kirk-effect* [101], while the *Webster-Rittner effect* [102, 103] can be typically neglected in these devices due to the relatively high doping level in the base region [104–106].

The physical principle of the Kirk-effect lies in recombination processes in the collector-base region. The increased minority carrier concentration compensates the background ionized donor density of the collector. This causes the original electric field on the collector-base junction to collapse and being pushed further into the collector region when the current density rises. This displacement increases the effective base-width, which is referred to as *base push-out*. The increase of the effective

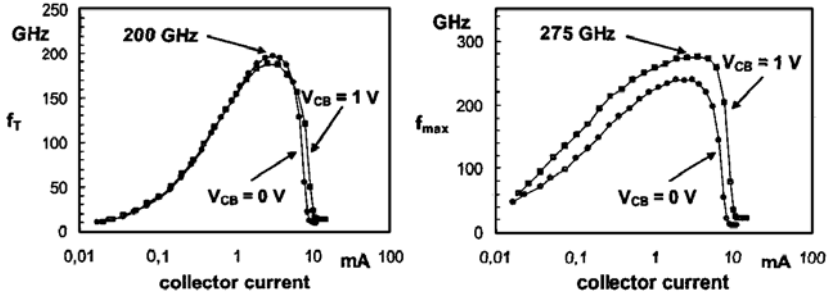


Figure 4.1: Transit frequency $f_T$ and maximum frequency of oscillation $f_{max}$ versus collector current of a SiGe HBT with an emitter size $A_E = 0.14 \times 2.6\,\mu m^2$ extrapolated from measurements up to 30 GHz [2]

base width is called the *current-induced base-width*. The base delay time $\tau_B$ increases and thus the transit frequency $f_T$ and the maximum frequency of oscillation $f_{max}$ drop. Due to the typical dotting profiles of HBTs, the Kirk-effect appears stronger than in conventional bipolar transistors, which can be seen in the steep roll-off loci of $f_T$ and $f_{max}$.

The output characteristics of one SiGe HBT is shown in Figure 4.2. It can be seen that the collector-emitter breakdown voltage $BV_{CEO}$ is 1.7 V. When this voltage is exceeded the base current gets negative due to increased impact ionization [107,108] and majority carriers flow out of the base. In this case the collector current $I_C$ rises and the device breaks down. In the circuit design therefore a biasing for the HBTs that is not sensitive for negative base currents needs to be found (see section 4.2.2).

The fabrication technology offers different transistor configurations and various lengths of the active areas. For the circuits designed in this work the collector-emitter-base-emitter-collector (cebec) configuration with the maximum available emitter length of 10 µm is used. This results in a total effective emitter area of $2 \times 10\,\mu m \times 0.14\,\mu m = 2.8\,\mu m^2$. The optimum collector current $I_C$ for $f_T$ and $f_{max}$ is therefore 22.4 mA.

For the modeling of the HBTs an extended Gummel-Poon model [109] provided by Infineon Technologies is used. As long as the transistors are not operated

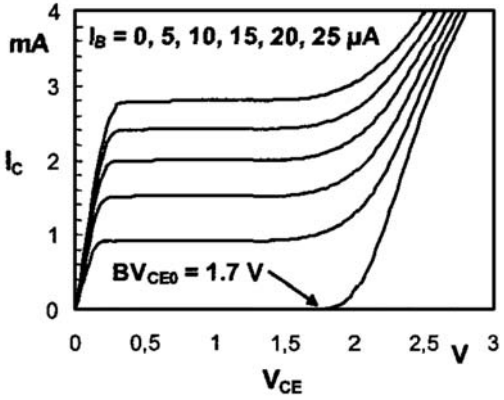


Figure 4.2: Measured output characteristics for different base currents $I_B$ of a SiGe HBT for an emitter size $A_E = 0.14 \times 2.6\,\mu m^2$ [2]

in the high current region or close to their voltage breakdown the Gummel-Poon model is an accurate large signal model for the transistors.

### 4.2.2 Optimum Biasing of the SiGe HBTs

In order to achieve a maximum oscillator output power a bias point allowing a high voltage swing and a high current swing needs to be set up. Therefore, a high collector current $I_C$ and a high collector-emitter voltage $V_{CE}$ are required. However, Kirk-effect and voltage breakdown of the HBTs need to be prevented by a carefully selecting the appropriate bias condition.

In [107,108] Rickelt and Rein consider different driving conditions of SiGe HBTs. Figure 4.3 shows schematically the dependency of the impact ionization on different driving conditions for an HBT for equal collector currents $I_C$ at low collector-emitter voltages $V_{CE}$.

For an impressed base current $I_B > 0$ the maximum collector-emitter voltage is given by $BV_{CEO}$, which is defined for an open base contact ($I_B = 0$). In this case

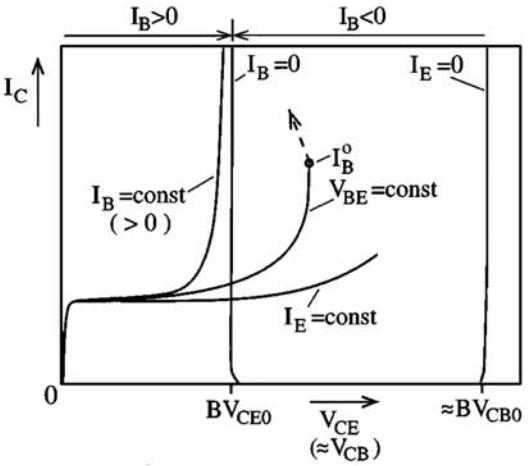


Figure 4.3: Influence of the impact ionization on the output characteristics of bipolar transistors for different driving conditions [107, 108]

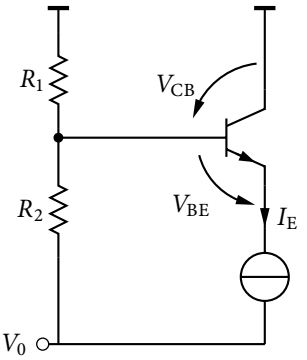


Figure 4.4: Biasing of a SiGe HBT

the transistor shows its lowest breakdown voltage. This breakdown voltage, however, can be exceeded by setting up a constant base-emitter voltage $V_{BE}$ or better a constant emitter current $I_E$. In these cases a negative base current, induced by impact ionization, does not result in a rapid growth of the collector current $I_C$. With an impressed emitter current $I_E$ the highest collector-emitter voltage can be used. Therefore, this type of bias is used in the oscillators presented in this work.

The stabilization of the emitter current is also advantageous for preventing the Kirk-effect in the HBTs. For the realization of the current source, a current mirror circuit is employed. As both suboscillators should be driven with the same currents, one reference path for both suboscillators is used.

Figure 4.4 shows schematically the biasing of one transistor with the impressed emitter current. A resistive divider fixes the voltage at the base terminal. As the emitter voltage is not externally fixed the base voltage and the base-emitter voltage $V_{BE}$ of the transistor will adjust it. The resistive divider in the design of Figure 4.4 sets the collector-base voltage $V_{CB}$ of the device.

By setting the collector terminal to ground, at this terminal a decoupling of the DC and the RF path can be omitted. In the oscillators realized, a tuning voltage on the resistive divider can be applied for adjusting the collector-base voltage $V_{CB}$.

## 4.3 Passive Structures

### 4.3.1 Metallizations

To enable high performance integrated circuit designs, the fabrication process offers additionally several passive structures. First of all the metallization layers are to be mentioned. Four copper layers with thicknesses of 600 nm, 600 nm, 1200 nm and 2400 nm, respectively, can be realized on top of the substrate. The isolations between these layers consists of a 50 nm SiN layer and rest $SiO_2$. The total thicknesses of the dielectrics are 850 nm, 850 nm and 2050 nm. In the fabrication of the oscillator presented in section 5.1.3 the dielectric thickness between metal 3 and metal 4 is reduced from 2050 nm to 1350 nm due to an update in the fabrication process.

In the circuit layout several design rules for the metallization need to be met. Table 4.1 compilates some of these rules. The metal density rules have to be fulfilled in any 100 µm × 100 µm window for metal 1 and metal 2 and in any 400 µm × 400 µm

Table 4.1: Design rules for the cooper metallizations

| | metal 1 | metal 2 | metal 3 | metal 4 |
|---|---|---|---|---|
| thickness in nm | 600 | 600 | 1200 | 2400 |
| minimum width in µm | 0.6 | 0.6 | 1.2 | 2.4 |
| maximum width in µm | 15 | 15 | 15 | 15 |
| minimum density in % | 19.8 | 19.8 | 19.8 | – |
| maximum density in % | 80 | 80 | 80 | – |

window for metal 3. In a microwave circuit design, therefore, fill structures have to be placed carefully into the layout for not influencing the circuit performance and holes in the ground plane need to be introduced.

Between the metallization layers vias are realized for interconnections. For increasing the current carrying ability and for decreasing the series resistance of the vias in practical circuit designs usually arrays of vias are used.

For the connection of the MMIC aluminum pads can be realized on chip. The aluminum structures, however, must not be placed close to active circuit elements and thus this metal layer cannot be used for interconnects or for integrated transmission lines.

### 4.3.2 Integrated Resistors and Capacitors

In addition to the metallizations that can be used also for distributed circuit elements, the fabrication process offers resistors and capacitors that can be considered as concentrated circuit elements up to millimeter-wave frequencies.

For high ohmic resistors two different poly-silicon resistors with sheet resistances of 150 Ω/□ and 1000 Ω/□, can be implanted in the Si substrate. A high precision TaN thin film resistor with 20 Ω/□ can be realized between metal 1 and metal 2 .

A metal-insulator-metal (MIM) capacitor between metal 2 and metal 3 allows to realize high-$Q$ capacitors with an area specific capacitance of 1.4 fF/µm$^2$. For the realization of the capacitors also the design rules for the metals need to be considered.

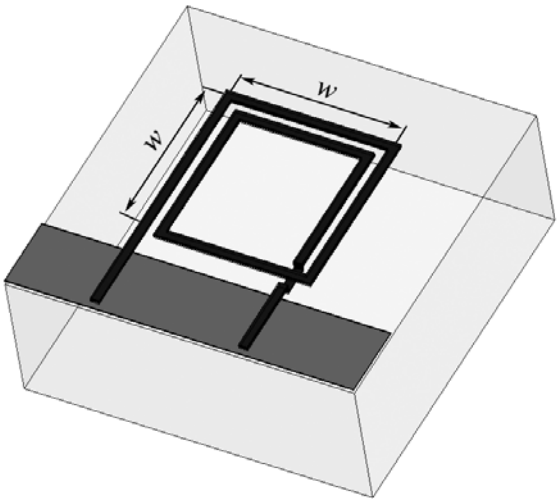


Figure 4.5: Inductor with 1.5 turns and a size of $w \times w$

Therefore, when large capacitors, e. g. for DC voltage stabilization are needed, arrays of capacitors are built.

### 4.3.3 Integrated Spiral Inductors

The realization of integrated inductors is much more challenging as of resistors and capacitors. Conventionally integrated inductors are realized as planar spirals as depicted in Figure 4.5. The electromagnetic field is, however, perpendicular to the circuit plane and thus it penetrates the lossy Si substrate. In the technology used it shows a resistivity of 18.5 Ωcm and the high relative dielectric constant $\epsilon_r = 11.9$.

Already in 1965 experiments with spiral inductors on silicon substrates led to the conclusion that the self-resonance caused by the parasitic capacitance to the substrate limits their high frequency abilities. And the losses due to the eddy currents induced in low resistivity substrates limit the quality factor $Q$ [110].

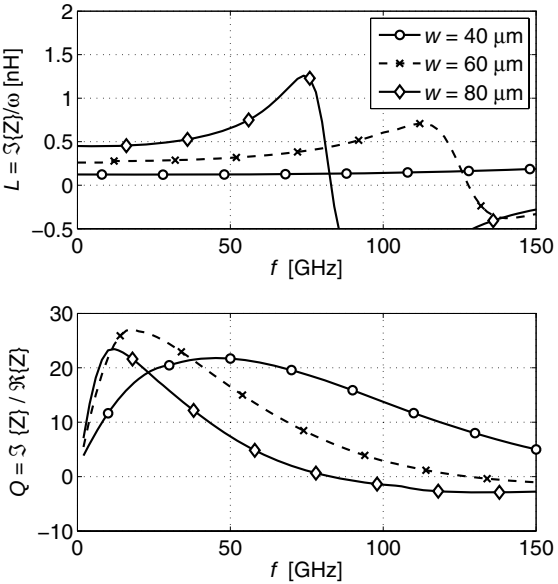


Figure 4.6: Simulated inductance $L$ and $Q$-values of three inductors with 1.5 turns and different sizes $w \times w$

The use of high resistivity substrates is one way to improve the inductors performance. For the process used in this work, this factor, however, is fixed. In [111] the author sums up endeavors of the recent years to improve the performance of integrated inductors.

One common approach for planar inductors is bulk etching. This can be accomplished either by selectively etching out the silicon from the front side [112], or by etching form the back side [113]. Another option is surface micromachining, where the substrate is not etched, but the inductors are realized in a distance above the substrate. The spacing between the underpass and the spiral is in this technology significantly increased, thus reducing the mutual capacitance between these lines [114,115].

Another approach to minimize the magnetic flux in the substrate is, to turn the inductor out of the substrate plane so that the spiral is perpendicular to the substrate.

These types of integrated inductors are named *out-of-plane* or *solenoid* inductors [116, 117].

During this work, however, the production technology used, has not allowed substrate etching or micromachining. Also a shielding of the lossy substrate with a ground metallization is not practical, since the capacitance to ground would be increased considerably and the resonance frequency of the inductor would decrease.

Therefore, conventional planar inductors are designed. For the simulation of the inductors the commercial electromagnetic field solver Ansoft HFSS is used. Realizations with 1 turn, 1.5 turns (Figure 4.5) and 2 turns were investigated. The simulations reveal that the resonance frequency of the inductors with 2 turns is too low for the use in push-push oscillators for automotive radars. The inductor with 1.5 turns, however, provides an inductive behavior in a wide frequency range while being less space consuming than the inductor with one turn.

Figure 4.6 shows simulation results of three inductors with one and a half turns and sizes of $w = 80\,\mu m$, $w = 60\,\mu m$ and $w = 40\,\mu m$. For the spiral the metallization layer 4 is used and the underpass is on layer 3. The metal width and the distance between the turns are both 5 µm. Wider metal strips or narrower gaps in-between result in higher parallel capacitances and thus lower resonant frequencies.

For a push-push oscillator with an output frequency of $2f_0 = 77\,GHz$ the $Q$-factor should be maximum at the internal oscillation frequency $f_0 = 38.5\,GHz$. This is achieved best by the 40 µm × 40 µm inductor. Therefore, this inductor is used in the oscillator design for 77 GHz.

### 4.3.4 Integrated Transmission Lines

The use of integrated transmission lines allows to realize inductive and also capacitive impedance values. At the same time the interconnects of the integrated circuit elements need to be regarded as transmission lines. This way the parasitics of the interconnects are modeled.

In general, either microstrip transmission lines or coplanar lines could be used for the integrated circuit design. When microstrip lines are used, the maximum distance between the line and ground is 5.5 µm and thus the according line width for a 50 Ω-line is only 9.7 µm. This results in a resistance per length at low frequencies of 0.76 Ω/mm. At 38.5 GHz this series resistances increases due to the skin-effect to 2.2 Ω/mm. The dielectric losses of the SiO isolator are low compared to the resistive

losses as $\tan\delta = 10^{-4}$. The attenuation factor of a 50 Ω microstrip line is 1.7 dB/$\lambda$ at 38.5 GHz (with $\lambda = 4.6$ mm). Similar results are shown for grounded coplanar waveguides in [118].

When coplanar lines without ground on metal layer 1 would be used, the line width could be increased while the characteristic impedance remains constant and thus the resistive losses could be reduced. In this case the electromagnetic field would penetrate the lossy Si substrate and thus dielectric losses would increase. The larger structures would be more space consuming and difficult to arrange on the chip. In this work the microstrip technology is preferred over coplanar technology due to the higher flexibility and the lower space requirements on chip.

# Chapter 5

# Design and Verification of Realized Oscillators

Within this work several millimeter wave push-push oscillators are realized [25–30, 46]. In the following, five different oscillators are presented. The oscillators in section 5.1.3 and section 5.2.2 are not published up to now. At first in section 5.1.1 oscillators designed for automotive radar applications are demonstrated. Afterwards, in section 5.2 oscillators with much higher output frequencies are discussed.

## 5.1 Oscillators for Automotive Radar Applications with Output Frequencies below 100 GHz

For automotive radar applications signal sources at frequencies around 77 GHz are required. Depending on the distance of the objects to be detected two independent sensors are under development: The long range radar at 76.5 GHz and the short range radar at 79 GHz. For the long range radar the bandwidth is 200 MHz, while for the short range radar, where a higher resolution is necessary, the bandwidth is 4 GHz. An oscillator that can be tuned from 76 GHz up to 81 GHz could be used for both sensors. The specifications concerning output power and phase noise are still a not fixed.

Since the fabrication process has been still under development during this work updates of the process have been introduced by the manufacturer. Therefore, the oscillation frequencies in the oscillators described in section 5.1.1 and in section 5.1.2 differ from the initially intended frequency.

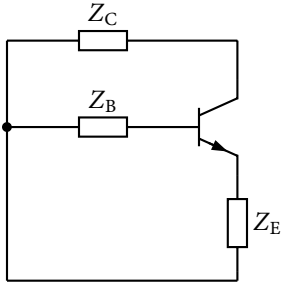


Figure 5.1: Load impedances connected to the transistor terminals for considering the small signal oscillation condition

### 5.1.1 Spiral Inductor based 70 GHz Push-Push Oscillator

The circuit design of the 70 GHz push-push oscillator [26] presented here is based on the active devices and the design considerations described in chapter 4. This section starts with the small signal circuit design of one suboscillator, describes the nonlinear circuit analysis of the complete push-push oscillator and discusses the circuit layout. At the end of the section, the measurement results on this circuit are presented.

#### Circuit design

For the design of the suboscillator, first a set of impedances to be connected to the active device for fulfilling the small signal oscillation condition needs to be found. Therefore, the transistor is linearized around its bias point and arbitrary impedances are connected as depicted in Figure 5.1. For a high $Q$-factor of the oscillator circuit, the circuit elements connected should show low losses. In this scheme, no load resistance appears because at the frequency of oscillation and for the intended mode of operation, the suboscillator is loaded only by a virtual ground.

A ground can be connected to any node of the circuit. Its behavior depends only on the impedances that appear between the transistor terminals. This circuit could be considered either as common collector, common base or common emitter configuration. Therefore, the designed circuits are not regarded as any of these basic transistor configurations. From the schematic in Figure 5.1 it can be seen that one of

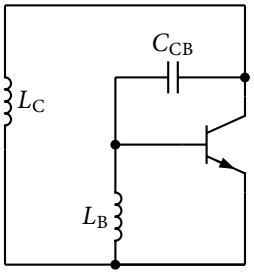


Figure 5.2: Hartley oscillator configuration

the impedances can be shorted without loss of a degree of freedom, as it is in series to the parallel connection of the other two. The degree of freedom in the circuit design here is only two.

The most common topologies for integrated oscillators are the Colpitts and the Hartley oscillators, which differ in the general type of feedback that is used. At millimeter wave frequencies the parasitic capacitance of the transistor between collector and base $C_{CB}$ is large enough to achieve the feedback required in a Hartley oscillator. For this reason, the Hartley configuration is generally preferred in this frequency band. By connecting the inductive impedances between the base terminal and the emitter terminal and between the collector terminal and the emitter terminal, $L_B$ and $L_C$, respectively, the Hartley configuration is completed (Figure 5.2).

As discussed in section 4.2.2 the collector terminal is DC grounded. The inductance $L_C$ combines the DC connection to ground and the inductive behavior at RF. Thus, a network separating the RF signal from the DC path is not necessary at this terminal. The base network and the emitter network will be coupled with the second suboscillator. Thus, virtual grounds for the fundamental frequency appear at the connection points as illustrated in Figure 5.3. As the grounds of the two suboscillators are connected, at the collector network also a virtual ground exists, which is identical with the ground of the complete circuit.

At the emitter terminal a series combination of the capacitor $C_E$ and the inductor $L_E$ is connected. This does not comply with the standard Hartley oscillator configuration. This deviation, however, allows by choosing appropriate values for these elements, an optimization of the $Q$-factor of the suboscillator.

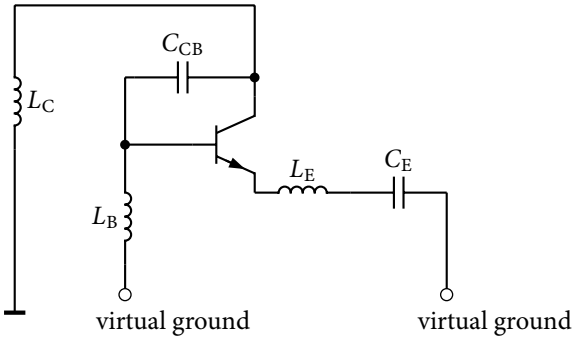


Figure 5.3: Equivalent circuit for the suboscillator at the fundamental frequency $f_0$

The output of the push-push oscillator can be connected at any point of the symmetry line of the circuit. Conventionally the output is connected at the collector terminal. Since this terminal is DC grounded, here the maximum amplitude is limited. At the emitter terminal, however, the voltage is not fixed, as the current source is connected and thus higher voltage amplitudes can be reached. This is confirmed by large signal analyses that reveal best results for the common output connected at the emitter networks. Thus, this network is used for the oscillator output port and the load impedance $R_L$ is connected here.

For analyzing the small signal oscillation condition the odd mode equivalent circuit of the push-push oscillator as shown in Figure 3.3i) is considered and thus the load impedance is set to zero, i. e. $R_L = 0$. The oscillation condition is fulfilled with the parameters: $L_B = 195\,\text{pH}$, $L_C = 40\,\text{pH}$, $L_B = 31\,\text{pH}$ and $C_B = 250\,\text{fF}$. The inductors $L_C$ and $L_E$ for the collector and the emitter network, respectively, are realized by integrated transmission lines. For the larger inductor in the base network $L_B$, however, the spiral inductor described in section 4.3.3 with a size of $40\,\mu\text{m} \times 40\,\mu\text{m}$ is used in order to achieve a high inductance per chip area. To increase the inductance of the spiral ($L_{Spiral} = 122\,\text{pH}$) to the desired value a transmission line is connected in series. A narrow line width of $5\,\mu\text{m}$, exhibiting a high characteristic impedance and thus a high inductance per length, is chosen for this purpose.

Simulation results of the input impedance $Z_S$ of the suboscillator are plotted in

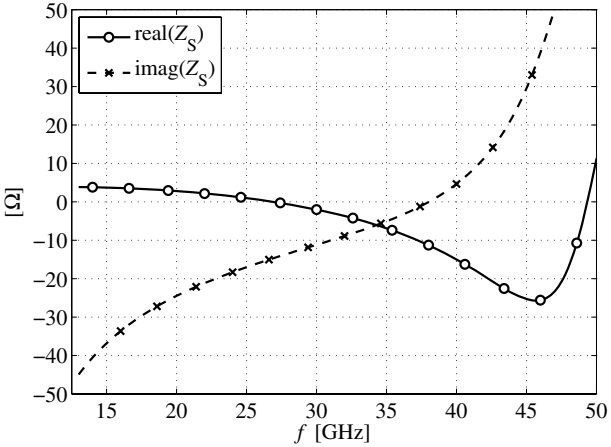


Figure 5.4: Simulated input impedance $Z_S$ of the suboscillator

Figure 5.4. At the desired frequency of oscillation and within an adjacent broadband frequency range the real part $\Re\{Z_S\}$ is negative. This allows tuning of the oscillator within a certain frequency range. Due to $\Re\{Z_S\} > -2R_L$ (with $R_L = 50\,\Omega$) at any frequency, even mode oscillations are not possible. Thus, the oscillation condition for odd mode operation of the combined circuit as given in (3.7) is fulfilled. The actual frequency of oscillation is given by the frequency, where the imaginary part of the input impedance $Z_S$ is zero. This is achieved at the desired frequency $f_0 = 37.5\,\text{GHz}$.

Two suboscillators are now combined to form the whole push-push oscillator, which is schematically drawn in Figure 5.5. The collector terminal is grounded via a transmission line resonator. The inductance $L_E$ is formed by a 110 µm transmission line. For the RF-path the end of this line is connected with the capacitor $C_E$ to the common output port. For the bias decoupling, here, a combination of a transmission line and a spiral inductor is used. At the inductor, a constant emitter bias current is impressed by the current mirror. As the capacitance $C_{CE}$ is a parasitic capacitance of the transistor, it is not explicitly drawn in the schematic.

At the base terminals of the transistors, the series combinations of a transmis-

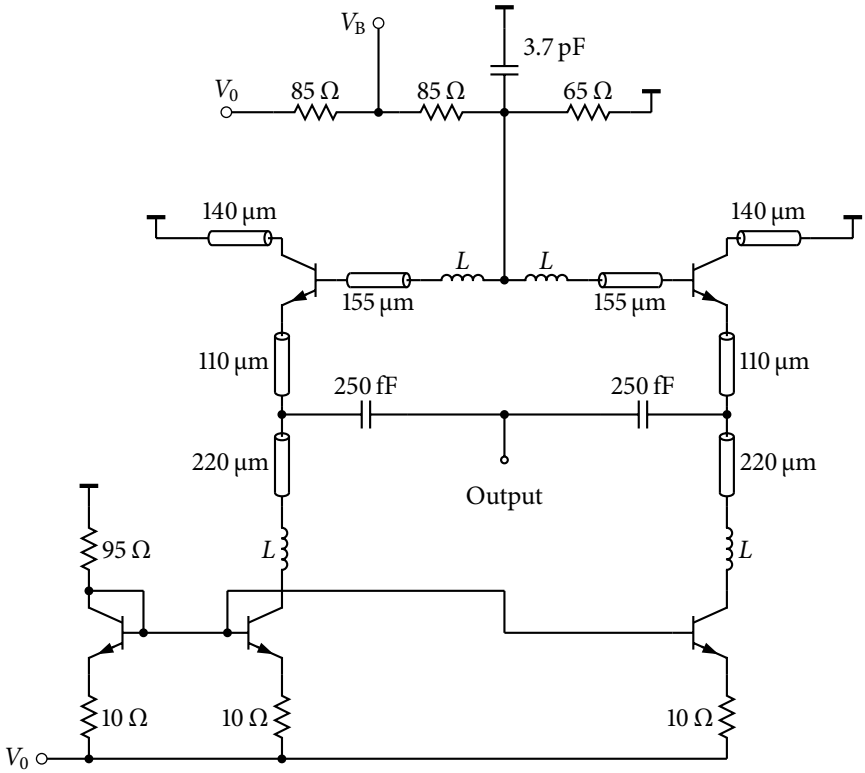


Figure 5.5: Circuit diagram of the 70 GHz push-push oscillator

sion line and the spiral inductor are connected. The DC supply at the base terminals is accomplished by a resistive divider connected at the virtual ground at the symmetry line of the circuit. Low resistances are used here to provide a low resistance connected to the base terminal in order to prevent the Kirk-effect in the transistor. The capacitance $C_B$ provides a short at the second harmonic frequency $2f_0$ and thus prevents a damping of the oscillation at this frequency. Additionally it stabilizes the bias voltage and prevents oscillations at low frequencies. For this purpose a large capacitance $C_B = 3.7\,\text{pF}$ is used.

The harmonic balance simulation of the circuit in Figure 5.5 determines an oscillation frequency $f_0 = 38.5\,\text{GHz}$ at a supply voltage $V_0 = -3\,\text{V}$. The simulated output power is 3.2 dBm. Figure 5.6 shows the simulated time domain signals of the collector currents $I_C$ and the collector to emitter voltages $V_{CE}$. It can be seen that the collector-emitter breakdown voltage $BV_{CEO}$ and also the optimum collector current for the maximum frequency of oscillation $I_{C,opt}$ (see section 4.2) are both exceeded within short time intervals. The collector current $I_C$ reaches a maximum of 42 mA although the DC collector current through one transistor is only 20 mA. Due to the type of bias used in this circuit the transistor can recover from the Kirk-effect and the increased impact ionization.

The layout of the push-push oscillator is designed with a maximum in symmetry. A chip photograph of the fabricated circuit is depicted in Figure 5.7. The distance between the two transistors is given by the length of the transmission lines in the emitter networks. The lines in the base and in the collector networks are bent for saving chip area. For connecting the current sources at the emitter networks, a crossing of either the line to the output or of the base network is necessary. In this design, the base network is crossed.

To stabilize the supply voltage, large MIM-capacitors are integrated. The input and output ports are realized by ground-signal-ground (GSG) pad configurations that allow a biasing of the circuit by RF probes and an on-wafer characterization of the oscillator circuit. In order to enable tuning of the collector to base voltage $V_{CB}$ of the transistors an additional set of pads that is connected to the resistive divider, is realized. The metal grid that can be seen in the photograph is used in order to provide a ground plane on the layer metal 1. Holes are introduced in the ground plane for fulfilling the design rules as described in section 4.3.1.

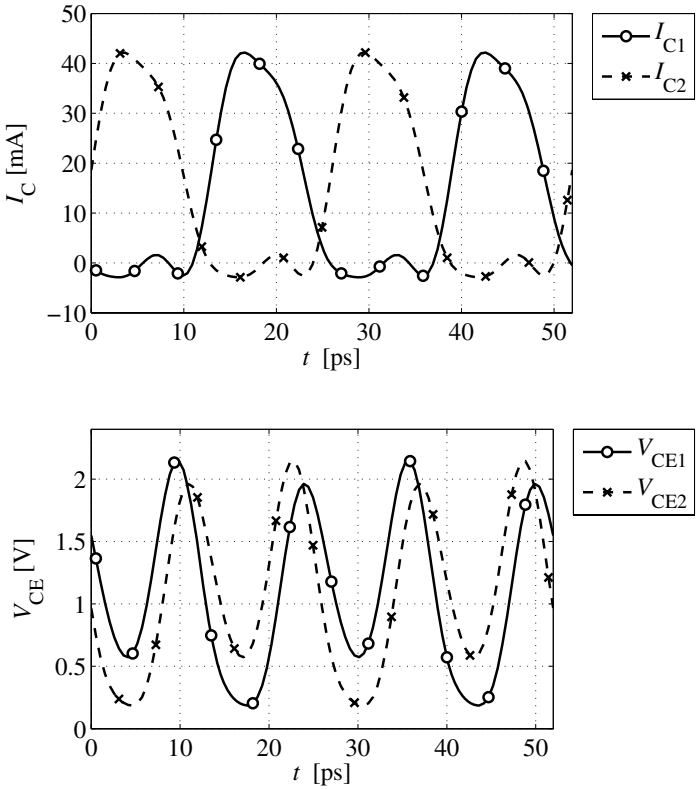


Figure 5.6: Simulated time domain signals of the collector currents $I_C$ and the collector emitter voltages $V_{CE}$ in the two suboscillators

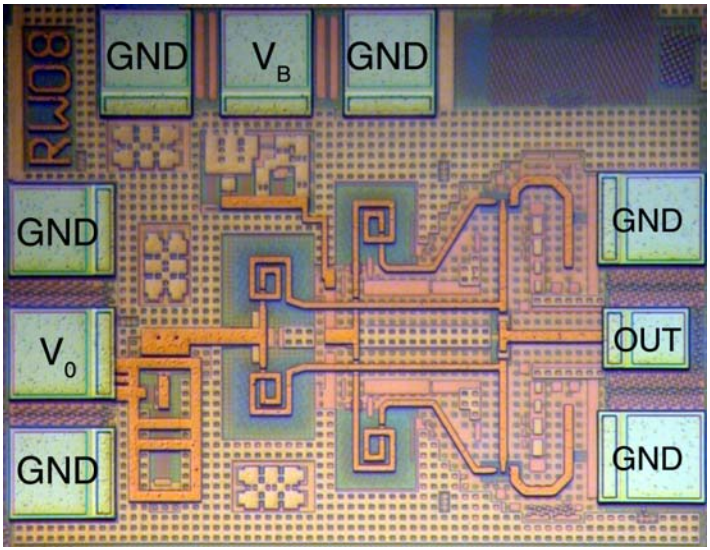


Figure 5.7: Chip photograph of the realized 70 GHz push-push oscillator (625 µm × 485 µm)

**Experimental Results**

The output signal of the push-push oscillator is measured on wafer by an HP 71000 spectrum analyzer using appropriate harmonic mixers. The measured power levels are corrected for the conversation loss of the mixers. Losses of the RF-probe and the measurement cables are taken into account with 1 dB. The DC supply voltage $V_0$ is connected by a GSG probe.

Figure 5.8 demonstrates the performance of the oscillator as a function of the supply voltage $V_0$. At $V_0 = -2$ V the output power reaches its maximum of 1.6 dBm. The measured spectrum of the oscillator output signal for this voltage is depicted in Figure 5.9. In this case the total bias current is −48 mA and the power consumption of the whole device is therefore 96 mW. This circuit has not been designed for a minimum power consumption; the efficiency is only 1.5 %.

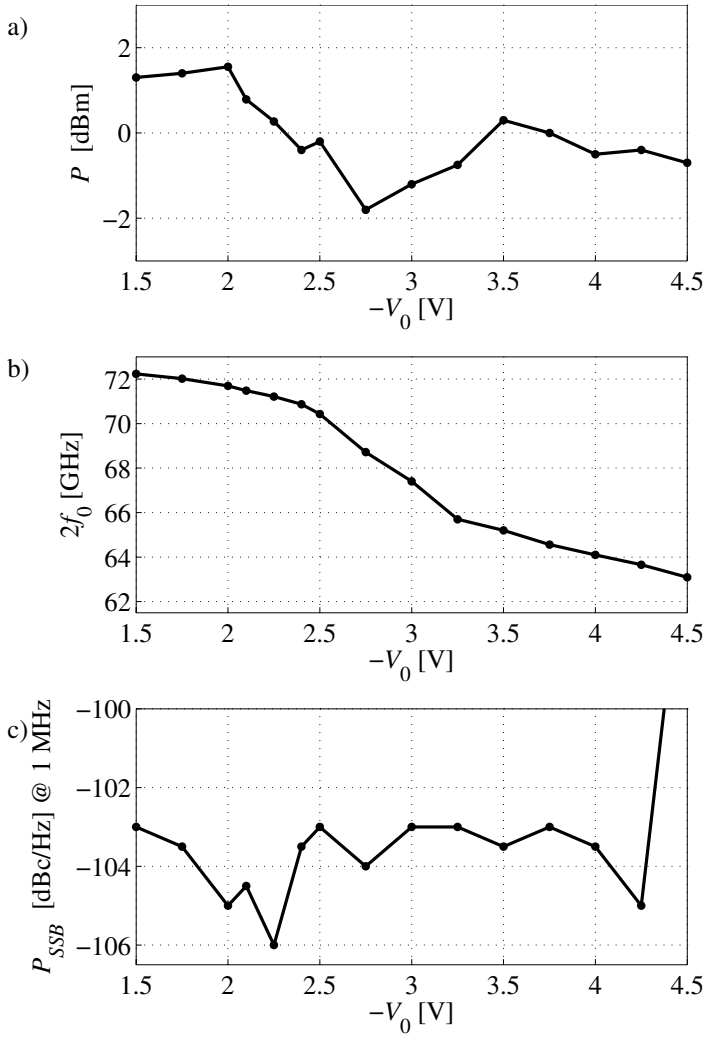


Figure 5.8: Dependency of a) the output power $P$, b) the output frequency $2f_0$ and c) the single side band phase noise $P_{\mathrm{SSB}}$ at 1 MHz offset from the carrier on the bias voltage $V_0$

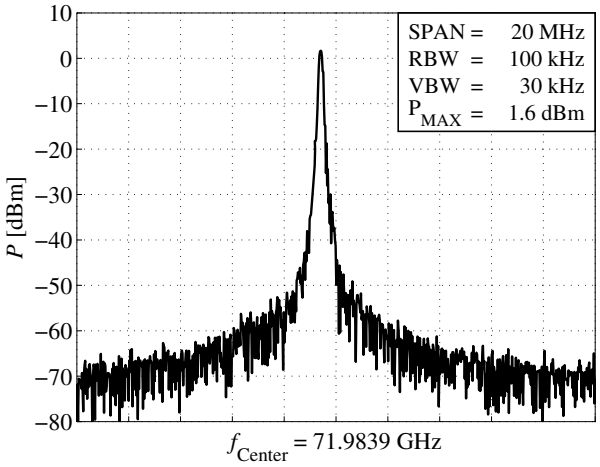


Figure 5.9: Measured spectrum at the second harmonic frequency of the oscillator signal for $-V_0 = 2.0\,\mathrm{V}$

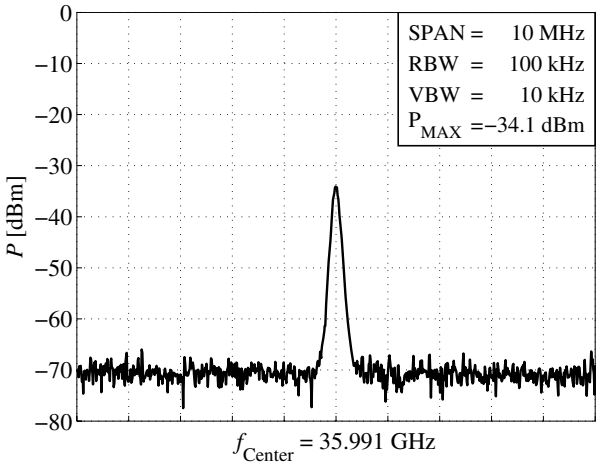


Figure 5.10: Measured spectrum at the fundamental frequency of the oscillator signal for $-V_0 = 2.0\,\mathrm{V}$

Varying the bias voltage between −1.5 V and −4.25 V the oscillation frequency changes form 72.23 GHz to 63.66 GHz, respectively. In this frequency range the single side band phase noise level is less than −103 dBc/Hz at an offset frequency of 1 MHz. At a supply voltage of $V_0 = -2.25$ V the phase noise level reaches a minimum of −106 dBc/Hz.

A measured spectrum of the fundamental frequency $f_0$ is shown in Figure 5.10. The low power level of this signal with −34 dBm indicates a high symmetry of the fabricated push-push oscillator and a proper odd mode operation. When an additional GSG probe is connected at the terminal $V_B$, the oscillation frequency gets unstable. Therefore, a separate tuning of this voltage is not performed on this circuit. Measurements of the temperature stability of this circuit are not available.

### 5.1.2 Push-Push VCO for 82 GHz

The oscillator described in this section is based on the design in section 5.1.1. For the control of the oscillation frequency, here a varactor is integrated and the spiral inductors are replaced by transmission lines [27].

#### Circuit Design

The fabrication process used in this work, does not provide integrated varactor diodes at the time when the circuits are realized. As a compromise, the collector-base junction of a transistor is employed as a voltage controllable capacitance. This capacitance, however, can be varied only in a small range and shows higher losses than varactor diodes that are optimized for this purpose. This results in a limited tuning bandwidth of the oscillator, and special care needs to be taken in order not to reduce the oscillator $Q$-factor significantly when the varactor is introduced. Figure 5.11 shows the tunability of the varactor and the corresponding $Q$-factor. At 40 GHz the relative tuning range of the varactor is 68 % and the $Q$-factor varies between 6 and 7.

The small signal analysis of one suboscillator indicates that the highest tuning sensitivity is reached, when the varactor element is connected in parallel to the base inductance $L_B$. A large signal analysis confirms this fact and thus the varactors are placed as close as possible to the base terminals of the transistors $Q_1$ and $Q_2$ as drawn in Figure 5.12. The 60 µm long microstrip lines that connect the varactors with the virtual ground increase the tuning range and improve the $Q$-factor of the oscillator. The voltage $V_{VC}$ denotes the voltage at the collector-base junction of the varactor. This voltage can be adjusted by the external tuning voltage $V_T$. By the 55 µm long transmission line connecting the varactor network with the large capacitor that provides a RF short, the impedance at the second harmonic frequency $2f_0$ is optimized. The nonlinear simulation of the VCO shows a tuning range of 1.2 GHz.

In this circuit, the combination of spiral inductors with transmission lines at the base terminals that is used in section 5.1.1 is replaced by a 350 µm long microstrip line. At the intended oscillation frequency $f_0 = 38.5$ GHz the corresponding equivalent inductance of the network connected at the base terminal is 226 pH. The collector terminals are again grounded via transmission line resonators and at the emitter terminals 190 µm long transmission lines are connected.

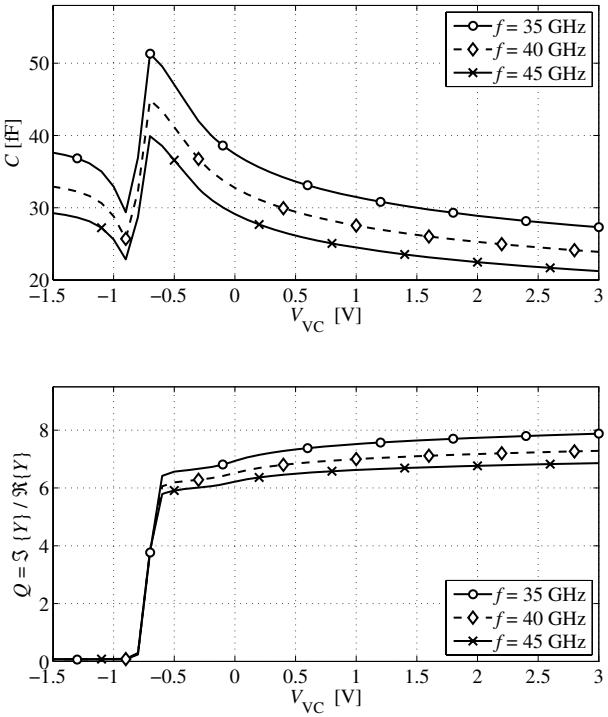


Figure 5.11: Simulated tuning characteristics of the collector-base capacitance that is used as a varactor

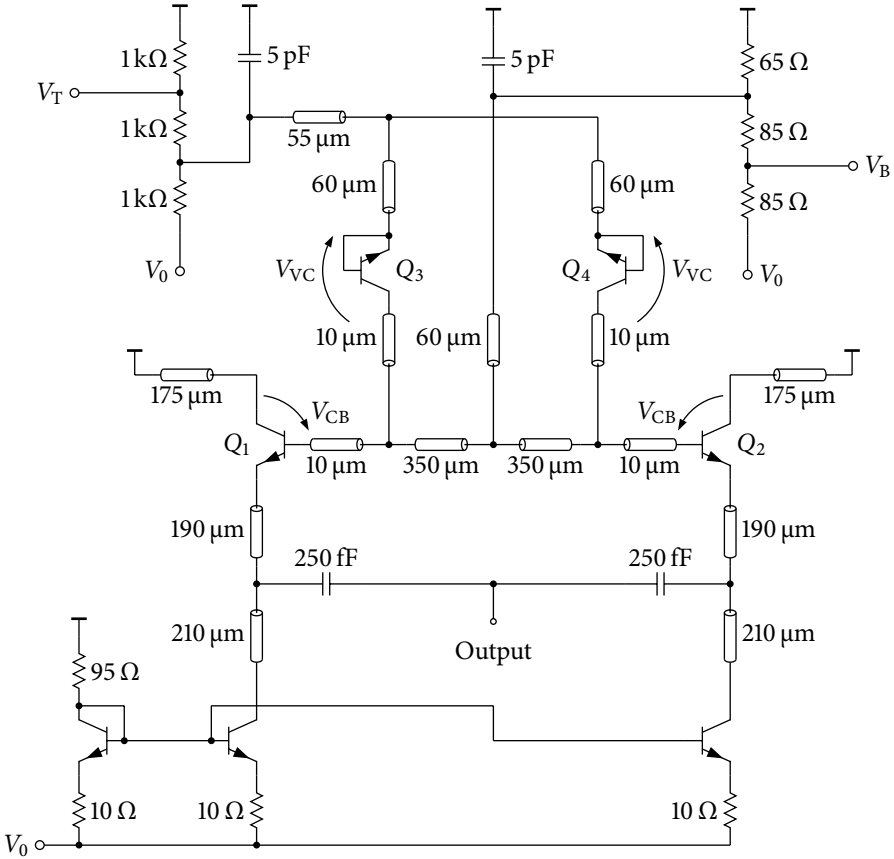


Figure 5.12: Circuit diagram of the 82 GHz push-push VCO

Here, via the capacitors the RF signal passes to the common output port. For the bias decoupling 210 µm long microstrip lines with a characteristic impedance $Z = 68\,\Omega$ providing an increased inductance per length, are used. At these transmission lines, the current mirror circuit impresses constant emitter bias currents. The DC supply voltage at the base terminal is accomplished by a resistive divider. By varying the voltage $V_B$ the collector to base voltage $V_{CB}$ is be tuned.

A chip photograph of the fabricated circuit is depicted in Figure 5.13. The DC voltages can be applied by the GSG pad configurations. For the connection of the current source to the emitter network in this design the output line of the push-push oscillator is underpassed. This avoids line crossings in the core oscillator as in the design shown in section 5.1.1. The current mirror circuit is located close to the output pads.

**Experimental Results**

The output signal of this oscillator is measured on-chip by the same set up as described in section 5.1.1. The measured power levels are again corrected for the conversation loss of the mixers. For this circuit additionally a $W$-band power meter is used to verify the output power level. Losses of the RF-probe and the measurement cables are taken into account with 1 dB. To verify the measured single side band phase noise level this circuit is also analyzed by delay line method with the phase noise measurement system PN9000 from Aeroflex.

For the DC voltage supply the chip is mounted on a FR4 substrate. By a combination of electrolyte and ceramic capacitors, the supply voltages and the tuning voltage are stabilized. The chip is connected to the substrate by wire bonding.

Figure 5.14 demonstrates the performance of the oscillator as a function of the varactor voltage $V_{VC}$ that is adjusted by the tuning voltage $V_T$. The bias voltage $V_0$ is set to $-3.0$ V and the base tuning voltage $V_B$ to $-4.0$ V. For this bias point the collector to base voltages of the transistors $Q_1$ and $Q_2$ are calculated by $V_{CB} = 1.7$ V and the collector to emitter voltage is 2.6 V. This means that the breakdown voltage $BV_{CEO}$ is exceeded by far. The DC-emitter current in each of these devices is 18 mA.

For a varactor voltage $V_{VC} = 2.05$ V the output power reaches its maximum of 3.9 dBm. The measured single side band phase noise level goes to its minimum of $-108$ dBc/Hz at an offset frequency of 1 MHz at a varactor voltage $V_{VC} = 1.80$ V. The measured spectrum of the oscillator output signal for this varactor voltage is depicted

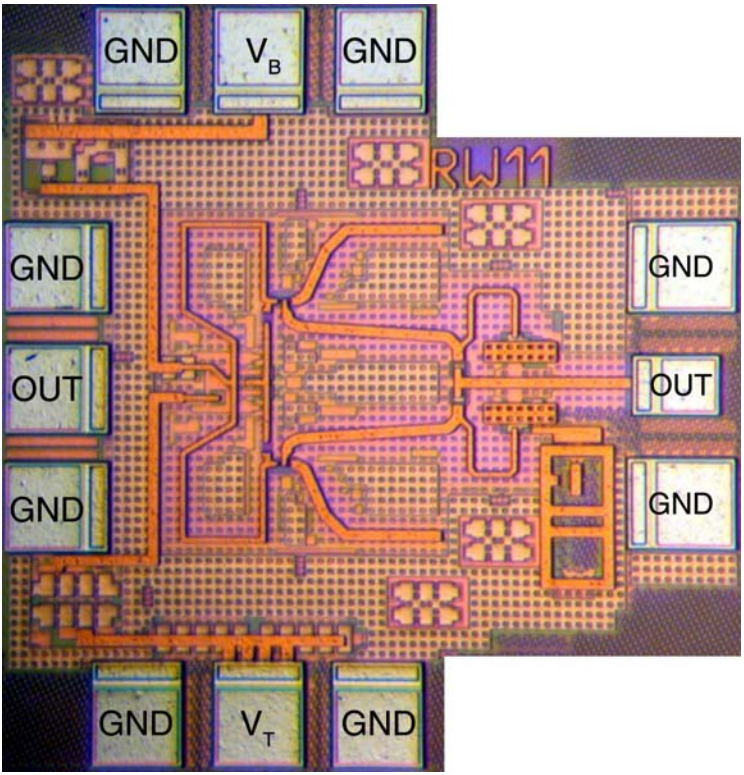


Figure 5.13: Chip photograph of the 82 GHz push-push VCO (700 µm × 700 µm)

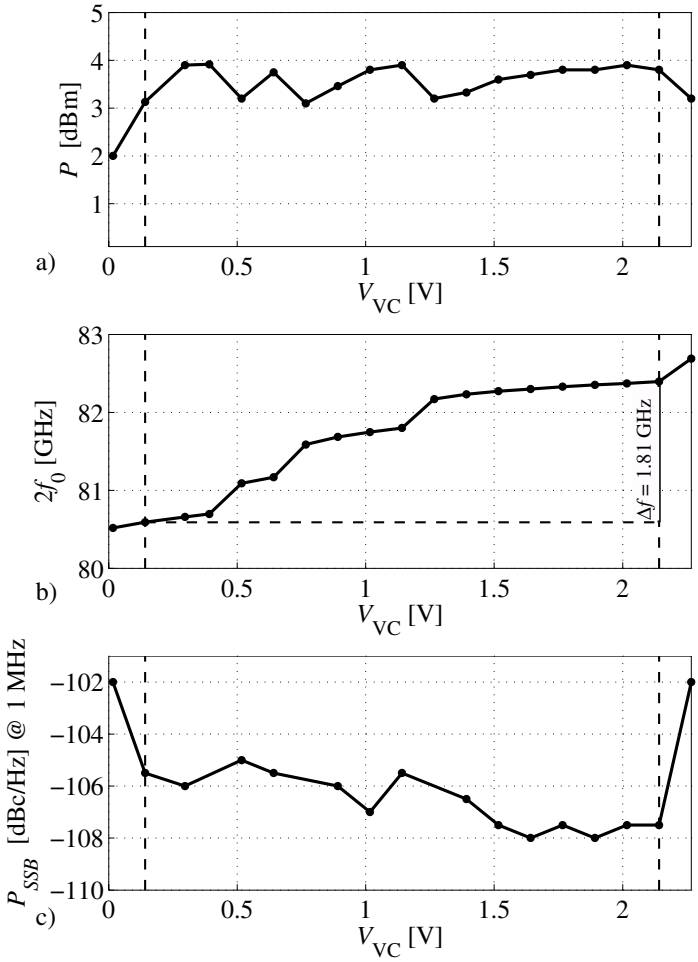


Figure 5.14: Dependency of a) the output power $P$, b) the output frequency $2f_0$ and c) the single side band phase noise $P_{\mathrm{SSB}}$ at 1 MHz offset from the carrier on the varactor voltage $V_{\mathrm{VC}}$ ($V_0 = -3.0\,\mathrm{V}$, $V_{\mathrm{B}} = -4.0\,\mathrm{V}$)

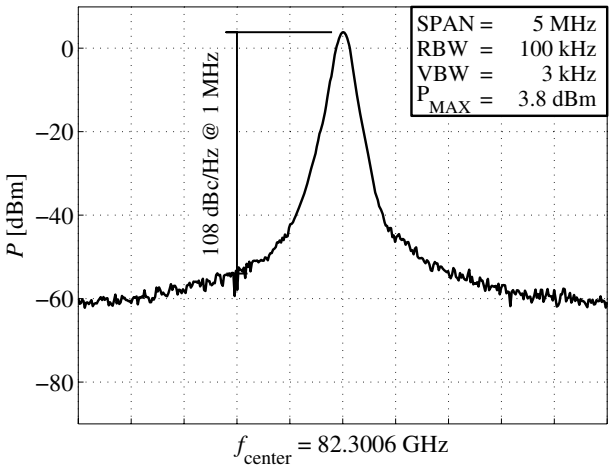


Figure 5.15: Measured spectrum at the second harmonic frequency of the oscillator signal for $V_0 = -3.0\,\mathrm{V}$, $V_B = -4.0\,\mathrm{V}$ and $V_T = -3.75\,\mathrm{V}$ ($V_{VC} = 1.80\,\mathrm{V}$)

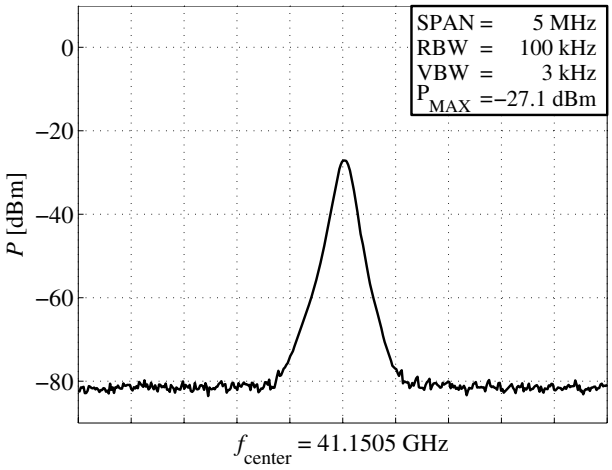


Figure 5.16: Measured spectrum at the fundamental frequency of the oscillator signal for $V_0 = -3.0\,\mathrm{V}$, $V_B = -4.0\,\mathrm{V}$ and $V_T = -3.75\,\mathrm{V}$ ($V_{VC} = 1.80\,\mathrm{V}$)

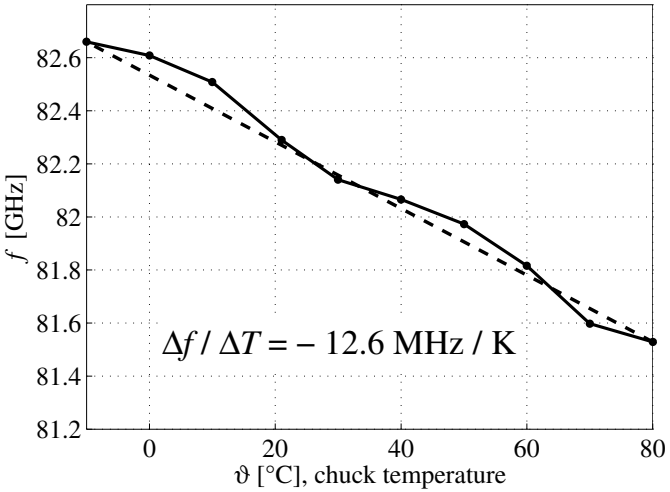


Figure 5.17: Measured temperature sensitivity of the output frequency $2f_0$ for $V_0 = -3.0\,\mathrm{V}$, $V_\mathrm{B} = -4.0\,\mathrm{V}$ and $V_\mathrm{T} = -3.75\,\mathrm{V}$ ($V_\mathrm{VC} = 1.80\,\mathrm{V}$)

in Figure 5.15. In this case the power consumption of the whole device is 280 mW, which corresponds with an efficiency of $\eta = 0.88\,\%$. This circuit, however, has not been optimized with respect to its efficiency.

Varying the varactor voltage between 0.1 V and 2.1 V the output frequency changes form 80.6 GHz to 82.4 GHz, respectively. The relative tuning bandwidth thus is 2.2 %. In this frequency range the oscillators output power is $3.5 \pm 0.4\,\mathrm{dBm}$ and the measured single side band phase noise level is less than $-105\,\mathrm{dBc/Hz}$ at an offset frequency of 1 MHz.

The measured spectrum of the fundamental frequency $f_0$ is shown in Figure 5.16. The low power level of this signal with $-27.1\,\mathrm{dBm}$ indicates a high symmetry of the fabricated push-push oscillator and a proper odd mode operation. In the whole tuning range of the VCO the measured fundamental frequency output power is $-26.5\,\mathrm{dBm}$.

For measuring the temperature sensitivity of the oscillator the chuck temperature is modified. As can be seen in Figure 5.17 the temperature sensitivity of the VCO

is −12.6 MHz/K. We propose that this low temperature sensitivity is a result of the lower temperature dependency of the transistors at the halved oscillation frequency compared to a fundamental frequency oscillator.

### 5.1.3 Low Power Consumption Push-Push VCO for 77 GHz

This oscillator is a derivative of the oscillator in the previous chapter and has not been published up to now. The center frequency of the VCO tuning range is set to 77 GHz, the tuning range is enlarged and the power consumption of the circuit is reduced.

#### Circuit Design

The circuit diagram of this VCO is drawn in Figure 5.18. The resistors in the voltage dividers for the varactor voltage and the collector to base voltage are significantly increased compared to the previous design in order to reduce the power consumption of the circuit. Large capacitors in parallel to these dividers obtain RF shorts for the frequency of oscillation at these points.

At the terminal $V_T$ a series resistance with 10 Ω is connected for damping possible oscillations on the external power supply network. At the terminal $V_B$ a series resistance with 5 Ω is used for this purpose. The emitter bias currents are impressed by the current mirror using four branches for the current source, the current in the reference path is only one quarter of sum of the emitter currents in $Q_1$ and $Q_2$. Thus, the power dissipation in the reference path is reduced.

The layout of the fabricated circuit is depicted in Figure 5.19. For a maximum symmetry of the circuit the current mirror is realized twice, while only one is connected. The pads for the DC voltage supply are in a SGSGS configuration that allows either connection with special DC probes or with bond wires.

#### Experimental Results

The output signal is measured on-chip by an HP 71000 spectrum analyzer using appropriate harmonic mixer. The measured power levels are corrected for the conversation loss of the mixers. A *W*-band power meter is used to verify the output power level. Losses of the RF-probe and the measurement cables are taken into account with 1 dB. For the DC voltage supply the chip is mounted on a FR4 substrate. The bias voltages are stabilized by a combination of electrolyte and ceramic capacitors. Wire bonding is used to connect the chip with the substrate.

The characteristics of the VCO are shown in Figure 5.20 as a function of the varactor voltage $V_{VC}$ that is adjusted by the external tuning voltage $V_T$. The bias voltage

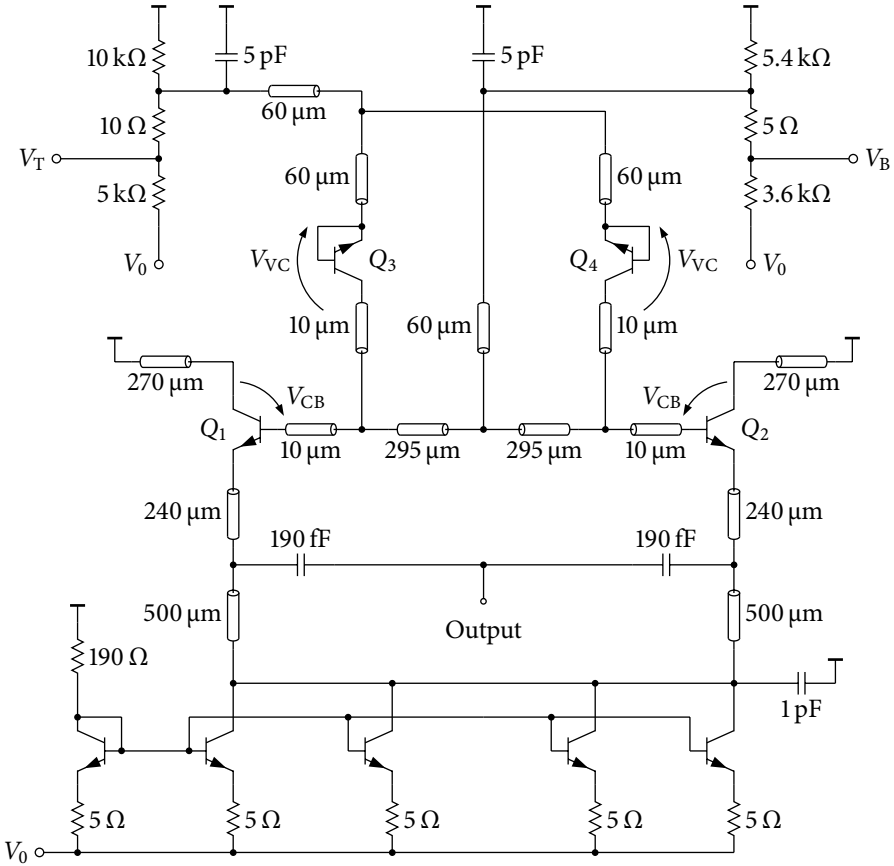


Figure 5.18: Circuit diagram of the 77 GHz push-push oscillator

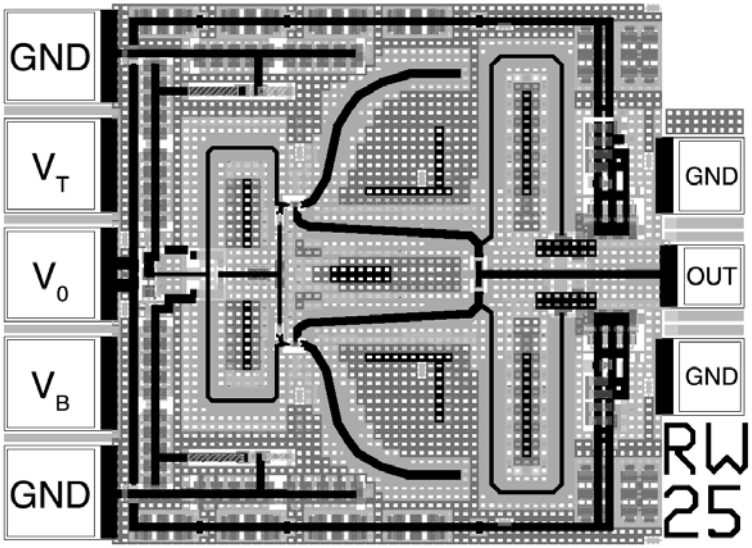


Figure 5.19: Layout of the 77 GHz push-push oscillator (800 µm × 620 µm)

$V_0$ is set to −3.0 V and the base tuning voltage $V_B$ to −2.0 V. Thus, the collector to base voltages of the transistors $Q_1$ and $Q_2$ are $V_{CB}$ = 2.0 V and the emitter currents in each of these devices are 20 mA.

The oscillator output frequency can be tuned from 76.1 GHz to 81.1 GHz. The relative tuning bandwidth is therefore 6.4 %. In this frequency range the output power is 4.0 ± 0.4 dBm. The measured single sideband phase noise level at 1 MHz offset frequency is less than −105 dBc/Hz. The measured spectrum of the oscillator output signal for this varactor voltage is depicted in Figure 5.21.

The measured power of the fundamental frequency signal at $f_0$ is below −34 dBm in the whole tuning range. Figure 5.22 shows the measured spectrum of the fundamental frequency signal for $V_T$ = −2.0 V. For $V_T$ < −2.25 V the fundamental frequency signal power is measured below −47 dBm. For measuring the temperature sensitivity of the oscillator the chuck temperature is modified. The temperature sensitivity of the VCO is −19.5 MHz/K.

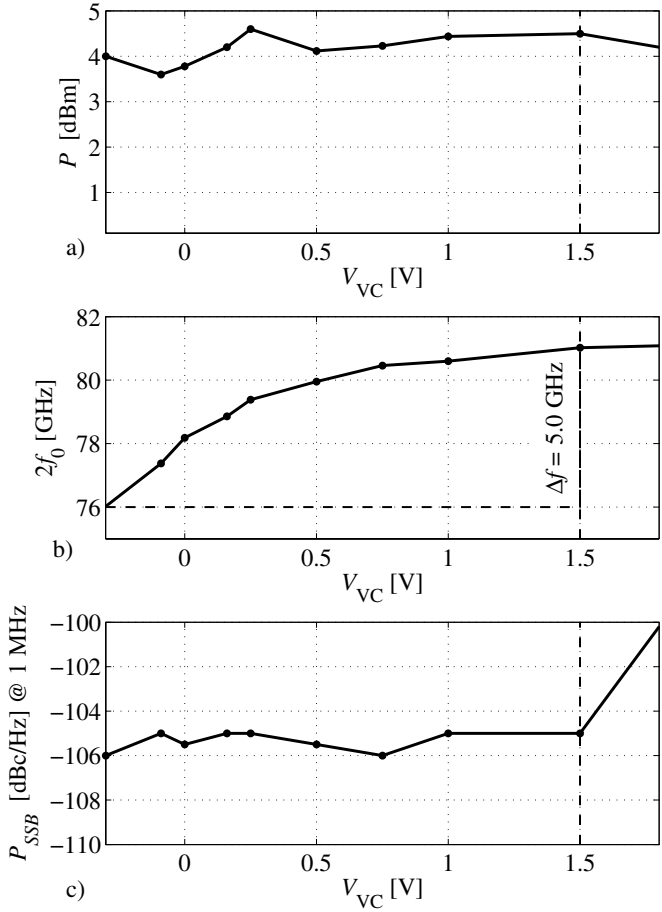


Figure 5.20: Measured a) output power $P$, b) output frequency $2f_0$ and c) single side band phase noise $P_{\mathrm{SSB}}$ at 1 MHz offset from the carrier on the varactor voltage $V_{\mathrm{VC}}$ ($V_0 = -3.0\,\mathrm{V}$, $V_{\mathrm{B}} = -2.0\,\mathrm{V}$)

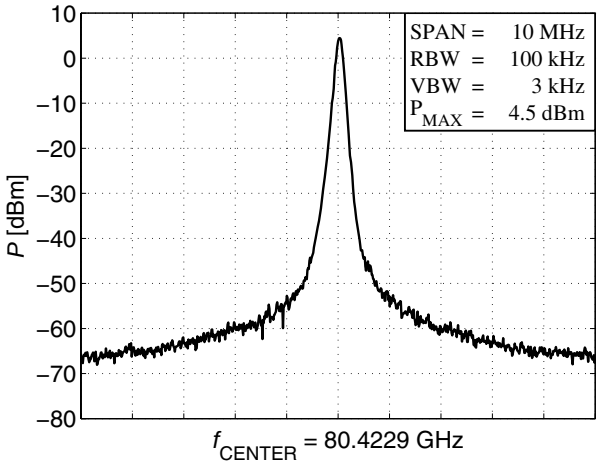


Figure 5.21: Measured spectrum at the second harmonic frequency of the oscillator signal for $V_0 = -3.0\,\mathrm{V}$, $V_B = -2.0\,\mathrm{V}$ and $V_T = -2.75\,\mathrm{V}$ ($V_{VC} = 0.75\,\mathrm{V}$)

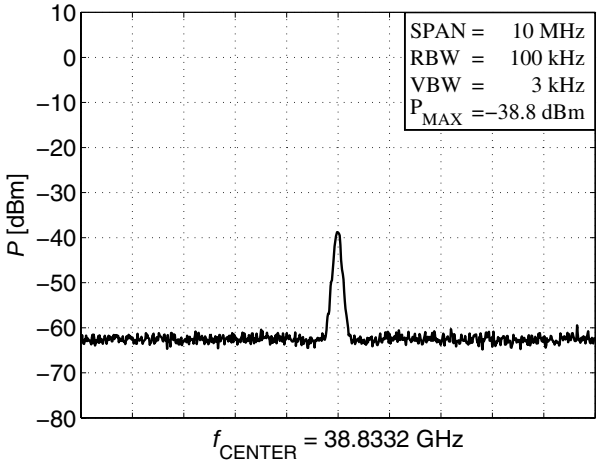


Figure 5.22: Measured spectrum at the fundamental frequency of the oscillator signal for $V_0 = -3.0\,\mathrm{V}$, $V_B = -2\,\mathrm{V}$ and $V_T = -2.0\,\mathrm{V}$ ($V_{VC} = 0.0\,\mathrm{V}$)

Table 5.1: DC to RF efficiency $\eta$ of a similar push-push VCO [29] versus supply voltages ($-V_T = 4\,V$)

| | | | | |
|---|---|---|---|---|
| $-V_0$ | 1.8 V | 2.4 V | 3.0 V | 3.6 V |
| $-V_B$ | 0.8 V | 1.4 V | 2.0 V | 2.2 V |
| $2f_0$ | 76.16 GHz | 76.21 GHz | 76.12 GHz | 75.18 GHz |
| $P_{RF}$ | 1.5 dBm | 3.8 dBm | 3.9 dBm | 1.0 dBm |
| $P_{SSB}$ @ 1 MHz | −107 dBc | −109 dBc | −110 dBc | −108 dBc |
| $\eta = P_{RF}/P_{DC}$ | 3.5 % | 2.7 % | 1.6 % | 0.52 % |

The power consumption of the whole circuit at the bias point $V_0 = -3.0\,V$ and $V_B = -2.0\,V$ is 138 mW. Thus, the efficiency of RF signal generation is 1.8 %. On a similar device that shows a 5 GHz lower output frequency [29], the efficiency is investigated as a function of the bias voltages. By reducing the supply voltage $V_0$ and the base tuning voltage $V_B$ simultaneously, the output power $P$ of this oscillator decreases but the DC to RF efficiency $\eta$ increases. As given in Table 5.1 an efficiency $\eta = 3.5\,\%$ is achieved with $V_0 = -1.8\,V$. Similar behavior is also expected for the 77 GHz oscillator presented here.

## 5.2 Oscillators for Frequencies above 100 GHz

In this chapter the design and the experimental verification of integrated oscillators with output frequencies far above 100 GHz are described. The main intension here is to demonstrate the feasibility of integrated signal sources at these frequencies. As the used transistor model parameters are measured at much lower frequencies, uncertainties of the used model are expected at the frequencies of interest. Therefore, in order to keep the circuit simple, varactors are not used here. The oscillation frequency of these oscillators can be tuned by varying the collector to base voltages $V_{CB}$ of the transistors and thus controlling the feedback capacitance $C_{CB}$ that is a function of $V_{CB}$.

### 5.2.1 Push-Push Oscillator for 190 GHz

The oscillator presented in this section [46] is originally designed for an output frequency of 200 GHz. The measurements, however, have proven a 5 % lower frequency of oscillation. The output frequency of 200 GHz is chosen in order to facilitate measurements with *G*-band (140 GHz to 220 GHz) equipment.

#### Circuit Design

The design of this push-push oscillator follows the principle of the oscillators in section 5.1. The passive circuit elements are downscaled for fulfilling the oscillation condition at the desired frequency of oscillation $f_0 = 100\,\text{GHz}$. The values for the lumped element equivalent circuit thus are: $L_C = 25\,\text{pH}$, $L_B = 24\,\text{pH}$, $L_E = 23\,\text{pH}$ and $C_E = 60\,\text{fF}$. The inductances are realized by integrated transmission lines. The two suboscillators are coupled via the base and emitter networks and the output is connected at the emitter network.

The circuit diagram of the whole oscillator including its bias network is drawn in Figure 5.23. The collector terminals are grounded via transmission line resonators. At the emitter terminals 50 µm long transmission lines are connected for increasing the circuits *Q*-factor. For the RF-paths, the ends of these lines are connected via capacitors to the common output port. For the bias decoupling quarter-wave transmission lines are used.

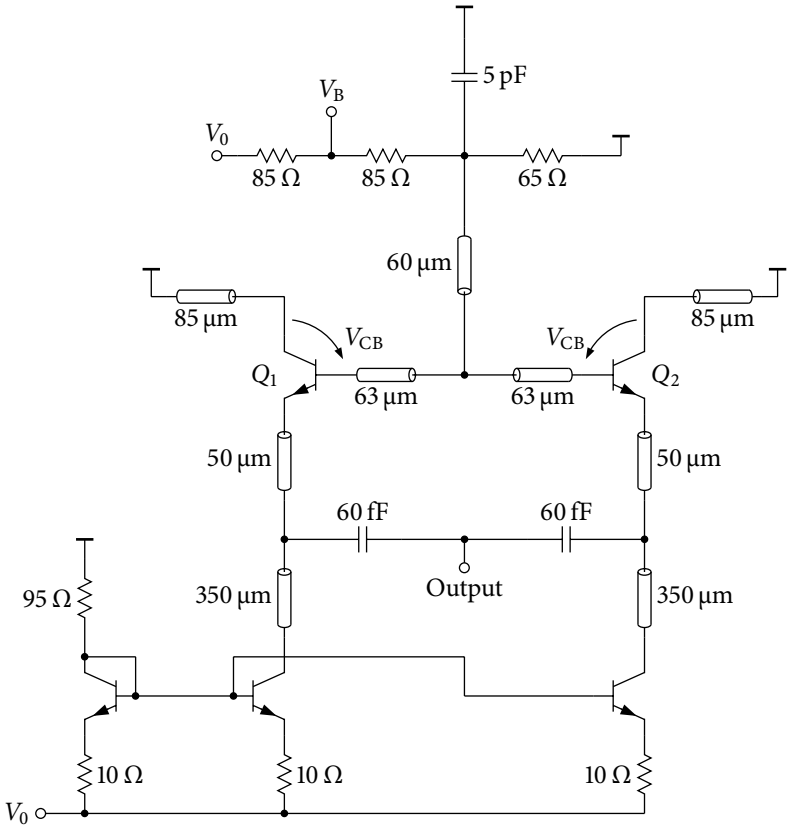


Figure 5.23: Circuit diagram of the 190 GHz push-push oscillator

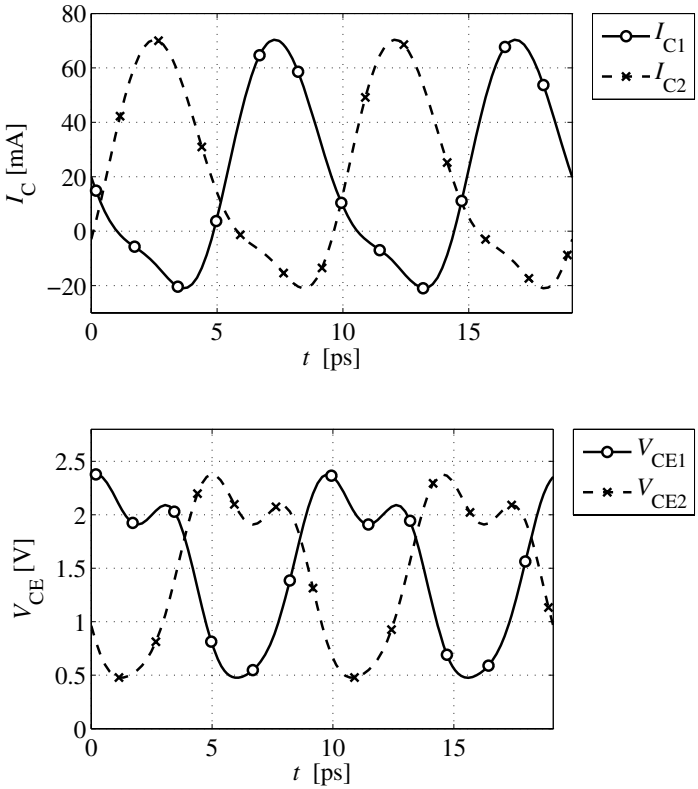


Figure 5.24: Simulated time domain signals of the collector currents $I_C$ and the collector emitter voltages $V_{CE}$ in the suboscillators

The DC supply is accomplished by a constant emitter bias current impressed by a current mirror and a fixed DC voltage at the base terminal. The low impedance connected at the base terminal and the impressed emitter current allow exceeding the breakdown voltage $BV_{CEO} = 1.7\,V$ of the active devices used. An additional DC-pad at the resistive voltage divider at the base terminal is added in order to allow tuning by varying the collector to base voltage $V_{CB}$.

The large signal analysis of the oscillator results in an oscillation frequency $f_0 = 100\,GHz$ and an output power of $-1.5\,dBm$ at $f_1$. As the transistor model is based on measurements only up to 40 GHz the calculated results can be considered only as a rough approximation. Figure 5.24 shows the calculated time domain signals of the collector currents $I_C$ and the collector-emitter voltages $V_{CE}$ of the transistors $Q_1$ and $Q_2$ in the time domain. Compared with the signals in Figure 5.6, here the harmonic content in the signal is considerably lower.

The chip photograph of the designed circuit is depicted in Figure 5.25.

**Experimental Results**

The output signal of the oscillator is characterized in an on-waver-measurement system. To analyze the oscillation frequency an Agilent E4448A spectrum analyzer with an Oleson *G*-band harmonic mixer is used. For phase noise measurements the same mixer is used to downconvert the 190 GHz signal to an intermediate frequency $f_{IF} < 1\,GHz$ allowing the signal to be analyzed by delay line method with the phase noise measurement system PN9000 from Aeroflex. The output power is determined by a DPM-05 *G*-band power sensor from Elva-1. The measured power levels are corrected for losses of the RF-probe and the connecting waveguides by 2 dB. The *G*-band measurements are made at the 'Fraunhofer-Institut für Angewandte Festkörperphysik' (IAF) in Freiburg, Germany. For the analysis at the fundamental frequency a HP 71000 spectrum analyzer with a *W*-band harmonic mixer 11970W is used.

Figure 5.26 demonstrates the performance of the oscillator as a function of the tuning voltage $V_B$ at a constant bias voltage $V_0 = -3.5\,V$. With $V_B = -3\,V$ the output power reaches its maximum of $-4.5\,dBm$. In this bias point the total power consumption of the device is 215 mW. This complies with an efficiency of 1.7 %.

Changing the tuning voltage $V_B$ between $-1\,V$ and $-5\,V$ allows to vary the output frequency from 183.3 GHz to 190.5 GHz, respectively. In this frequency range the

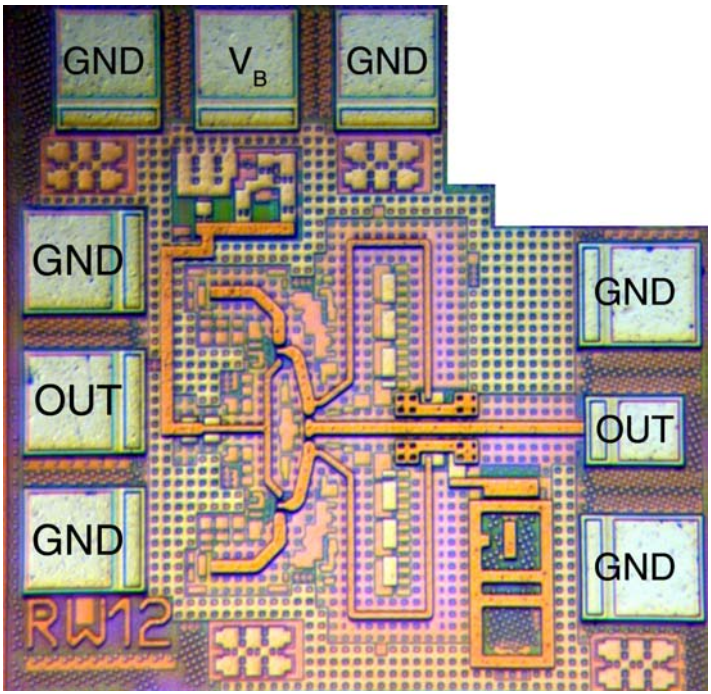


Figure 5.25: Chip photograph of the 190 GHz push-push oscillator (560 µm × 560 µm).

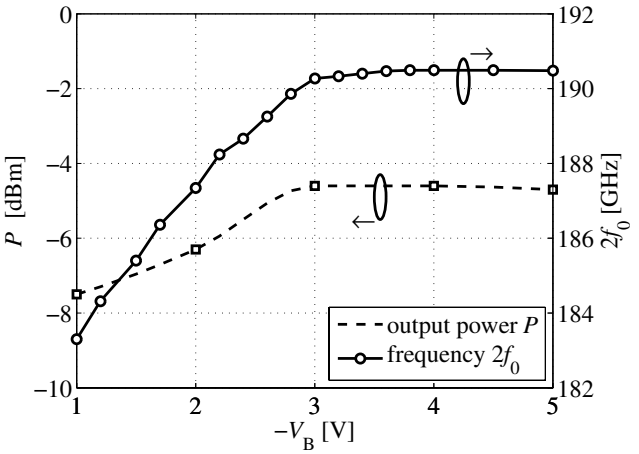


Figure 5.26: Measured output power $P$ and output frequency $2f_0$ as a function of the tuning voltage $V_B$

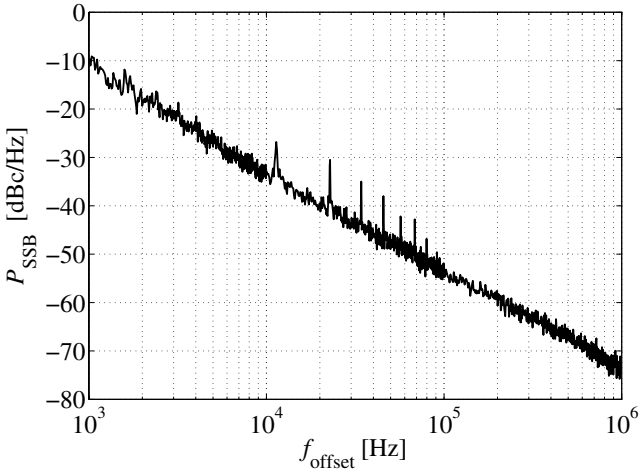


Figure 5.27: Measured single side band phase noise of the 190 GHz oscillator output signal ($V_0 = -3.5\,\mathrm{V}$, $V_B = -3\,\mathrm{V}$)

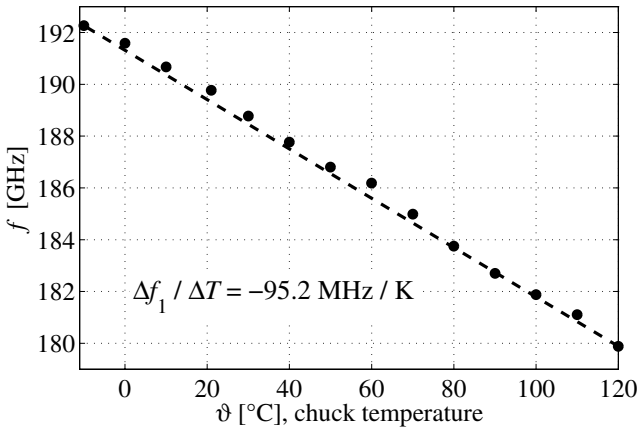


Figure 5.28: Measured temperature dependency of the output frequency

fundamental frequency component in the output signal is measured below −19 dBm and the single side band phase noise of the second harmonic frequency $2f_0$ at an offset frequency of 1 MHz is measured between −73 dBc/Hz and −70 dBc/Hz. Figure 5.27 shows a phase noise measurement for $V_0 = -3.5\,\mathrm{V}$ and $V_\mathrm{B} = -3\,\mathrm{V}$.

Measurements with $V_\mathrm{B} = -5\,\mathrm{V}$ prove that the breakdown voltage $\mathrm{BV_{CEO}} = 1.7\,\mathrm{V}$ of the transistors can be exceeded due to the bias condition used. The calculated collector to emitter voltage in this bias point is $V_\mathrm{CE} = 3.1\,\mathrm{V}$. The frequency stability versus temperature is investigated by *W*-band spectrum measurements of the fundamental frequency. The temperature dependency of the frequency of the output signal plotted in Figure 5.28 results from these measurements.

### 5.2.2 Push-Push Oscillator for 278 GHz

The oscillator described in this section is originally designed for an output frequency of 300 GHz. Due to the uncertainties of the models at the oscillation frequency the measured output frequency is reduced to 278 GHz. The circuit is designed for facilitating measurements with *J*-band equipment (220 GHz to 325 GHz). This band is the highest frequency band, where harmonic mixers are available. The circuit has not been published until now.

#### Circuit Design

For the design of the 278 GHz push-push oscillator the same circuit principle as in section 5.2.1 is used. The transmission line lengths and the capacitances in the emitter networks are scaled in order to fulfill the oscillation condition at $f_0 = 150$ GHz. The circuit diagram of the oscillator is drawn in Figure 5.29. By the external tuning voltage $V_B$ the collector to base voltage $V_{CB}$ can be varied and thus the oscillation frequency is tuned.

By the nonlinear simulation of the push-push oscillator the oscillation frequency is calculated by $f_0 = 150$ GHz and the simulated output power is $-4$ dBm at $f_1$. Due to the low preciseness of the transistor model at the frequencies of interest, a certain deviation in the measurement results must be expected for this circuit. The layout of the total circuit is shown in Figure 5.30.

#### Experimental Results

The output signal of the oscillator is measured on-chip. For measurements in the *J*-band two different harmonic mixers are commercially available. These are the mixer M03HWD of Oleson Microwave Labs that uses the 48th harmonic and shows a conversion loss of 90 dB and the Tektronix mixer WM782J that uses the 20th harmonic and shows a conversion loss of 60 dB. Due to the lack of reference standard sources in this frequency band the conversion loss data are only approximate and are not calibration data.

At the 'Fraunhofer-Institut für Angewandte Festkörperphysik' (IAF) in Freiburg, Germany, the Oleson mixer and appropriate probes facilitating on-waver characterization in the *J*-band are available for measurements. Due to the high conversion

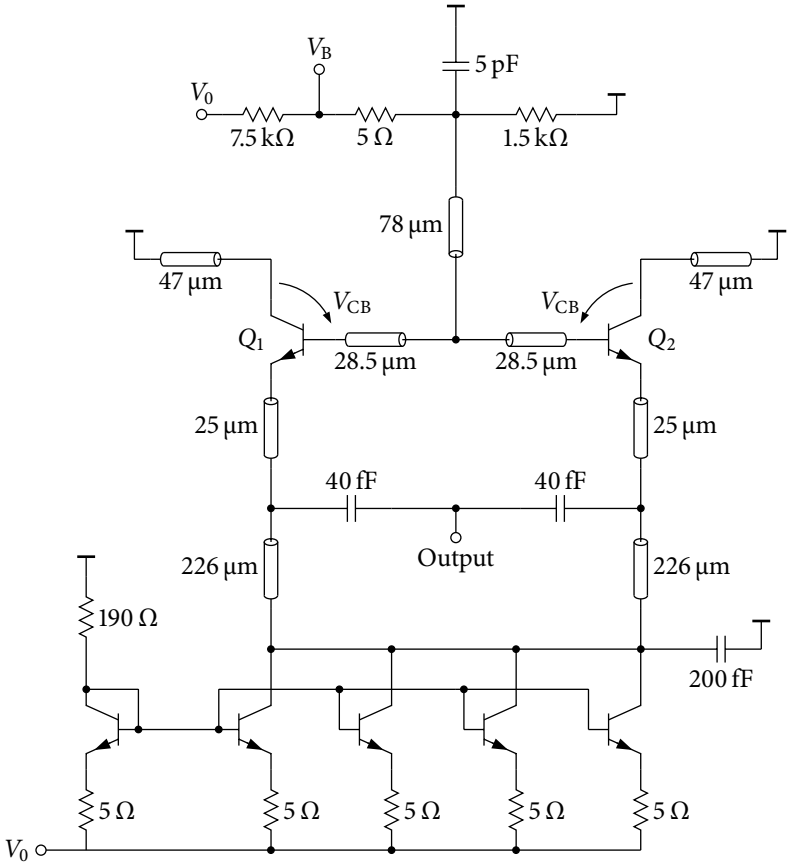


Figure 5.29: Circuit diagram of the 278 GHz push-push oscillator

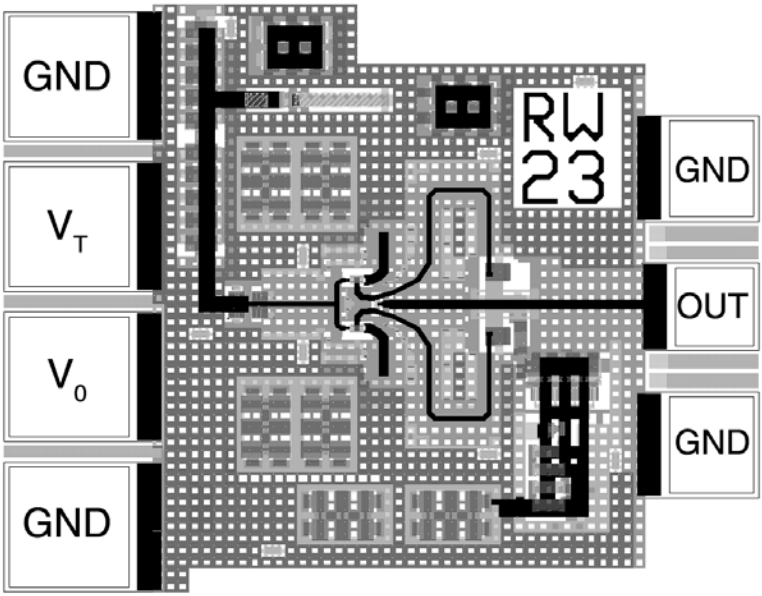


Figure 5.30: Layout of the 278 GHz push-push oscillator (630 µm × 490 µm).

loss of the mixer, however, it has been not possible to detect a signal. The exact oscillation frequency is not known and thus the signal needs to be searched for within a large bandwidth. For a high sensitivity of the spectrum analyzer, the noise level at the input needs to be reduced. This is achieved by a low resolution bandwidth. When measuring with low resolution bandwidths, however, the frequency step size also needs to be reduced in order not to miss the oscillator signal in the spectrum. Both, the low resolution bandwidth and the small frequency step size increase the measurement time significantly. Within acceptable measurement times, the oscillator signal has not exceeded the noise level of the spectrum analyzer.

The output power of the circuit has been measured with the *G*-band power meter of the IAF. With $V_0 = -3\,\mathrm{V}$ and $V_\mathrm{B} = -1.2\,\mathrm{V}$ a maximum power of −30.7 dBm is displayed. The maximum frequency, however, for which the power meter can be

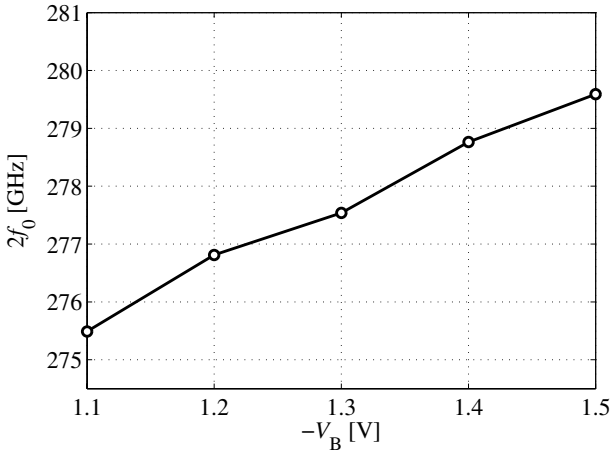


Figure 5.31: Measured output frequency $2f_0$ of the 278 GHz oscillator as a function of the tuning voltage $V_B = -V_{CB}$

calibrated is 220 GHz. The reflections at the waveguide junction from *J*- to *G*-band are not considered. Therefore, a significantly higher output power is expected.

The oscillator output signal has been analyzed in a second step at the 'Lehrstuhl für Hochfrequenztechnik' at the University of Erlangen, Germany, with the harmonic mixer of Tektronix. For these measurements, however, only *W*-band probes with rectangular waveguides for connecting the oscillator circuit have been available. The construction of the probe station and the harmonic mixer do not allow to connect the mixer directly to the waveguide port of the probe. Therefore, a waveguide bent is connected in-between. The total length of the waveguide is thus 10 cm. The losses at the waveguide junction in the *W*-band probe, in the waveguide and at the junction of the *W*-band waveguide to the mixer are estimated by 10 dB. The harmonic mixer is used with the Rohde & Schwarz spectrum analyzer FSEK 30.

Since the conversion loss of the Tektronix mixer is lower, with this measurement setup the oscillator output signal has been detected. Figure 5.31 shows the tunability of the output frequency, when the voltage $V_B$ is varied. The minimum frequency is 276.8 GHz and the maximum is 279.5 GHz. While for the tuning of the oscillator

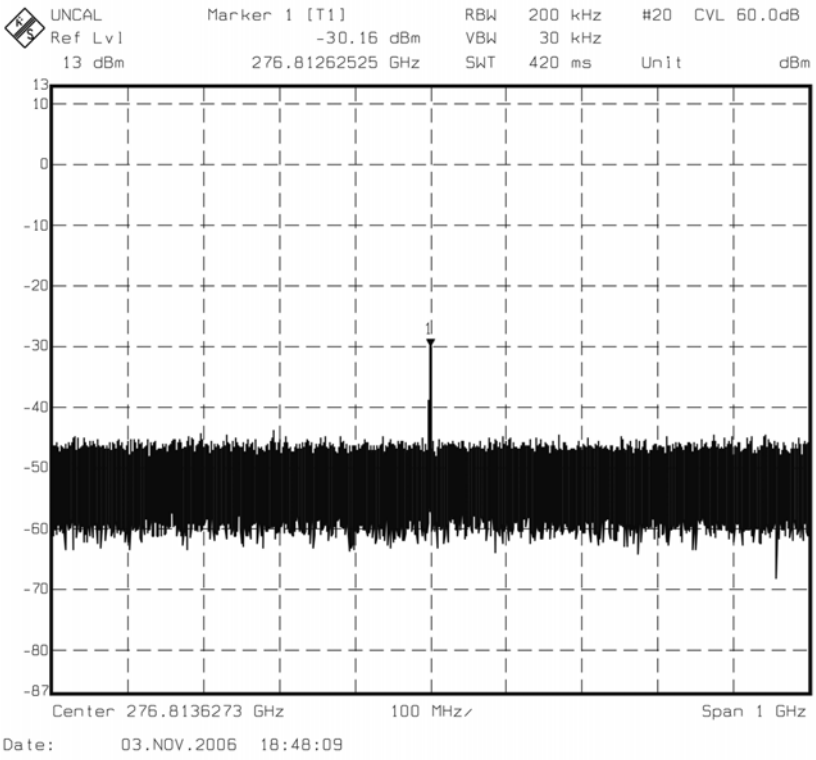


Figure 5.32: Measured spectrum at the second harmonic frequency of the oscillator signal for $V_0 = -3.0\,\mathrm{V}$, $V_\mathrm{B} = -1.2\,\mathrm{V}$. In this figure only the conversion loss of the mixer is considered. Losses of the measurement setup are not accounted for.

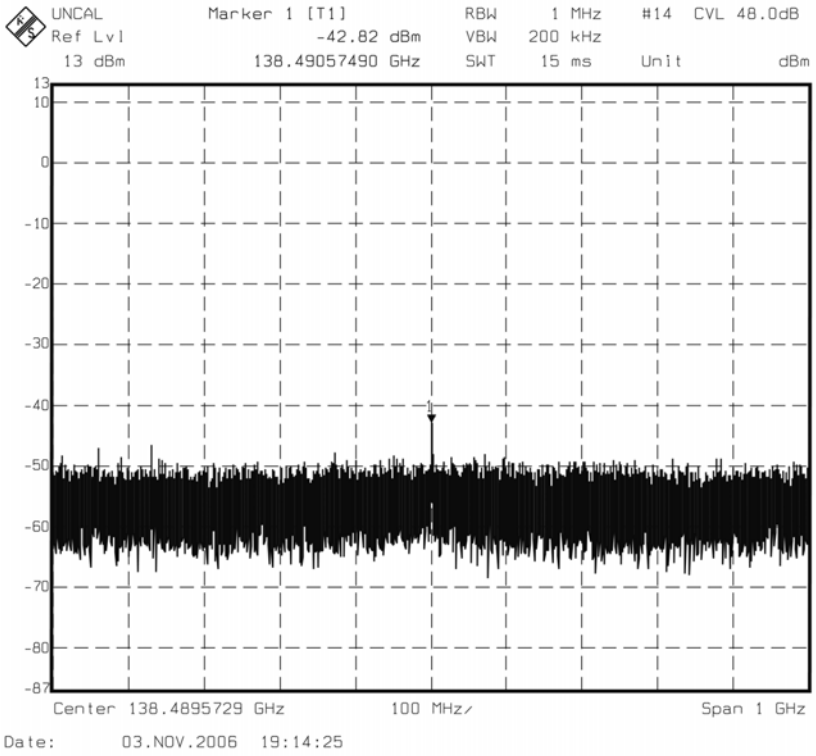


Figure 5.33: Measured spectrum at the fundamental frequency of the oscillator signal for $V_0 = -3.0\,\mathrm{V}$, $V_\mathrm{B} = -1.2\,\mathrm{V}$. In this figure only the conversion loss of the mixer is considered. Losses of the measurement setup are not accounted for.

in section 5.2.1 the collector to base voltage $V_{CB}$ can be varied from −0.5 V up to −2.1 V, this oscillator shows an output signal only in the range from −1.1 V to −1.5 V. As the frequency of oscillation is closer to $f_T$ and $f_{max}$, this circuit shows a higher sensitivity on the bias point used. Thus tuning by changing the collector to base voltage is limited.

Under consideration of the conversion loss of the mixer (60 dB) and the losses due to the waveguide mismatch (10 dB) the measured output power is between −25 dBm and −20 dBm within the tuning range. The variation of the detected power could be a result of the frequency dependency of the termination that is connected to the oscillator circuit. Figure 5.32 shows a measured spectrum at the second harmonic frequency $2f_0$.

The fundamental frequency component is shown in Figure 5.33. This signal is measured by the *G*-band Tektronix mixer WM782G that uses the 14th harmonic. For this measurement, the W-band probe and the waveguide bent are used again for connecting the oscillator with the harmonic mixer. The conversion loss of this mixer is accounted by 48 dB and the waveguide loss is estimated by 4 dB. Considering these losses, within the tuning range in Figure 5.31 the measured fundamental frequency signal power is below −38 dBm.

Due to the low power at the output of the harmonic mixer a measurement of the oscillator phase noise is not possible with the available measurement equipment. The temperature sensitivity of this device has not been investigated until now. The power consumption of the circuit is 132 mW.

# Chapter 6

# Conclusion

In this thesis methods for determining the steady state signals and the noise behavior of oscillators are analyzed. Based on the steady state solution and the Jacobian matrix, which result from the nonlinear analysis of the unperturbed circuit by harmonic balance, the conversion analysis approach allows calculating the oscillator phase noise level for the perturbed circuit. An existing frequency domain method has been extended for the phase noise analysis at harmonic frequencies.

The push-push oscillator principle has been proven to be a suitable circuit topology for low phase noise oscillators. An expression is given to estimate the gain in phase noise that is achieved by push-push oscillators compared to fundamental frequency oscillators. For the circuit design of push-push oscillators a procedure is described.

The SiGe HBTs used show collector to emitter breakdown voltages $BV_{CEO} = 1.7\,V$. In order to allow exceeding this voltage within short time intervals, the driving conditions for the SiGe HBTs are analyzed with respect to the device physics at high currents and high voltages. For the circuit design at millimeter wave frequencies passive circuit components as spiral inductors and transmission lines are considered by full-wave analysis.

Based on these considerations several oscillators have been designed. Exemplarily five of these circuits are presented in this thesis. With the VCO at 77 GHz a tuning range of 6.4 % is achieved, which is sufficient for the intended application in automotive radar systems. The output power within the tuning range is $4.0 \pm 0.4\,dBm$ and the measured single sideband phase noise level at 1 MHz offset frequency is below −105 dBc/Hz. The unwanted fundamental frequency component in the output signal is suppressed by at least 38 dB. With a temperature sensitivity of the output

frequency of –19.5 MHz/K this circuit is less temperature dependent than fundamental frequency oscillators at the same frequency using the same technology. The DC to RF efficiency of this oscillator is 1.8 %. On a similar device it is shown that by reducing the supply voltages the oscillator output power decreases to 1.5 dBm but the efficiency reaches up to 3.5 %.

The oscillators at 190 GHz and 278 GHz have proven that by SiGe HBT oscillators can obtain output signals in the upper millimeter wave frequency range. The 278 GHz oscillator is the highest frequency transistor based oscillator published until now. The author expects that with the technology used, output frequencies above 300 GHz can be generated by the push-push oscillator principle.

# Bibliography


[1] J. F. Luy and P. Russer, Eds., *Future Applications in Silicon-Based Millimeter-Wave Devices*. Springer, Berlin, Germany, 1994.

[2] J. Bock, H. Schäfer, K. Aufinger, R. Stengl, S. Boguth, R. Schreiter, M. Rest, H. Knapp, M. Wurzer, W. Perndl, T. Bottner, and T. Meister, "SiGe bipolar technology for automotive radar applications," in *Bipolar/BiCMOS Circuits and Technology, 2004. Proceedings of the 2004 Meeting*, 2004, pp. 84–87.

[3] M. Racanelli and P. Kempf, "SiGe BiCMOS technology for RF circuit applications," *IEEE Transactions on Electron Devices*, vol. 52, no. 7, pp. 1259–1270, 2005.

[4] G. Freeman, B. Jagannathan, S.-J. Jeng, J.-S. Rieh, A. Stricker, D. Ahlgren, and S. Subbanna, "Transistor design and application considerations for > 200 GHz SiGe HBTs," *IEEE Transactions on Electron Devices*, vol. 50, no. 3, pp. 645–655, 2003.

[5] J.-S. Rieh, M. Khater, G. Freeman, and D. Ahlgren, "SiGe HBT without selectively implanted collector (SIC) exhibiting $f_{max}$ = 310 GHz and $BV_{CEO}$ = 2 V," *IEEE Transactions on Electron Devices*, vol. 53, no. 9, pp. 2407–2409, 2006.

[6] B. Van Haaren, M. Regis, O. Llopis, L. Escotte, A. Gruhle, C. Mahner, R. Plana, and J. Graffeuil, "Low-frequency noise properties of SiGe HBT's and application to ultra-low phase-noise oscillators," *IEEE Transactions on Microwave Theory and Techniques*, vol. 46, pp. 647–652, May 1998.

[7] A. Bangert, M. Schlechtweg, M. Lang, W. Haydl, W. Bronner, T. Fink, K. Kohler, and B. Raynor, "W-band MMIC VCO with a large tuning range using a pseudomorphic HFET," in *IEEE MTT-S International Microwave Symposium Digest, 17-21 June 1996*, vol. 2, 1996, pp. 525–528.

[8] I. Aoki, K. Tezuka, H. Matsuura, S. Kobayashi, T. Fujita, and A. Miura, "80 GHz AlGaAs HBT oscillator," in *18th Annual Gallium Arsenide Integrated Circuit (GaAs IC) Symposium, 3-6 Nov. 1996*, 1996, pp. 281–284.

[9] H. Wang, K. W. Chang, L. Tran, J. Cowles, T. Block, E. Lin, G. Dow, A. Oki, D. Streit, and B. Allen, "Low phase noise millimeter-wave frequency sources using InP-based HBT MMIC technology," *IEEE Journal of Solid-State Circuits*, vol. 31, pp. 1419–1425, Oct. 1996.

[10] T. Kashiwa, T. Ishida, T. Katoh, H. Kurusu, H. Hoshi, and Y. Mitsui, "V-band high-power low phase-noise monolithic oscillators and investigation of low phase-noise performance high drain bias," *IEEE Transactions on Microwave Theory and Techniques*, vol. 46, pp. 1559–1565, Oct. 1998.

[11] H. Siweris, H. Tischer, T. Grave, and W. Kellner, "A monolithic W-band HEMT VCO with feedback topology," in *IEEE MTT-S International Microwave Symposium Digest, 13-19 June 1999*, vol. 1, 1999, pp. 17–20.

[12] V. Schwarz, T. Morf, A. Huber, H. Jackel, and H.-R. Benedickter, "Differential InP-HBT current controlled LC-oscillators with centre frequencies of 43 and 67 GHz," in *Electronics Letters*, vol. 35, July 1999, pp. 1197–1198.

[13] S. Kudszus, T. Berceli, A. Tessmann, M. Neumann, and W. Haydl, "W-band HEMT-oscillator MMICs using subharmonic injection locking," *IEEE Transactions on Microwave Theory and Techniques*, vol. 48, pp. 2526–2532, Dec. 2000.

[14] F. Sinnesbichler, "Hybrid millimeter-wave push-push oscillators using silicon-germanium HBTs," *IEEE Transactions on Microwave Theory and Techniques*, vol. 51, pp. 422–430, Feb. 2003.

[15] B. Floyd, "V-band and W-band SiGe bipolar low-noise amplifiers and voltage-controlled oscillators," in *Radio Frequency Integrated Circuits (RFIC) Symposium, 6-8 June 2004*, 2004, pp. 295–298.

[16] H. Li, H.-M. Rein, T. Suttorp, and J. Bock, "Fully integrated SiGe VCOs with powerful output buffer for 77-GHz automotive Radar systems and applications around 100 GHz," *IEEE Journal of Solid-State Circuits*, vol. 39, pp. 1650–1658, Oct. 2004.

[17] W. Perndl, H. Knapp, K. Aufinger, T. Meister, W. Simburger, and A. Scholtz, "Voltage-controlled oscillators up to 98 GHz in SiGe bipolar technology," *IEEE Journal of Solid-State Circuits*, vol. 39, pp. 1773–1777, Oct. 2004.

[18] F. Ellinger, T. Morf, G. Buren, C. Kromer, G. Sialm, L. Rodoni, M. Schmatz, and H. Jackel, "60 GHz VCO with wideband tuning range fabricated on VLSI

SOI CMOS technology," in *IEEE MTT-S International Microwave Symposium Digest 6-11 June 2004*, vol. 3, 2004, pp. 1329–1332.

[19] F. Lenk, M. Schott, J. Hilsenbeck, and W. Heinrich, "Low phase-noise GaAs-HBT monolithic W-band oscillator," in *34th European Microwave Conference, 13 Oct. 2004*, vol. 2, 2004, pp. 897–900.

[20] C. Changhua and K. O, "A 90-GHz Voltage-Controlled Oscillator with a 2.2-GHz Tuning Range in a 130-nm CMOS Technology," in *Symposium on VLSI Circuits, Digest of Technical Papers. June 16-18 2005*, 2005, pp. 242–243.

[21] B. Floyd, S. Reynolds, U. Pfeiffer, T. Zwick, T. Beukema, and B. Gaucher, "Sige bipolar transceiver circuits operating at 60 GHz," *IEEE Journal of Solid-State Circuits*, vol. 40, no. 1, pp. 156–167, Jan. 2005.

[22] R. Makon, R. Driad, K. Schneider, H. Massler, R. Aidam, R. Quay, M. Schlechtweg, and G. Weimann, "Fundamental low phase noise inp-based DHBT VCO operating up to 89 GHz," *Electronics Letters*, vol. 41, no. 17, pp. 961–963, Aug. 2005.

[23] X. Lan, M. Wojtowicz, I. Smorchkova, R. Coffie, R. Tsai, B. Heying, M. Truong, F. Fong, M. Kintis, C. Namba, A. Oki, and T. Wong, "A Q-band low phase noise monolithic algan/gan HEMT VCO," *IEEE Microwave and Wireless Components Letters*, vol. 16, no. 7, pp. 425–427, July 2006.

[24] C. Cao and K. O, "Millimeter-wave voltage-controlled oscillators in 0.13 µm CMOS technology," *IEEE Journal of Solid-State Circuits*, vol. 41, no. 6, pp. 1297–1304, June 2006.

[25] R. Wanner, M. Pfost, R. Lachner, and G. R. Olbrich, "A 47 GHz Monolithically Integrated SiGe Push-Push Oscillator," in *Topical Meeting on Silicon Monolithic Integrated Circuits in RF Systems, September 8–10, 2004, Atlanta, USA*, Sep 2004, pp. 9–12.

[26] R. Wanner, H. Schäfer, R. Lachner, G. R. Olbrich, and P. Russer, "A Fully Integrated 70 GHz SiGe Low Phase Noise Push-Push Oscillator," in *2005 IEEE MTT-S Int. Microwave Symp. Dig. 12.–17. June 2005, Long Beach, USA*, 2005, pp. 1523–1526.

[27] ——, "A Fully Integrated SiGe Low Phase Noise Push-Push VCO for 82 GHz," in *European Gallium Arsenide and other Compound Semiconductors Application Symposium, Paris, France, 3.-7.10.2005*, oct 2005, pp. 249–252.

[28] ——, "A SiGe Low Phase Noise Push-Push VCO for 72 Ghz," in *XXVIIIth General Assembly of the International Union of Radio Science, 23.-29.10.2005, New Delhi, India*, Oct 2005.

[29] R. Wanner, R. Lachner, and G. R. Olbrich, "SiGe Integrated mm-Wave Push-Push VCOs with Reduced Power Consumption," in *IEEE Radio Frequency Integrated Circuits Symposium, June 11–13, San Francisco, USA*, jun 2006, pp. 483–486.

[30] ——, "A SiGe Monolithically Integrated 75 GHz Push-Push VCO," in *Topical Meeting on Silicon Monolithic Integrated Circuits in RF Systems, Januar September 18–20, 2006, San Diego, USA*, 2006, pp. 375–378.

[31] Y. Baeyens and Y. Chen, "A monolithic integrated 150 GHz SiGe HBT push-push VCO with simultaneous differential V-band output," in *IEEE MTT-S International Microwave Symposium Digest, 8-13 June 2003*, vol. 2, 2003, pp. 877–880.

[32] Y. Baeyens, C. Dorschky, N. Weimann, Q. Lee, R. Kopf, G. Georgiou, J. Mattia, R. Hamm, and Y.-K. Chen, "Compact InP-based HBT VCOs with a wide tuning range at W- and D-band," *IEEE Transactions on Microwave Theory and Techniques*, vol. 48, pp. 2403–2408, Dec. 2000.

[33] K. Kobayashi, A. Oki, L. Tran, J. Cowles, A. Gutierrez-Aitken, F. Yamada, T. Block, and D. Streit, "A 108-GHz InP-HBT monolithic push-push VCO with low phase noise and wide tuning bandwidth," *IEEE Journal of Solid-State Circuits*, vol. 34, pp. 1225–1232, Sept. 1999.

[34] S. Kudszus, W. Haydl, A. Tessmann, W. Bronner, and M. Schlechtweg, "Push-push oscillators for 94 and 140 GHz applications using standard pseudomorphic GaAs HEMTs," *IEEE MTT-S International Microwave Symposium Digest*, vol. 3, pp. 1571–1574, May 2001.

[35] Y. Kwon, D. Pavlidis, T. Brock, and D. Streit, "A D-band monolithic fundamental oscillator using InP-based HEMT's," *IEEE Transactions on Microwave Theory and Techniques*, vol. 41, pp. 2336–2344, Dec. 1993.

[36] S. Rosenbaum, B. Kormanyos, L. Jelloian, M. Matloubian, A. Brown, L. Larson, L. Nguyen, M. Thompson, L. Katehi, and G. a. Rebeiz, "155- and 213-GHz AlInAs/GaInAs/InP HEMT MMIC oscillators," *IEEE Transactions on Microwave Theory and Techniques*, vol. 43, pp. 927–932, Apr. 1995.

[37] K. Uchida, H. Matsuura, T. Yakihara, S. Kobayashi, S. Oka, T. Fujita, and A. Miura, "A series of InGaP/InGaAs HBT oscillators up to D-band," *IEEE Transactions on Microwave Theory and Techniques*, vol. 49, pp. 858–865, May 2001.

[38] K. Uchida, I. Aoki, H. Matsuura, T. Yakihara, S. Kobayashi, S. Oka, T. Fujita, and A. Miura, "104 and 134 GHz InGaP/InGaAs HBT oscillators," in *Gallium Arsenide Integrated Circuit (GaAs IC) Symposium*, Oct. 1999, pp. 237–240.

[39] W. Winkler, J. Borngraber, and B. Heinemann, "LC-oscillators above 100 GHz in silicon-based technology," in *Proceeding of the 30th European Solid-State Circuits Conference, ESSCIRC 2004*, Sept. 2004, pp. 131–134.

[40] P.-C. Huang, M.-D. Tsai, H. Wang, C.-H. Chen, and C.-S. Chang, "A 114 GHz VCO in 0.13 µm CMOS technology," in *Solid-State Circuits Conference, 2005. Digest of Technical Papers. ISSCC. 2005 IEEE International*, Feb. 2005, pp. 404–606.

[41] P.-C. Huang, R.-C. Liu, H.-Y. Chang, C.-S. Lin, M.-F. Lei, H. Wang, C.-Y. Su, and C.-L. Chang, "A 131 GHz push-push VCO in 90-nm CMOS technology," in *Radio Frequency integrated Circuits (RFIC) Symposium, 2005. Digest of Papers. 2005 IEEE*, June 2005, pp. 613–616.

[42] Y. Baeyens, N. Weimann, V. Houtsma, J. Weiner, Y. Yang, J. Frackoviak, A. Tate, and Y. Chen, "High-power submicron InP d-HBT push-push oscillators operating up to 215 GHz," in *Compound Semiconductor Integrated Circuit Symposium, 2005. CSIC '05. IEEE*, Oct./Nov. 2005.

[43] C. Cao and K. O, "A 140-GHz fundamental mode voltage-controlled oscillator in 90-nm CMOS technology," *IEEE Microwave and Wireless Components Letters*, vol. 16, no. 10, pp. 555–557, Oct. 2006.

[44] C. Cao, E. Seok, and K. O, "192 GHz push-push VCO in 0.13 µm CMOS," *Electronics Letters*, vol. 42, no. 4, pp. 208–210, Feb. 2006.

[45] P. Roux, Y. Baeyens, O. Wohlgemuth, and Y. Chen, "A monolithic integrated 180 GHz sige HBT push-push oscillator," in *Gallium Arsenide and Other Semiconductor Application Symposium, 2005. EGAAS 2005. European*, Oct. 2005, pp. 341–343.

[46] R. Wanner, R. Lachner, and G. Olbrich, "A monolithically integrated 190-GHz SiGe push-push oscillator," *IEEE Microwave and Wireless Components Letters*, vol. 15, no. 12, pp. 862–864, Dec 2005.

[47] H. Eisele and R. Kamoua, "High-performance oscillators and power combiners with inp gunn devices at 260-330 GHz," *IEEE Microwave and Wireless Components Letters*, vol. 16, no. 5, pp. 284–286, May 2006.

[48] J. Nishizawa, P. Plotka, H. Makabe, and T. Kurabayashi, "GaAs TUNNETT diodes oscillating at 430-655 GHz in CW fundamental mode," *IEEE Microwave and Wireless Components Letters*, vol. 15, no. 9, pp. 597–599, Sept. 2005.

[49] W. Anzill, *Berechnung und Optimierung des Phasenrauschens von Oszillatoren*. München: Dissertation an der Technischen Universität München, Lehrstuhl für Hochfrequenztechnik, 1993.

[50] W. Anzill and P. Russer, "A general method to simulate noise in oscillators based on frequency domain techniques," *IEEE Transactions on Microwave Theory and Techniques*, vol. 41, no. 12, pp. 2256–2263, 1993.

[51] W. Mathis and P. Russer, "Oscillator Design," in *Encyclopedia of RF and Microwave Engineering*, K. Chang, Ed. Hoboken, New Jersey: John Wiley, 2005.

[52] M. Odyniec, *RF and Microwave Oscillator Design*. Boston, London: Artech House Publishers, 2002.

[53] G. Vallauri, "Über die wirkungsweise der in der drahtlosen telegraphie benutzten vakuumröhren mit drei elektroden (audion)," *Jahrbuch der Drahtlosen Telegraphie*, vol. 12, p. 349ff, 1917.

[54] K. Kurokawa, "Some Basic Characteristics of Broadband Negative Resistance Oscillator Circuits," *Bell Sys. Tech. J.*, vol. 48, pp. 1937–1955, 1969.

[55] B. van der Pol, "The nonlinear theory of electrical oscillations," *Proceedings of the Institute of Radio Engeneering (IRE)*, vol. 22, pp. 1051–1086, 1934.

[56] T. Aprille and T. Trick, "A computer algorithm to determine the steady-state response of nonlinear oscillators," *Circuits and Systems, IEEE Transactions on [legacy, pre - 1988]*, vol. 19, no. 4, pp. 354–360, 1972.

[57] L. Chua and P.-M. Lin, *Computer-aided analysis of electronic circuits: algorithms and computational techniques*. Englewood Cliffs, NJ: Prentice-Hall, 1975.

[58] C.-R. Chang and M. Steer, "Frequency-domain nonlinear microwave circuit simulation using the arithmetic operator method," *IEEE Transactions on Microwave Theory and Techniques*, vol. 38, no. 8, pp. 1139–1143, 1990.

[59] M. Schwab, *Ein kombiniertes Zeit-Frequenzbereichsverfahren zur Berechnung periodischer Schwingungen von Oszillatoren*. München: Dissertation an der Technischen Universität München, Lehrstuhl für Hochfrequenztechnik, 1991.

[60] ——, "Determination of the steady state of an oscillator by a combined time-frequency method," *IEEE Transactions on Microwave Theory and Techniques*, vol. 39, no. 8, pp. 1391–1402, 1991.

[61] K. S. Kundert, J. K. White, and A. Sangiovanni-Vincentelli, *Steady-State Methods for Simulating Analog and Microwave Circuits*. Kluwer Academic Publishers, 1990.

[62] V. Rizzoli, A. Lipparini, and E. Marazzi, "A general-purpose program for nonlinear microwave circuit design," *IEEE Transactions on Microwave Theory and Techniques*, vol. 83, no. 9, pp. 762–770, 1983.

[63] S. A. Maas, *Nonlinear Microwave and RF Circuits*. Norwood, MA: Artech House, 2003.

[64] M. Steer and P. Khan, "An algebraic formula for the output of a system with large-signal, multifrequency excitation," *Proceedings of the IEEE*, vol. 71, no. 1, pp. 177–179, 1983.

[65] D. Leeson, "A simple model of feedback oscillator noise spectrum," *Proceedings of the IEEE*, vol. 54, no. 2, pp. 329–330, 1966.

[66] R. L. Stratonovich, *Introduction to the Theory of Random Noise*, 1st ed. New York: Gordon and Breach, 1963.

[67] I. Berstein and G. Gorelik, "Frequency modulation noise in oscillators," *Proceedings of the IRE*, vol. 45, pp. 94–99, Jan. 1957.

[68] W. Freude, "Messung der Statistik eines Gunn-Oszillator-Signals und Vergleich mit einem Rechenmodell," *Archiv für Elektronik und Übertragungstechnik*, vol. 30, pp. 209–218, Mar. 1976.

[69] W. A. Edson, "Noise in oscillators," *Proceedings of the IRE*, vol. 48, pp. 1454–1466, 1960.

[70] E. Hafner, "The effects of noise in oscillators," *Proceedings of IREE*, vol. 54, pp. 1311–1330, 1964.

[71] K. Kurokawa, "Noise in synchronized oscillators," *IEEE Transactions on Microwave Theory and Techniques*, vol. 16, no. 4, pp. 234–240, Apr. 1968.

[72] ——, "Injection locking of microwave solid-state oscillators," *Proceedings of the IEEE*, vol. 61, no. 10, pp. 1386–1410, Oct. 1973.

[73] F. Kaertner, "Determination of the correlation spectrum of oscillators with low noise," *IEEE Transactions on Microwave Theory and Techniques*, vol. 37, no. 1, pp. 90–101, Jan. 1989.

[74] ——, "Analysis of white and $f^{-\alpha}$-noise in oscillators," *International Journal of Circuit Theory and Applications*, vol. 18, no. 5, pp. 485–519, May 1990.

[75] F. X. Kärtner, *Untersuchung des Rauschverhaltens von Oszillatoren*. München: Dissertation an der Technischen Universität München, Lehrstuhl für Hochfrequenztechnik, 1988.

[76] A. Demir, "Phase noise in oscillators: DAEs and colored noise sources," in *Computer-Aided Design, 1998. ICCAD 98. Digest of Technical Papers. 1998 IEEE/ACM International Conference on*, Nov. 1998, pp. 170–177.

[77] V. Rizzoli, F. Mastri, and D. Masotti, "General noise analysis of nonlinear microwave circuits by the piecewise harmonic-balance technique," *IEEE Transactions on Microwave Theory and Techniques*, vol. 42, no. 5, pp. 807–819, 1994.

[78] A. Hajimiri and T. Lee, "A general theory of phase noise in electrical oscillators," *IEEE Journal of Solid-State Circuits*, vol. 33, no. 2, pp. 179–194, 1998.

[79] A. Suárez, S. Sancho, S. Ver Hoeye, and J. Portilla, "Analytical comparison between time- and frequency-domain techniques for phase-noise analysis," *IEEE Transactions on Microwave Theory and Techniques*, vol. 50, no. 10, pp. 2353–2361, 2002.

[80] Y. Ou, N. Barton, R. Fetche, N. Seshan, T. Fiez, U.-K. Moon, and K. Mayaram, "Phase noise simulation and estimation methods: a comparative study," *IEEE Transactions on Circuits and Systems II: Analog and Digital Signal Processing*, vol. 49, no. 9, pp. 635–638, 2002.

[81] P. Vanassche, G. Gielen, and W. Sansen, "On the difference between two widely publicized methods for analyzing oscillator phase behavior," in *Computer Aided Design, 2002. ICCAD 2002. IEEE/ACM International Conference on*, 2002, pp. 229–233.

[82] M. Filleböck, *Kombinierte Zeit-Frequenzbereichsmethoden zum Entwurf von Mikrowellenoszillatoren*. München: Dissertation an der Technischen Universität München, Lehrstuhl für Hochfrequenztechnik, 1996.

[83] J. R. Bender and C. Wong, "Push-Push Design Extends Bipolar Frequency Range," *Microwaves & RF*, pp. 91–98, Oct. 1983.

[84] Anthony M. Pavio and Mark A. Smith, "A 20-40-GHz Push-Push Dielectric Resonator Oscillator," *IEEE Transactions on Microwave Theory and Techniques*, vol. 33, pp. 1346–1349, Dec. 1985.

[85] F. Sinnesbichler, "Hybrid millimeter-wave push-push oscillators using silicon-germanium HBTs," *IEEE Transactions on Microwave Theory and Techniques*, vol. 51, pp. 422–430, Feb. 2003.

[86] F. C. Jones, *Radio Handbook*. Radio, 1937.

[87] F. X. Sinnesbichler and H. Geltinger and G. R. Olbrich, "A 38-GHz push-push oscillator based on 25-GHz $f_T$ BJT's," *IEEE Microwave and Guided Wave Letters*, vol. 9, no. 4, pp. 151–153, April 1999.

[88] A.-S. Hyun, H.-S. Kim, J.-Y. Park, J.-H. Kim, J.-C. Lee, N.-Y. Kim, B.-K. Kim, and U.-S. Hong, "K-band hair-pin resonator oscillators," *IEEE MTT-S International Microwave Symposium Digest*, vol. 2, pp. 725–728, 1999.

[89] F. X. Sinnesbichler and G.R. Olbrich, "SiGe HBT push-push oscillators for V-band operation," *Topical Meeting on Silicon Monolithic Integrated Circuits in RF Systems*, pp. 55–59, 2000.

[90] M. Schott, F. Lenk, C. Meliani, and W. Heinrich, "Low phase noise X-band push-push oscillator with frequency divider," in *Microwave Symposium Digest, 2005 IEEE MTT-S International*, 2005.

[91] M. M. Schott, F. Lenk, and W. Heinrich, "Low phase noise X-band clapp push-push oscillator," in *German Microwave Conference, GeMiC, April 5–7, 2005, Ulm*, 2005.

[92] P. Kinget, "Integrated GHz voltage controlled oscillators," in *Analog Circuit Design: (X)DSL and Other Communication Systems; RF MOST Models; Integrated Filters and Oscillators*, W. Sansen, J. Huijsing, and R. van de Plassche, Eds. Kluwer, 1999, p. 353–381.

[93] A. Zanchi, C. Samori, S. Levantino, and A. Lacaita, "A 2-v 2.5-GHz-104-dbc/hz at 100 khz fully integrated VCO with wide-band low-noise automatic amplitude control loop," *IEEE Journal of Solid-State Circuits*, vol. 36, no. 4, pp. 611–619, 2001.

[94] J. van der Tang and D. Kasperkovitz, "Oscillator design efficiency: a new figure of merit for oscillator benchmarking," in *Circuits and Systems, 2000. Proceedings. ISCAS 2000 Geneva. The 2000 IEEE International Symposium on*, vol. 2, 2000, pp. 533–536.

[95] W.-M. L. Kuo, J. Cressler, Y.-J. Chen, and A. Joseph, "An inductorless Ka-band SiGe HBT ring oscillator," *IEEE Microwave and Wireless Components Letters*, vol. 15, no. 10, pp. 682–684, 2005.

[96] K. W. Kobayashi, A. K. Oki, L. T. Tran, J. C. Cowles, A. Gutierrez-Aitken, F. Yamada, T. R. Block, and D. C. Streit, "A 108-GHz InP-HBT monolithic push-push VCO with low phase noise and wide tuning bandwidth," *IEEE Journal of Solid-State Circuits*, vol. 34, no. 9, pp. 1225–1232, Sept. 1999.

[97] M. Gris, "Wideband Low Phase Noise Push-Push VCO," *Applied Microwave & Wireless*, pp. 28–32, Jan 2000.

[98] H. C. Chang, X. Cao, U. K. Mishra, and R. A. York, "Phase Noise in Coupled Oscillators: Theory and Experiment," *IEEE Transactions on Microwave Theory and Techniques*, vol. 45, pp. 604–615, May 1997.

[99] K. Fujii, Y. Hara, and H. Isikawa, "J Band GaAs MMIC Push-Push VCO," *Applied Microwave & Wireless*, pp. 20–23, June 1993.

[100] T. Meister, H. Schäfer, K. Aufinger, R. Stengl, S. Boguth, R. Schreiter, M. Rest, H. Knapp, M. Wurzer, A. Mitchell, T. Bottner, and J. Bock, "SiGe bipolar technology with 3.9 ps gate delay," in *Bipolar/BiCMOS Circuits and Technology Meeting, 2003. Proceedings of the*, 2003, pp. 103–106.

[101] Kirk, C.T., "A theory of transistor cutoff frequency $f_T$ falloff at high current densities," *IEEE Transactions on Electron Devices*, vol. 9, no. 2, pp. 164–174, Mar. 1962.

[102] Webster, W. M., "On the variation of junction-transistor current-amplification factor with emitter current," *Proc. IRE*, vol. 42, pp. 914–916, 1954.

[103] Rittner, E. S., "Extension of the theory of the junction transistor," *Physical Review*, vol. 94, pp. 1161–1171, 1954.

[104] M. Friedrich and H.-M. Rein, "Analytical current-voltage relations for compact sige HBT models. i. the "idealized" HBT," *IEEE Transactions on Electron Devices*, vol. 46, no. 7, pp. 1384–1393, 1999.

[105] A. Joseph, J. Cressler, D. Richey, and G. Niu, "Optimization of sige HBTs for operation at high current densities," *IEEE Transactions on Electron Devices*, vol. 46, no. 7, pp. 1347–1354, 1999.

[106] F. X. Sinnesbichler, "Großsignalmodellierung von SiGe-Heterobipolartransistoren für den Entwurf von Millimeterwellenschaltungen," Ph.D. dissertation, Dissertation am Lehrstuhl für Hochfrequenztechnik der Technischen Universität München, 1999.

[107] M. Rickelt, H. M. Rein, and E. Rose, "Influence of impact-ionization-induced instabilities on the maximum usable output voltage of Si-bipolar transistors," *IEEE Transactions on Electron Devices*, vol. 48, no. 4, pp. 774–783, Apr 2001.

[108] M. Rickelt and H. M. Rein, "A novel transistor model for simulating avalanche-breakdown effects in Si bipolar circuits," *IEEE Journal of Solid-State Circuits*, vol. 2, no. 9, pp. 1184–1197, Sep 2002.

[109] H. K. Gummel and H. C. Poon, "An Integral Charge Control Model of Bipolar Transistors," *The Bell System Technical Journal*, vol. 49, pp. 827–853, May-June 1970.

[110] R. M. Warner, *Integrated Circuits: Design Principles and Fabrication*. McGraw-Hill, New York, 1965.

[111] R. Wanner, "Overview of RF MEMS Inductors," in *AMICOM Deliverables D24 and D25*, J. Tuovinen and T. Vähä-Heikkilä, Eds., http://www.amicom.info/OpenPlatform/index.php/Inductors, 2004.

[112] R. Ribas, J. Lescot, J.-L. Leclercq, J. Karam, and F. Ndagijimana, "Micromachined microwave planar spiral inductors and transformers," *IEEE Transactions on Microwave Theory and Techniques*, vol. 48, no. 8, pp. 1326–1335, Aug. 2000.

[113] J.-C. Chang, A. Abidi, and M. Gaitan, "Large suspended inductors on silicon and their use in a 2 µm CMOS RF amplifier," *IEEE Electron Device Letters*, vol. 14, no. 5, pp. 246–248, May 1993.

[114] J.-B. Yoon, Y.-S. Choi, B.-I. Kim, Y. Eo, and E. Yoon, "CMOS-compatible surface-micromachined suspended-spiral inductors for multi-GHz silicon RF ICs," *IEEE Electron Device Letters*, vol. 23, no. 10, pp. 591–593, Oct. 2002.

[115] E.-C. Park, Y.-S. Choi, J.-B. Yoon, S. Hong, and E. Yoon, "Fully integrated low phase-noise VCOs with on-chip MEMS inductors," *IEEE Transactions on Microwave Theory and Techniques*, vol. 51, no. 1, pp. 289–296, Jan. 2003.

[116] D. Young, V. Malba, J.-J. Ou, A. Bernhardt, and B. Boser, "Monolithic high-performance three-dimensional coil inductors for wireless communication applications," in *Electron Devices Meeting, 1997. Technical Digest., International*, Dec. 1997, pp. 67–70.

[117] Y.-J. Kim and M. Allen, "Surface micromachined solenoid inductors for high frequency applications," *IEEE Transactions on Components, Packaging, and Manufacturing Technology, Part C*, vol. 21, no. 1, pp. 26–33, Jan. 1998.

[118] D. Lukashevich and P. Russer, "Network-oriented models of transmission line structures in MMICs," in *Silicon Monolithic Integrated Circuits in RF Systems, 2003. Digest of Papers. 2003 Topical Meeting on*, Apr. 2003, pp. 178–181.